DUST HEATING IN NEARBY

GALAXIES

A thesis submitted to the University of Manchester
for the degree of Master of Science
in the Faculty of Engineering and Physical Sciences

November 2012

By
Lingjie Kong
School of Physics and Astronomy

Contents

List of Tables

List of Figures

Abstract

Dust is an important part of the interstellar medium (ISM). Dust absorbs ultraviolet and optical star light and re-emits in the mid- and far-infrared light. More than one third of the total star light in the universe is absorbed and re-emitted by dust. Observations show that dust emission is strongly correlated with star formation rates. Recent research with Herschel Space Observatory data has shown that dust emission at ≥ 250 μm appears to be heated by the total stellar population rather than just star forming regions, questioning the use of dust to measure star formation.

To further study dust heating sources, we carried out an analysis on NGC4254, NGC4303, NGC4321 and NGC4579 using 100, 160, 250, 350 and 500 μm images from the Herschel Reference Survey and Herschel Virgo Cluster Survey. We used Hα images to trace star forming regions and 1.6 μm image to trace the total stellar populations. Colour temperature maps (based on 100/160, 160/250, 250/350 and 350/500 μm ratio maps) were compared to the Hα and 1.6 μm images. We made ratio plots against Hα and 1.6 μm pixel by pixel to find out whether there is a linear relation.

All the infrared ratios in four galaxies show strong correlation both with Hα and 1.6 μm data. NGC4303, NGC4321 and NGC4579 shows no significant difference between Hα and 1.6 μm data which indicate the dust in these three galaxies maybe heated by both star forming regions and the evolved star regions. NGC4254 shows a better correlation between the colour temperature maps with the Hα image than the 1.6 μm image, which means more dust is heated by star forming regions than by the evolved stars. There is no clear evidence for a dust component which is heated only by the evolved stars. From the colour temperature maps, I find dust temperatures

in the range of 12-30 K assuming that $\beta = 2$. There is no evidence for dust at lower temperature than 12 K.

All the four galaxies show hotter dust at longer wavelength which is unexpected. Changing the value of β to $\beta = 2.2$ fixes the problem. Further study is needed to determine if β is indeed higher than 2 in these and possibly other galaxies.

Declaration

I declare that no portion of the work referred to in this thesis has been submitted in support of an application for another degree or qualification of this or any other university or other institute of learning.

Lingjie Kong

University of Manchester

Jodrell Bank Center of Astrophysics

Oxford Road

Manchester

Copyright

i. The author of this thesis (including any appendices and/or schedules to this thesis) owns certain copyright or related rights in it (the Copyright) and s/he has given The University of Manchester certain rights to use such Copyright, including for administrative purposes.

ii. Copies of this thesis, either in full or in extracts and whether in hard or electronic copy, may be made only in accordance with the Copyright, Designs and Patents Act 1988 (as amended) and regulations issued under it or, where appropriate, in accordance with licensing agreements which the University has from time to time. This page must form part of any such copies made.

iii. The ownership of certain Copyright, patents, designs, trade marks and other intellectual property (the Intellectual Property) and any reproductions of copyright works in the thesis, for example graphs and tables (Reproductions), which may be described in this thesis, may not be owned by the author and may be owned by third parties. Such Intellectual Property and Reproductions cannot and must not be made available for use without the prior written permission of the owner(s) of the relevant Intellectual Property and/or Reproductions.

iv. Further information on the conditions under which disclosure, publication and commercialisation of this thesis, the Copyright and any Intellectual Property and/or Reproductions described in it may take place is available in the University IP Policy (download pdf file from http://documents.manchester.ac.uk/DocuInfo .aspx?DocID=487), in any relevant Thesis restriction declarations deposited in the University Library, The University Librarys regulations (see http://www.manchester.ac.uk/ library/aboutus/regulations) and in The Universitys policy on presentation of Theses.

Acknowledgements

I would like to thank both of my supervisors Prof. A. Zijlstra and Dr. G. Bendo for their guidance and help during my study for this project. I would also like to thank Prof.G. Fuller and Dr. I. McDonald. Prof.G. Fuller have generously give me time and patience to answer my questions and always kindly take time to listen to me when I meet with problems and need help. Dr. I. McDonald have been always kindly answer my questions and did proof readings for my English writing in my literature review.

I want to give a special thank to Mareika Haberichter who have been always there to help me with my Latex whenever I need her. She has saved so much of my time to solve Latex problems and made learning Latex so easy.

Also, I want to thank my classmates Constantinos Demetroullas, Supachai Awiphan and Mohammad Hussein who have made this study time friendly and memorable.

Chapter 1

Dust and Star Formation

This chapter aims to understand why dust is an important part of ISM and how dust emission in IR and FIR correlates with star formation rate. Observations of the emission from dust in nearby galaxies as well as the changing viewpoints on how dust emission is related to star formation are discussed in preparation for research on IR and FIR dust emission data from *Herschel*.

Section 1 gives a brief introduction to dust. Section 2 introduces three aspects of dust first, the origins of dust; second, the importance of dust in the ISM and in star forming regions; third, linking the dust emission in the spectral energy distribution (SED) with stellar evolution. Telescopes launched to detect dust emission, *IRAS*, *ISO*, *Spitzer* and *Herschel*, are presented in section 3. Section 4 discusses the data from these space observatories and the role of dust as a star-formation tracer at different wavelengths. A summary of whether dust should be a good SFR tracer or not and the goal of this project is provided in section 5.

1.1 Introduction

Dust plays an important role in the astrophysics of the Interstellar Medium (ISM) and in the dynamics of star formation. More than one third of the energy emitted by stars in the Universe is absorbed and re-emitted by dust (Sanders & Mirabel, 1996). Dust attenuates radiation at short wavelengths and re-emits it in the infrared (IR)

and far infrared(FIR), hence dust reshapes the spectra of galaxies. Dust is closely linked with star formation because stars usually are formed in dusty regions. Young stars emit strong visible and ultraviolet (UV) light. Their light is extincted by the surrounding dust and the dust, heated by this light, emits in the IR and FIR (Draine, 2003). In recent years, dust emission is being studied as a tracer for star forming regions after the space observatories made the observation in IR and FIR available. Arguments exist as to whether dust emission at a particular wavelength should be a good SFR tracer or not.

1.2 The Importance of Dust in The Interstellar Medium

The interstellar medium (ISM) and intergalactic medium fills the empty space between stars and galaxies. The ISM consists of gas and dust. Interstellar dust comprises 1% by mass of the ISM, is mostly made of grains of graphite or silicate compounds, typically sized between 0.1 μm to several μm, and plays an important role in the evolution of galaxies.

1.2.1 Where does dust in the universe come from?

Stars produce helium and metal elements[1] during their lives. The higher mass the star is, the higher the abundance of metal elements it will produce. When a star comes to the end of its life, it will eject some of its mass. The fraction of mass lost is related to the star's original mass. Massive stars (over 10 solar masses) lose over 80% of their mass during their life cycle (Poelarends et al., 2008) while even the lower mass stars (about 1 solar mass) observed can also lose up to 40% of their total mass. All the lost mass is ejected in the form of gas and small dust grains. These ejecta become part of the Interstellar Medium (ISM). There are three main sources of dust production as discussed below.

---

[1]Elements heavier than helium such as carbon, nitrogen, oxygen and other heavier elements are considered to be metal as in astrophysics.

Stars with mass below about 10 solar masses will usually turn into Asymptotic Giant Branch (AGB) stars in the late stages of their evolution. Fig. 1.1 shows the procedure of production of dust grains by AGB stars. 'Metal' elements are produced during the shell burning phases, and convection brings the products of nuclear burning to the surface. During the late stages of an AGB star's evolution (the thermal pulsing AGB), it pulsates hugely. The pulsation pushes these molecules together with other elements outwards. Fig. 1.1 also shows the temperature becoming lower in the direction of outwards from the centre. At about 3×10^3 K, molecules form at the pulsating atmosphere. The ejected elements form dust grains at about 10^3 K. Dust formation happens at the outer edge of the pulsating atmosphere which make the inner dust shell of the AGB star. The acceleration of the outflow pushes the outer dust into the Universe. More than 70% of dust in the Universe occurr through radiation pressure on the dust, carrying the gas with it by friction produced by AGB stars (Habing, 1996).
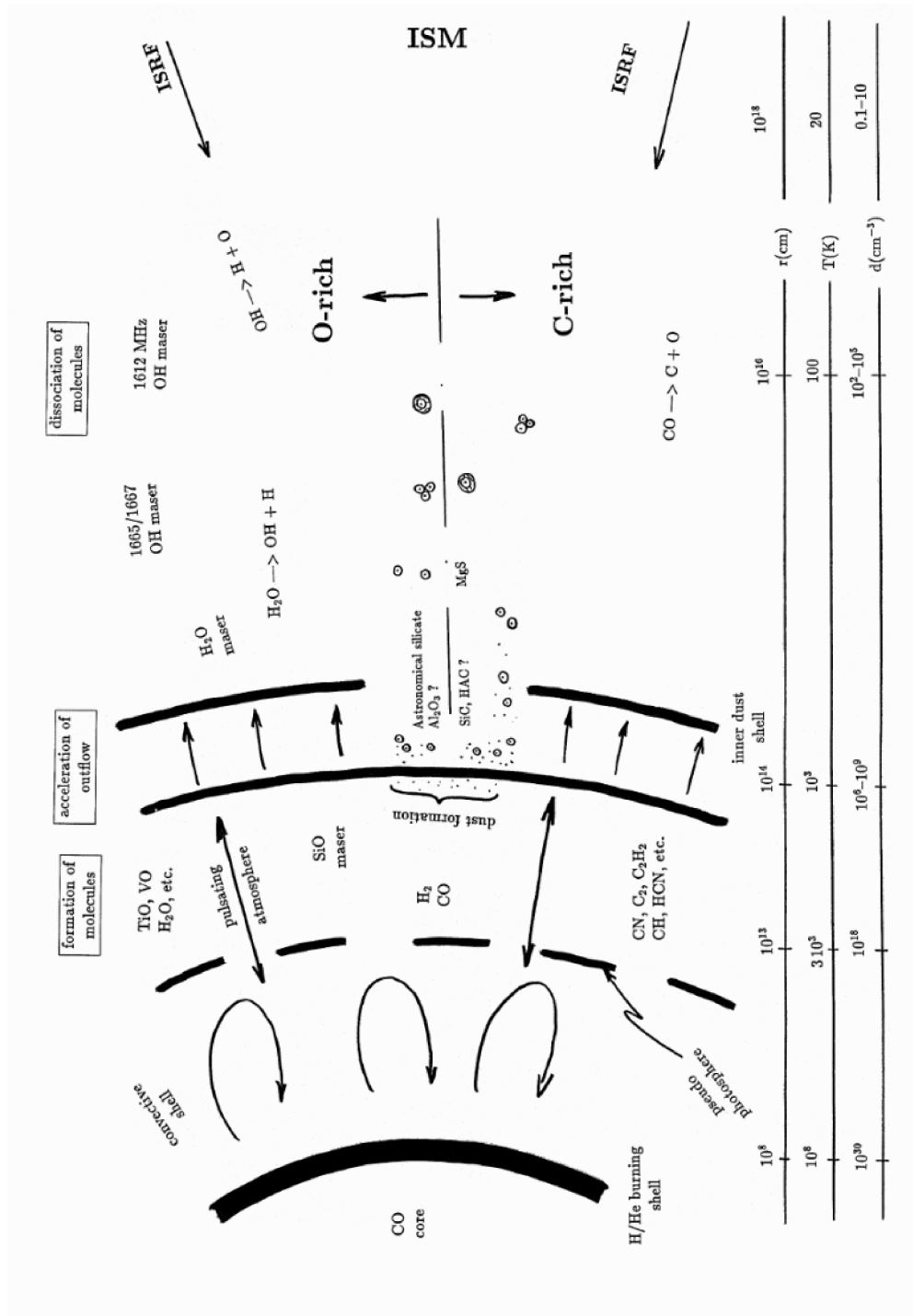
Figure 1.1: The procedure of production of dust grains by AGB stars(LeBertre, 2004).

Massive stars at about 8 - 12 solar mass will produce a carbon core in supernovae explosion. Only stars more than 12 solar mass will produce heavier elements like iron. Also, stars more than 8-12 solar mass will not go through the AGB but produce supernovae at the end of their lives. During their Super-AGB phase, these stars will produce a large amount of dust, but most of the dust will be destroyed by the shock wave of the supernovae. It was first claimed by Dunne et al. (2003) that supernovae produce most of the dust in the universe but this was disproved by Krause et al. (2004) and Barlow et al. (2010). They found a different sample for that. Supernovae produce less than 30% of the dust in the Universe (Andrews et al., 2011).

Dust also grows in the interstellar medium. The mechanism of how this happens is not yet known, but molecules or atoms maybe accreted onto existing dust grains (Dwek, 1998).

The amount of dust distributed among stars varies greatly in different galaxies. The dust grains are mostly silicates and amorphous carbon. Typically, dust grains are up to several micrometres across (Zinner, 2003). Different sizes and temperatures of dust grains give rise to different emission spectra which unveil valuable information about the Universe such as star formation to us.

1.2.2 Why is dust so important?

The life cycle of stars enriches the interstellar medium (ISM) and supplies new material for star formation. Star formation usually happens where the ISM is dense, which implies a high dust density. It has been observed that star formation usually happens in dusty areas of a galaxy. Star formation is very important for the understanding of the evolution of the Universe because it drives the form of galaxies and produce the heavy elements. The importance of dust is discussed in detail by the following three points.

Dust emission is a powerful tracer of star forming activity

Dust absorbs and reprocesses a large amount of starlight in the Universe. More than one third of the starlight is absorbed, and remitted by dust in the infrared.

If we use $\nu F\nu$ to represent energy per wavelength as shown in Fig. 1.2, the total energy (the area under the graph) shows that the infrared comprises over a third of a galaxy's spectral energy distribution (1 to 100 μm) (Sanders & Mirabel, 1996). The IR and FIR glow from interstellar dust can be measured. Fig. 1.3 shows the observed emissivity by dust per H nucleon, based on COBE-FIRAS and COBE-DIRBE photometry (Draine, 2003). It shows that dust emission longer than 50μm accounts for more than 65% of the total dust emission. In this thesis we will analyse the dust emission in this wavelength range.
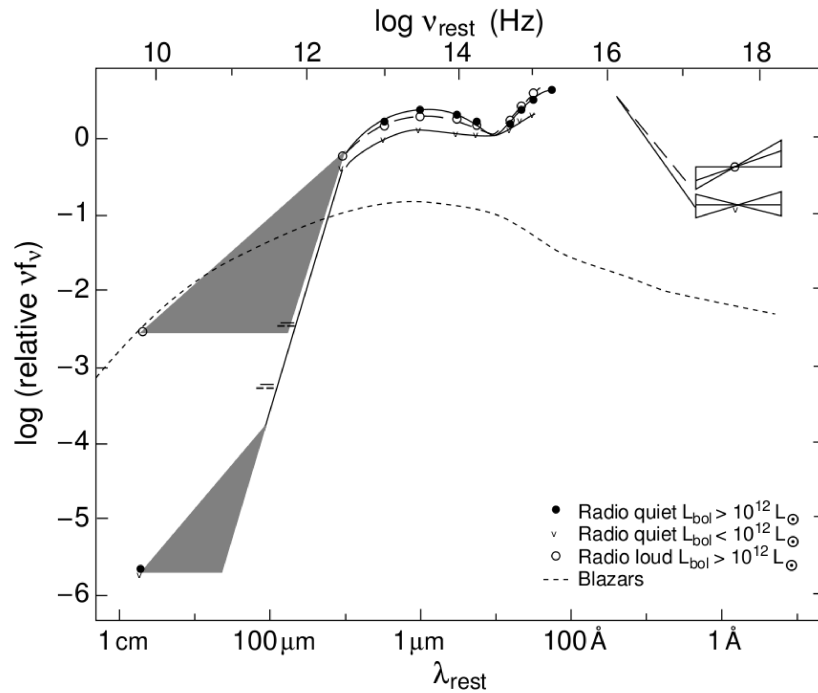
Figure 1.2: Mean spectral energy distributions from radio to X-ray in wavelength. Samples selected from radio-loud and radio-quiet QSOs (Sanders et al., 1989), and blazars (Impey & Neugebauer, 1988). Figure is from Sanders & Mirabel (1996).

The absorption also results in the attenuation of the short wavelength radiation from stars. So the spectra of galaxies and the optical view of the Universe is greatly reshaped by dust. The Infrared Astronomical Satellite (IRAS) survey showed many many bright in infrared galaxies that had never been observerved before because of the stellar light in these galaxies are so heavily obscured, that the only way to observe them is through dust emission (Soifer et al., 1987).

The dust surrounding the star forming region will be heated by absorbing the UV radiation and re-emit in IR. Therefore, dust emission can be used to trace
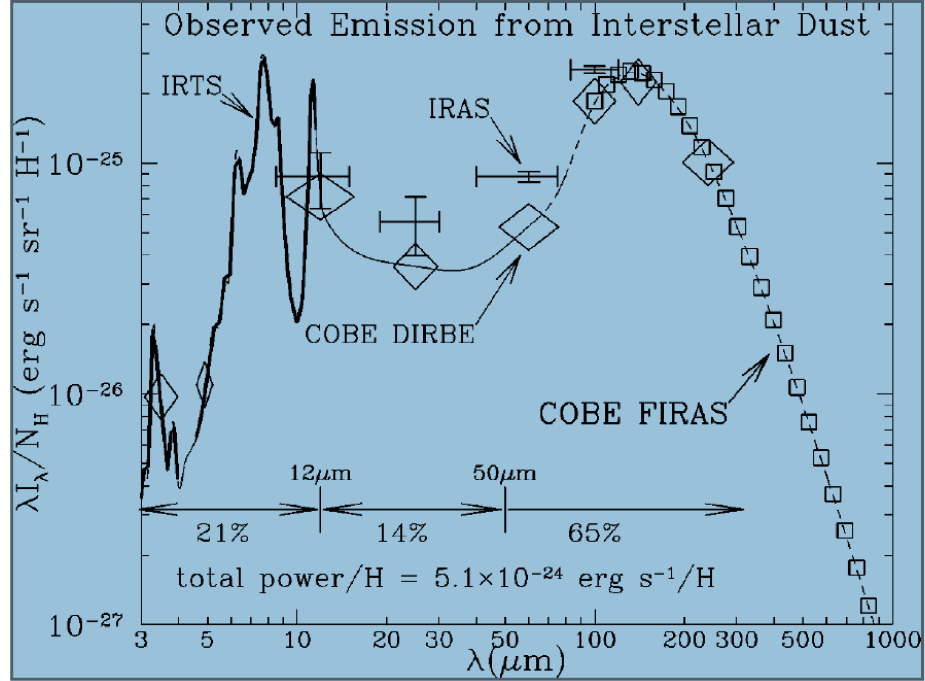
Figure 1.3: Observed emission from diffuse interstellar dust. Crosses: IRAS; squares: COBE-FIRAS; diamonds: COBE-DIRBE; thick line: IRTS. The total power $\approx$ $5.1 \times 10^{-24}\,\mathrm{erg.s^{-1}/H}$ is estimated from the interpolated broken line (Draine, 2003).

star formation activity when SFR dominate the UV energy output of the galaxies (Kennicutt, 1998b). The emission of dust is one of the most powerful tracers of star formation in galaxies (Kennicutt, 1998a; Hirashita et al., 2003).

Dust provides a shield for the star forming gas

The molecular hydrogen (H_2) is easily dissociated back to atomic hydrogen (H I) and then ionised to H II by the UV emission of the surrounding stars. The H I and H II is not a good material for star formation any more because the ionised hydrogen is too hot to collapse. Also even if photo-dissociation did not happen, the gas exposed to star light will get hot and the thermal pressure will stop it from collapsing to form star. But the hydrogen gas is surrounded by thick dust and dust provides a shield for the star-forming gas by blocking and absorbing UV radiation from the stars and hence protecting the star-forming gas from dissociation (Hollenbach & Tielens, 1997; Duley & Williams, 1986). Dust here becomes a key part in this procedure because of its function of blocking the star light.

Dust is a catalyst for star formation

Molecular hydrogen is the main material for star formation, so the quantity of molecular hydrogen in an area becomes the key determinant of whether star formation can proceed or not. Hydrogen is produced in the beginning of the Universe in the form of atomic hydrogen or ionised hydrogen. By the existence of dust, molecular hydrogen can be formed because it is observed that molecular hydrogen forms on dust grains. Hollenbach & Salpeter (1971) and Duley & Williams (1986) proved from completely different principles that dust acts as a catalyst in the process of transforming the atomic hydrogen to molecular hydrogen. Also, cooling is necessary for star formation and dust is a very good cooling agent.

1.2.3 Stellar evolution and the spectral energy distribution

Stellar evolution
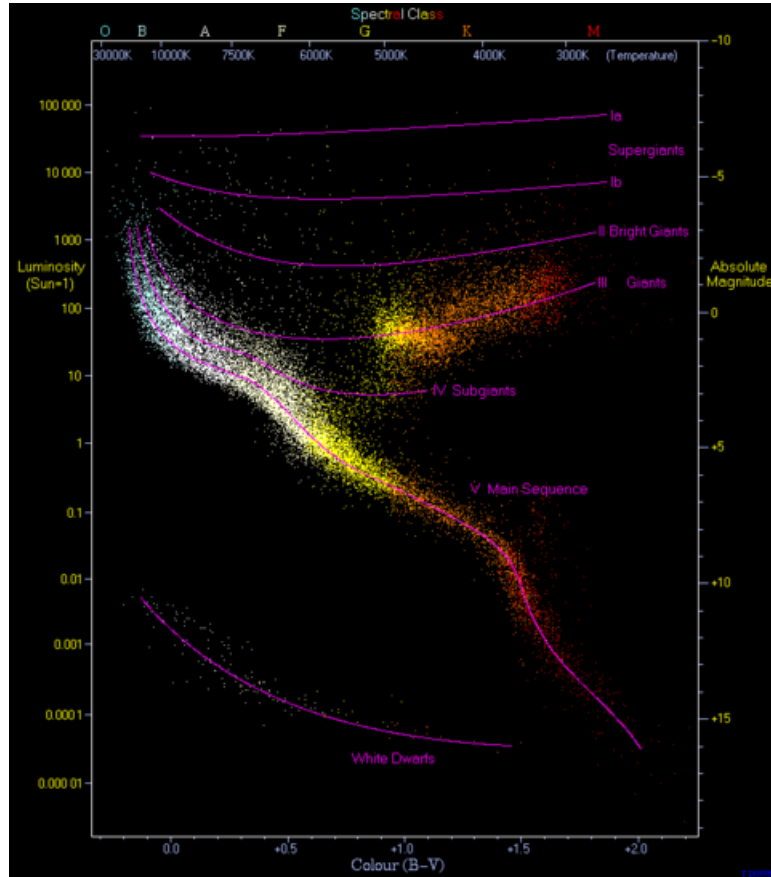
Figure 1.4: HR diagram. Taken from http://www.atlasoftheuniverse.com/hr.html

Fig. 1.4 shows an HR diagram mainly of nearby Hipparcos (High Precision Parallax Collection Satellite) stars. The HR diagram shows the main sequence (MS) stars where the most luminous stars are the O/B-type stars, matched only by some of the red giant stars. The O/B-type stars are high mass stars, and they dominate the energy output of the galaxy. This is because the luminosity of a star scales as $L \propto M^{3.5}$, while the number of stars scales as the initial mass function (IMF), $n \, dm \propto M^{-2.3}$ (the Salpeter function) (Salpeter, 1955). The energy produced therefore scales as $E \, dm = nLdm \propto M^{+1.2}$. However, these high mass stars are short lived. The life time of a star can be estimated as (very roughly) $t \propto M/L \propto M/M^{3.5} = M^{-2.5}$. A massive O-type star ($M \gtrsim 20 \, M_\odot$) may live for perhaps 10^7 yr, while the Sun can live for 10^{10} yr. Following an event of star formation, the initial luminosity will be high, but will drop after 10^7 yr as the high-mass stars end their lives and only the low-mass stars are left.

Assuming that high mass stars are those with mass $M > 10 \, M_\odot$, Integration of the IMF over high mass stars gives a result that they account for are about 3.8% of the stellar population. But although O/B type stars dominate the luminosity of the galaxy, red giant stars also contribute to the luminosity of the galaxy as we see from the HR diagram. The low-mass stars will eventually evolve into red giants. During this phase, they also reach high luminosities, peaking at $\sim 10^4 \, L_\odot$. This phase is again short lived, with the highest luminosities found during the AGB phase, lasting 10^7–10^8 yr which is similar to the life time of the O/B type stars. The stars have masses between 0.8 to $5 \, M_\odot$ live longer so most of them will stay longer on the MS. So though integrating the Salpeter function we find that the low mass stars are about 50 times more numerous than high mass stars, we discount them as big contributors to the luminosity.

Fig. 1.5 shows the four stages of a evolved MS star. In this diagram, it shows the main sequence (core hydrogen burning) stars which have mass lower than $9 \, M_\odot$ have a different way of evolve. They will have longer life and after 3×10^8 yr, they develop into Sub-Giant Branch (SB) and then Red Giant Branch (RGB). RGB stars are giant in size and very luminus compare to when they were in main sequence. They stay
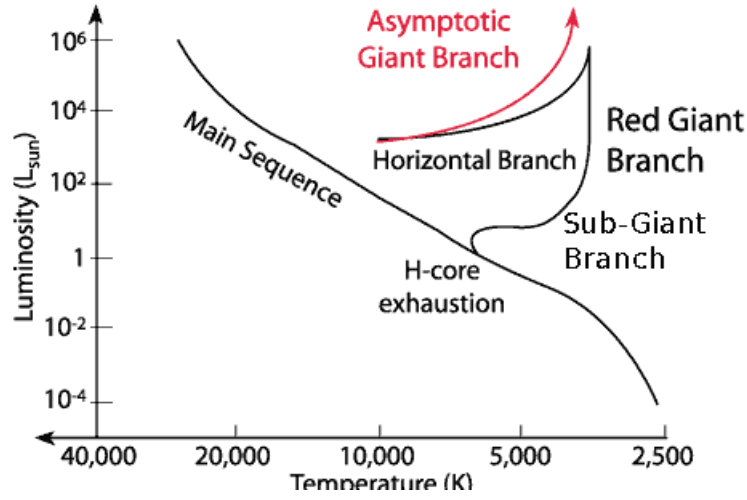
Figure 1.5: Definition of SGB, RGB, HB and AGB.
Taken from http://www.noao.edu/outreach/press/pr03/sb0307

in RGB for some time (depends on their mass) and evolve into a Horizontal Branch
(HB) with their size and luminosity goes down, and later become giant again and
even more luminus which are called Athymptotic Giant Branch (AGB) stars.

Intigration of the IMF for stars mass between 5 to $10\,M_{\odot}$ showes they take about
5.6% of the stellar popullation. They appear to outnumber the O/B type stars, but
their brightness is still less than the young stars. The luminosity comparison of
different stellar types at different times is shown in Fig. 1.6.

Fig. 1.6 shows the starburst model, which means the stellar population of a
single age, and indicate the contribution to the integrated luminosity of various
phases of late stellar evolution, as function of the age of the stellar population.The
y axis shows the ratio of the bolometric luminosity at time i and stellar type j to
the bolometric luminosity of the total stellar population at time i, and the x axis
is the age of the stars. It is a normalised diagram which means the contribution of
luminosity by different type of stars is the fraction of the total luminosity at each
time. This diagram does not show the time before $10^{7.5}$ yr, which is dominated by
O/B type stars from the main squence. From the diagram we can see that at $10^{7.5}$ yr,
MS stars still make up about 75% of the total bolometric lominosity, and all the
other evolved types take 25%. At about $10^{8.5}$ yr, when most high mass bright stars
have finished their life, AGB stars start to take over and dominate the luminosity
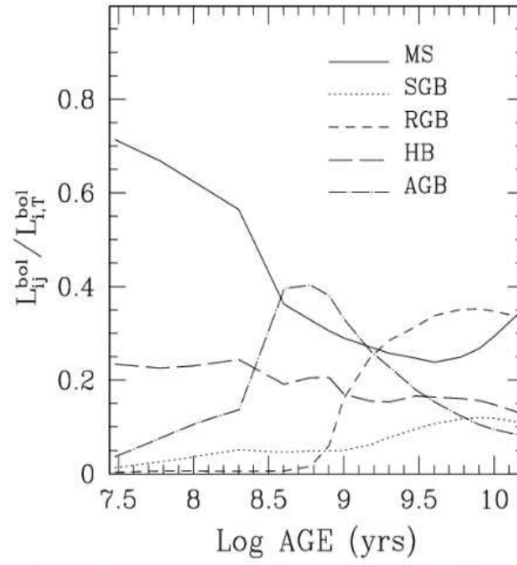
Figure 1.6: Stellar luminosity contribution. MS: Main Sequence stars. SGB: Sub-Giant Branch. RGB: Red Giant Branch. HB: Horizontal Branch. AGB: Asymptotic Giant Banch. Taken from Maraston (2011)

contribution. But they only contribute a maximum of 40% of the total and MS stars still make up about 30%. After $10^{9.5}$ yr, RGB stars take over and become the biggest contributor to the total luminosity which contribute about 35% to the total. In a starburst galaxy, the evolved stars will dominate the energy output, after the O/B stars have disappeared. However, they are cool ($T_{eff} \sim 4000$ K) and they emit the bulk of their energy in the near infrared. The young O/B stars emit their energy in the UV.

The high mass RGB stars (5 to 9 $M_\odot$) experience a very short RGB stage and a much longer and brighter AGB stage. The lower mass ones experience a comparitively longer RGB stage. That's why though the RGB stage of a star is before the AGB stage in time order, high mass stars have shorter life and evolve into high luminus AGB stars earlier than most MS stars evolve into RGB stars. Their high brightness and longer life make them take over the bolometric luminosity ratio among all the stellar popualtion at $10^{8.5}$ yr in the starburst model in Fig 1.6.

But the galaxy is a dynamic place in star formation. Hot young stars are produced all the time in most spiral gaxies we observe today, though the age of these galaxies can be 10^{10} yr. So the luminosity we observe today is a combination of

young O/B type stars and the evolved stars. In each galaxy there are star forming regions, which can be observed by strong Hα emission, and areas dominated by evolved red stars.

From the above we can conclude that not only hot young high mass O/B type stars contribute to the luminosity of galaxies, but the evolved stars also contribute to the luminosity of galaxies. Luminosity is the energy emitted by stars. This energy can heat the dust surrounding the stars. These luminosity contirbution in galaxies give a possibility that evolved stars can be a source beside the hot young stars that heating the dust at the same time.

Spectral energy distribution of dust in star forming regions

The emission at mid to far infrared comes from several sources (Draine et al., 2007; Draine, 2003; Popescu et al., 2011):

- $\leq 5\,\mu$m: Star light from the total stellar population, including newly formed stars and evolved stars.

- $3\,\mu$m to $15\,\mu$m: Mainly dominated by the Polycyclic Aromatic Hydrocarbons (PAHs).

- $10\,\mu$m to $70\,\mu$m: Mainly dominated by very small grains or hot dust which maybe associated with star formation.

- $\geq 70\,\mu$m: Large dust grains at ∼10-35 K.

Fig. 1.7 shows emission sources contributing to the spectral energy distribution (SED) of NGC 891. This figure demonstrates that dust is the main emitter between 6 μm to 1000 μm. NGC 891 is typical of other galaxies for the SED curve (Draine & Li, 2007).
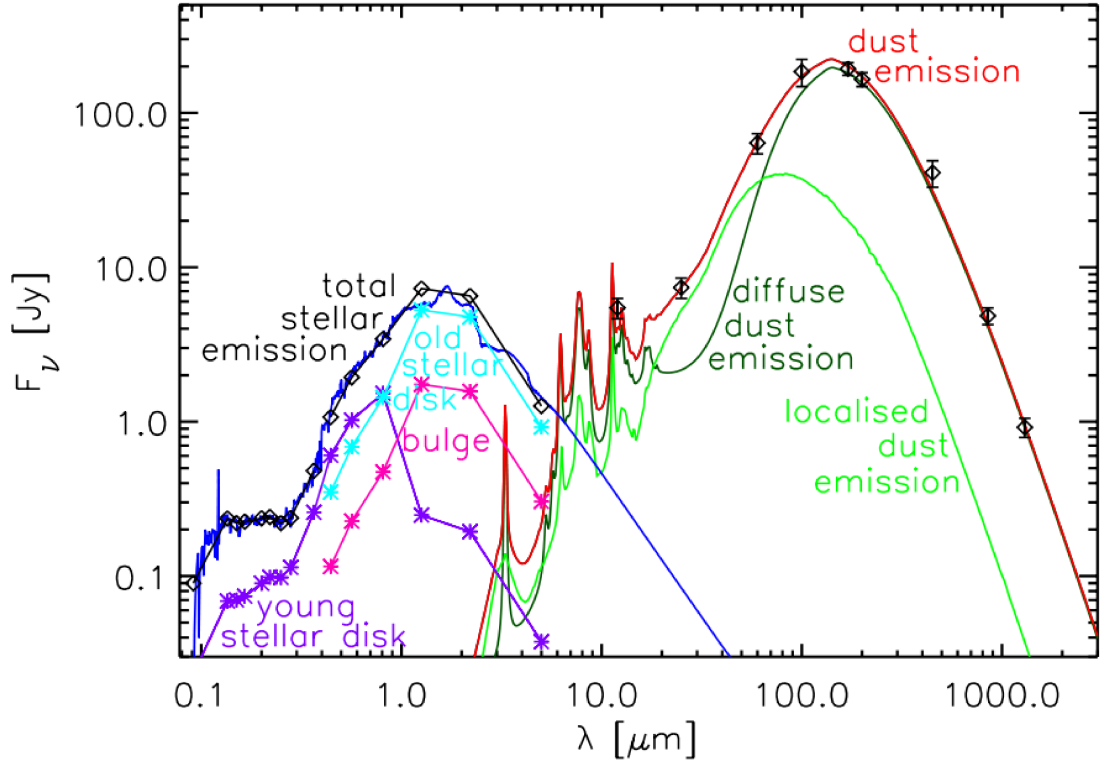
Figure 1.7: The curves show the best fit model of spectral energy distribution (SED) observed in flux densities against wavelength of NGC 891. The red line shows the predicted PAH and dust emission SED. Light-green line shows the predicted clumpy component associated with the star-forming regions (Popescu et al., 2011).

1.3 Space Observatories Launched for Dust Emission

Dust emits at mid- to far-infrared wavelengths. The wavelength of the dust emission is related to its temperature. Higher temperature dust emits at shorter wavelengths while colder dust emits at longer wavelengths. The temperature of the dust can be measured by the observed emission curve of the dust. Because of the important information that dust emission spectra provide, several space observatories have been launched specifically focusing on the mid- to far-infrared (IR and FIR) wavelength regions.

The atmosphere of the earth reflects, scatters and absorbs a large fraction of the radiation that the Earth receives, hence the amount of extra-terrestrial star radiation that we receive on the ground is very limited. Fig. 1.8 shows the bands that can be observed from the ground. Infrared extends between the end of the

Table 1.1: Summary of the important telescopes for IR and FIR emission.

Name of Telescope	Year of Launch	Wavelength coverage (μm)	Reference
IRAS	1983	12 - 100	Soifer et al. (1987)
ISO	1995	2.5 - 240	Kessler (1995)
Spitzer	2003	3.6 - 160	Werner et al. (2004)
Herschel	2009	100 - 500	Boselli et al. (2010)

visible light (about 1 μm) and microwave (about 1 cm) which is mostly blocked by the atmosphere. Dust emission is mostly at about 10 μm to 500 μm which is in the IR to FIR, hence undetectable from ground. The best place to observe IR and FIR is from space. So, space telescopes were launched for the purpose of studying of dust emission.

Though there are many telescopes launched for IR observation, only four space observatories (see Table 1.1) are discussed in this paper. This is because only these four telescopes focus on the longer wavelengths ($\geq 50\,\mu$m) emitted by larger dust grain, and only these four produced high quality SED of galaxies in these wavelengths.
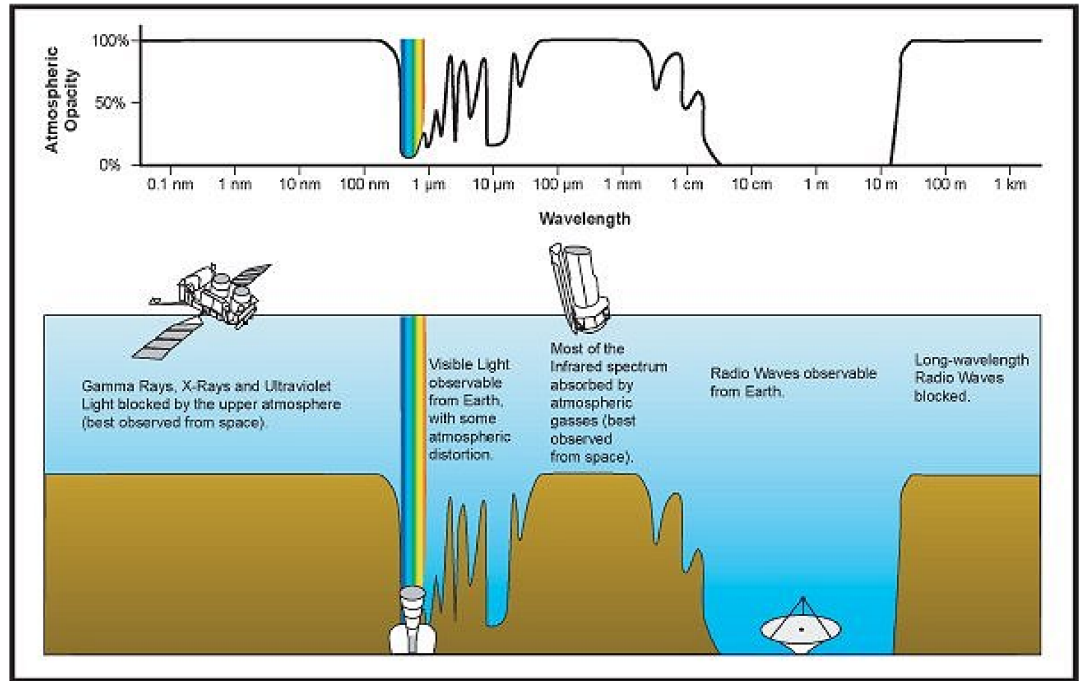
Figure 1.8: Atmospheric transmission of the electromagnetic spectrum. Image is form
http: //coolcosmos.ipac.caltech.edu/cosmic_classroom/multiwavelength_astronomy.

1.3.1 *IRAS*

The Infrared Astronomical Satellite (*IRAS*) was the first space-based observatory to perform a survey of the entire sky at infrared wavelengths. It was launched on 25 January 1983 and performed a successful all-sky survey between 12 and 100 μm. This completely changed the previous picture of the universe by detecting many IR luminous stars and galaxies in the sky for the first time (Soifer et al., 1987). It mapped the entire sky and found about 25,000 galaxies (Chester, 1986). The Ultra-Luminous Infrared Galaxies (ULIRG's) which IRAS uncovered are the most actively star-forming objects in the local universe (Sanders & Mirabel, 1996). All these exciting new sources and results attracted more attention in this field and greatly encouraged detailed study of the dust emission.

With all these excitements, there also come problems. *IRAS* observed only up to 100 μm which is dust at about 20 K, and missed the colder dust emission which is at longer wavelength. It also had poor resolution of is a few arcmin. Devereux & Young (1990b) calculated the gas-to-dust ratio using the *IRAS* data by the following method:

The mass of molecular hydrogen is derived from the gas column density. The mass of dust was calculated with the Hildebrand (1983) equation. The following equation is a simplified version:

$$\mathrm{M}_{dust} = \frac{D^2 f_\nu}{k_\nu B_\nu(T)}, \tag{1.1}$$

where:

D: Distance from the observer to the location of dust

f_ν: Dust emission flux density at frequency ν

κ_ν: Emissivity at ν

$B_\nu(T)$: Blackbody emission curve for dust emission at temperature T (assuming dust emits as a blackbody).

The temperature of the dust was estimated from the *IRAS* 60~100 μm data.

The gas-to-dust ratio measured from *IRAS* data was 1080±70 (Devereux & Young, 1990b). This is far higher than the currently-accepted value of 100∼200 within the Milky Way galaxy (Tielens, 2005). The gas-to-dust ratio of of the local galaxy is measured in two ways: one is by comparison of the gas column density to dust the extinction, another is by the depletion of metals in the ISM.

The high gas-to-dust ratio from the *IRAS* data means that the estimated temperature is too high. The *IRAS* data did not constrain the Rayleigh-Jeans side of the SED because it only measured dust emission up to 100 microns. Fig. (1.9) showed this relation.
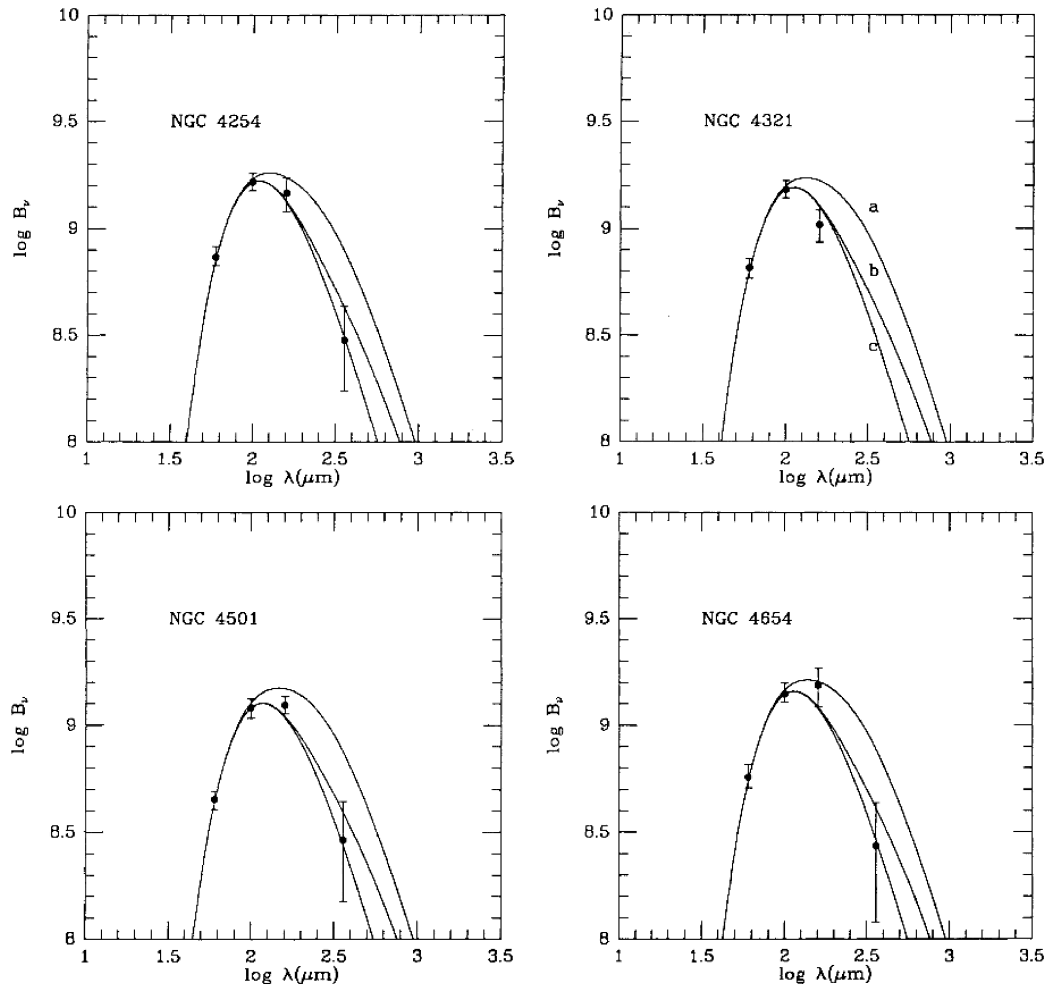
Figure 1.9: The above four figures compared the far-infrared photometry with three models for the dust emission for four galaxies. Model a: 90% of dust mass is 15 K, 10% of dust mass isin a warm component. Model b: 90% of dust mass is 10 K,10% of dust mass is in a warm component. Model C: 'Warm' dust component in single temperature. The temperature of the warm component is derived from the IRAS $S_{100\mu m}/S_{60\mu m}$ flux ratio. The plots are with 1σ error bars with observed 60, 100(IRAS), 160,and 360 μm fluxes. The scale on the vertical axis is arbitray. (a) n=1 emssivity law. (b) n=2 emissivity law. (Devereux & Young, 1990b).

So, the drive to provide higher-resolution images at wavelengths where dust peaks led to the launch of other space telescopes.

1.3.2 *ISO*

The Infrared Space Observatory *(ISO)* was launched on 16 November 1995 by the European Space Agency (ESA). *ISO* was the first observatory to perform an all sky survey at infrared wavelengths. It operated at wavelengths from 2.5 to 240 μm (Kessler, 1995).

ISO provided a better angular resolution than the IRAS survey. At 100μm, the resolution is 2 arcmin. Through ISO observations at 12 μm, the rings, spiral arm fragments, knotted spiral arms, and bright sources in the disks of some galaxies were found to found to be brighter than the nuclei (Bendo et al., 2002). This means the peak of dust emission does not have to be in the same places as the optical emission and showed the important correlation of dust and star forming regions.

ISO measured at longer wavelength than *IRAS*. It detected dust at colder temperature hence allowed gas-to-dust ratios to be determined more accurately. The measurement at 160 and 240 μm seems to be located at the Rayleigh Jeans side of the dust emission curve instead of the peak, while we know the *IRAS* measurement was at the Wien's side of the curve. This straddled the peak of the dust emission.

However, the *ISO* measured temperature is still above 15 K, and the of dust emission at lower than 15 K that radiates primarily at >200 μm may have been missed. Also, the sensitivity of *ISO* was very poor (Tuffs et al., 2002; Haas, 2000).

1.3.3 *The Spitzer Space Telescope*

With the strong calling for higher sensitivity at infrared wavelengths, the Spitzer Space Telescope was launched on 25 August 2003. Its MIPS photometer observed at wavelengths of 24, 70 and 160 μm (Werner et al., 2004). It performed at much higher sensitivity, and provided good science data at wavelengths between 3.6 and

160 μm. Its 1σ sensitivity of 130 mJy in one second at 160 μm (Latter, 2006), was much better than *ISO* which was 640 mJy in one second for 1σ (Laureijs et al., 2003).

The excellent observations provided by *Spitzer* explored much cooler dust than *IRAS*. The dust mass calculated by equation (1), shows the relation of dust emission to its temperature. The gas-to-dust ratios derived from *Spitzer* are about 100-200 which is within the range of the accepted value from most galaxies (Draine & Li, 2007).

Though the gas-to-dust ratio from *Spitzer* data is consistent with accepted values, it may still miss the colder dust emission at <15 K which emits at >200 μm. In order to find out the true nature of dust, colder dust needed to be observed which means observations at longer wavelength needed to be carried out.

1.3.4 *The Herschel Space Telescope*

The *IRAS*, *ISO* and *Spitzer* telescopes are sensitive to dust emitting between 5 μm and 200 μm in the mid to far-infrared, which only give information about hot dust. The longest wavelength coverage by *Spitzer* is still just sensitive to dust warmer than 15 K (Draine & Li, 2007; Draine et al., 2007). Strong empirical evidence shows that much of the dust was missed by previous surveys as the dust are very cold and emit in longer wavelength than 200 μm (Devereux & Young, 1990a). *Herschel*'s mission is to unveil the property of dust and to find out the role of dust in the evolution of the Universe. One of *Herschel*'s main scientific objectives is to discover the properties of cold dust emitting at wavelength up to 500 μm. *Herschel* has carried out several key projects: The Herschel Reference Survey will focus on study of dust in the nearby galaxies, while several large cosmological surveys will trace dust in the distant universe. This will tell us about the properties of dust in the past (Boselli et al., 2010). *Herschel* was launched in May 2009 and is now producing data (ESA, 2009).

Herschel has three main instruments: PACS, SPIRE and HIFI, which detect wavelength of 70,100, 160, 250, 350 and 500 μm(Barlow et al., 2010). Because my project is mainly based on *Herschel* data, these instruments will be discussed in more detail in the observation part.

1.4 Dust Emission and Star Formation

1.4.1 The complexity of emission from star forming regions

When new stars form, they emit strong UV and visible light. Strong UV emission is a good tracer for star formation. As discussed in Section 1, the ISM contains mainly hydrogen, which is the major material for star formation. So hot young stars are usually surrounded by hydrogen which hasn't been used up during star formation. (See Fig. 1.10.) The UV emission from the young stars gives energies of 10 to 100 eV (the ionisation of hydrogen is 13.6 eV). So the UV will ionise the hydrogen. The recombination of the electrons and hydrogen nuclei will cause a strong Hα line which corresponds to the electron falling from $n = 3$ to $n = 2$. So, Hα is often seen alongside UV emission. Hence Hα can also be a tracer of star formation. However, in most cases, star formation happens inside dusty regions, and the dust cloud will be optically thick at UV and optical wavelengths, including Hα. This means in a lot of star forming regions, we don't observe much of UV or Hα emission but IR and FIR by dust heating. The relation of dust heating and star forming regions makes the study of dust emission important to galaxy evolution theory.

Stars are usually formed in areas which are full of molecular hydrogen and dust. When a young star forms, it is hot with temperature greater than 10^4 Kelvin. It emits energetic ultra-violet photons. These photons have enough energy to destroy the dust grains and ionise the hydrogen that are closely surrounding the star.

So, around the centre region of a newly formed star, there are different layers of ISM as shown in Fig.. 1.10, with according temperatures as shown in Table 1.2. Also, with this physical structure of a young star region, we observe the spectroscopy as shown by Fig. 1.7 (presented in introduction).
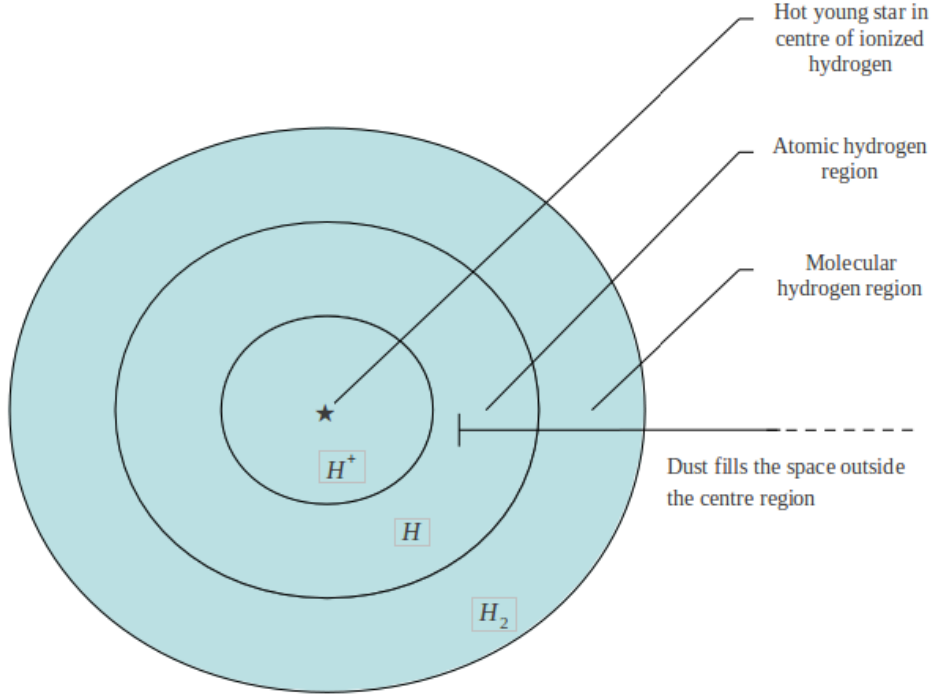
Figure 1.10: Hydrogen location structure of a hot young star region.

Table 1.2: Summary of temperatures of gas and dust out side a hot young star region

region	H^+ region	H region	H_2 region
T_{gas}	10^4 K	10^3 K	10-100 K
T_{dust}	100 K	50 K	10 K

The most inner layer is the ionised hydrogen that is the hot and dense H^+ zone. The electrons have a chance to collide with the protons and emit intensive Hα. This makes the Hα emission become a indicator of star forming regions. In this project, Hα emission images of galaxies were used to indicate the star forming regions.

Outside the centre region of the first layer, Fig. 1.10 shows the transition from fully ionised to fully neutral is very sharp (Stromgren sphere). Molecular hydrogen are deformed into atomic hydrogen by high energetic photons, which forms the H (atomic hydrogen) region in Fig. 1.10. Further out there are unchanged molecular region. Through out the space in the figure there are dust grains.

1.4.2 Dust emission and star formation rate

It used to be a problem for star formation observation as little information could be obtained by optical observation. Now, since the launch of several space observatories which focus on the mid to far-infrared spectra, star formation rates can be estimated from the observed infrared spectra.

Dust emission at 60μm and 100μm from *IRAS*

Devereux & Young (1990c) investigated 124 galaxies from *IRAS* data and compared the 60 and 100μm emission to Hα emission. These galaxies are luminous spiral galaxies chosen from thousands of bright far-infrared *IRAS* sources which also have Hα data from previous optical observations. Fig. 1.11 by Devereux & Young (1990c) shows that the luminosity of the FIR is basically proportional to the luminosity of Hα, which means that the dust emission at 60 and 100 μm is an indicator of star formation. Dust emission at FIR originates from dust heated by star forming regions. Devereux et al. (1995) also investigated 85 independent locations in M81 and also found that its FIR emission regions are 'remarkably similar' to the Hα emission regions. Devereux & Young (1992, 1993) also supported the conclusion that FIR (60 and 100μm) traces star formation. Buat & Xu (1996) investigated 152 disk galaxies that were observed both in UV (200nm) and FIR (40-100 μm) by *IRAS*, with Hubble types from Sa to Scd and Sd-Irr. They all have moderate (0.2-0.9$_{mag}$) extinction in the UV. For Sb-Irr galaxies, the UV (200nm) luminosity produced a good correlation with the FIR (40-100 μm) luminosity hence showing the FIR correlation with star formation rate. Thus, their conclusion is that hot and warm dust (wavelength at 60μm and 100μm) traces the star formation rate.

But Walterbos & Schwering (1987) compared the ratio of 60 to 100 μm with the radius of M31 with the conclusion that they are remarkably constant with radius, As the total stellar population is constant with radius, that result means the hot dust is heated by the total stellar population including evolved stars rather than only the new-born stars. Also, Lonsdale Persson & Helou (1987) researched 54 disk galaxies from *IRAS* data and found that the area of dust heated by evolved stars
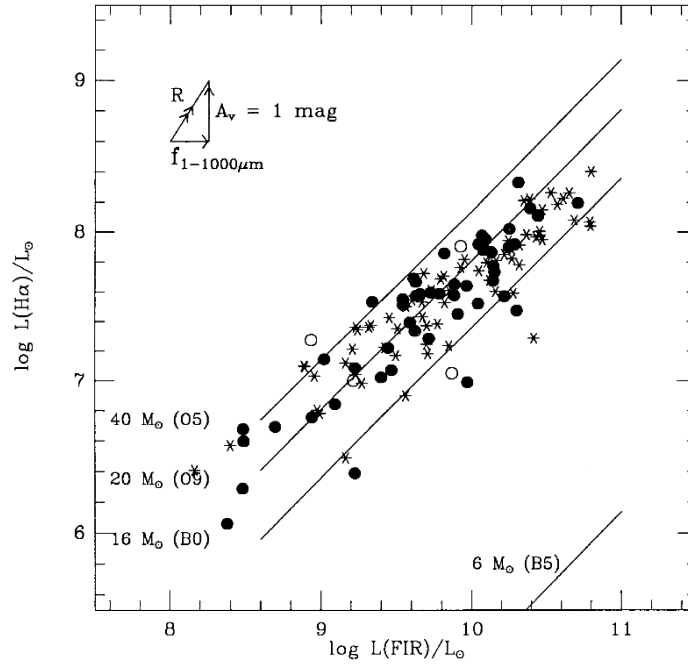
Figure 1.11: Plot shows the Hα emission against the IRAS FIR (40-120μm) emission. Points are coded by $S_{100\mu m}/S_{60\mu m}$ colour. Stars indicate galaxies with $S_{100\mu m}/S_{60\mu m} \leq 2.5$; Filled circles indicate galaxies with $2.5 < S_{100\mu m}/S_{60\mu m} \leq 3.5$; Open circles indicate galaxies with $S_{100\mu m}/S_{60\mu m} > 3.5$. The lines show the ratio $L_{H\alpha}/L_{bol}$ expected for a HII region powered by stars of masses 40,20, 16 and 6 M$_\odot$ respectively (Devereux & Young, 1990c).

and young stars physically overlap.

Sauvage & Thuan (1992) compared the star formation rate of different galaxies to their morphology type and found a decrease of $L_{FIR}/L_{H\alpha}$ from early- to late-type spirals. Fig. 1.12 shows this decrease. Early- type galaxies have a higher $L_{FIR}/L_{H\alpha}$ ratio which means the emission at IR is higher than the star-formation rate represented by Hα. This conclusion is derived from two groups of examples. The left panel used 48 galaxies from Hα luminous galaxies from Kennicutt (1983) (sample I) and the method of using Hα as the SFR indicator. The right panel used 135 galaxies from Romanishin (1990) and Kennicutt (1992) (sample II) and the method of using Hα+[NII] as the SFR indicator. The Hα+[NII] is a corrected star formation indicator which shows more accurate results. The result in panel 2 showed a larger dispersion from result in panel 1. Sa and Sab type galaxies are far from the $L_{FIR}=L_{H\alpha}$ line. Sa and Sb galaxies mainly have low star formation rates. This dispersion shows that the dust emission from Sa,Sab galaxies are from dust
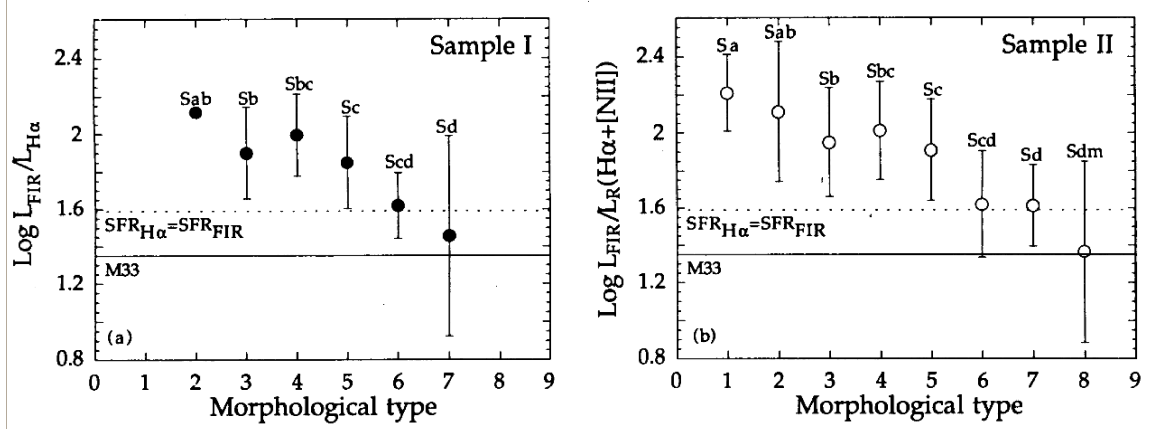
Figure 1.12: Variation of the $L_{FIR}/L_{H\alpha}$ ratio with galaxies morphological type. The panel on the left represents a sample of 48 galaxies. The panel on the right represents a sample of 135 galaxies. Both Hubble and RC3 types (de Vaucouleurs et al., 1991) are shown. The mean value with 1σ dispersion about the mean is plotted for each type. The solid line is the observed ratio in the star-forming regions with highest $f(60\mu m)/f(100\mu m)$ in M33 (Wilson et al., 1991). The dashed line represents to the ratio between the star formation rates derived from L_{FIR} and $L_{H\alpha}$. Both samples show a decrease of $L_{FIR}/L_{H\alpha}$ from early to late type spirals (Sauvage & Thuan, 1992).

heated by the total star population including evolved stars. Beside the difference, both panels show the same results.

Walterbos & Greenawalt (1996) compared the dust model by Desert et al. (1990) to the observed 60 μm and 100 μm radial profiles from *IRAS* data for 10 galaxies. Most of the 10 galaxies show that the observational IR curve is higher than the model predictions which indicates that, for most galaxies, a separate contribution from the O,B stars is adding to the heating of the dust. This conclusion is also supported by Kong et al. (2004).

Dust emission at 24 μm, 70 μm and 160 μm by *Spitzer*

Several calibrations of monochromatic star formation rate indicators at 24 μm were carried out on *Spitzer*'s data. Some observations show that there is a strong correlation between 24 μm emission and the star formation rate (Calzetti et al., 2005, 2007; Prescott et al., 2007; Kennicutt et al., 2007; Zhu et al., 2008). Fig. 1.13 shows the correlation between 24 μm and Paschen α emission which is another indicator of star formation.
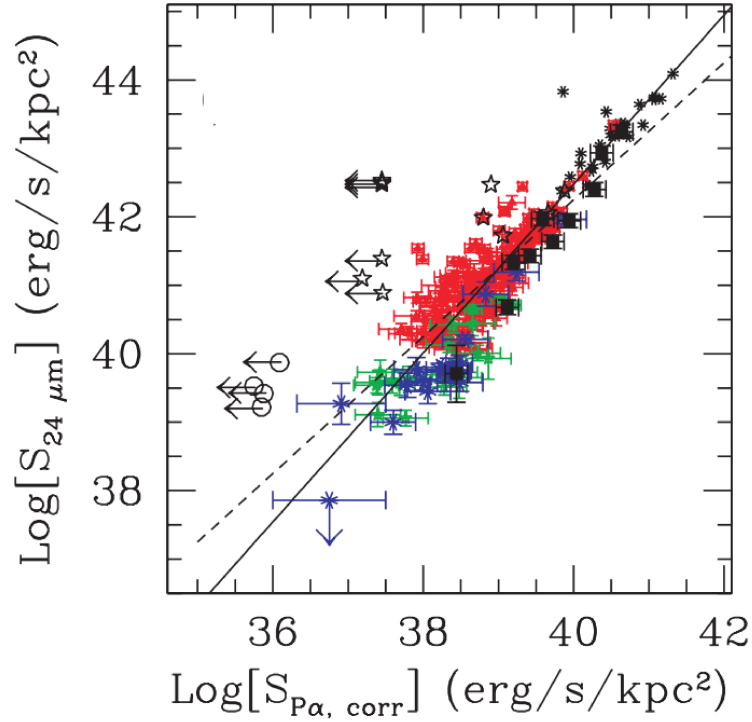
Figure 1.13: 24 μm luminosity surface density (LSD) as a function of the extinction-corrected P_α LSD. The data are from 220 HII knots in 33 galaxies. Data points are divided into three metallicity bins: high (red filled triangles), intermediate (green stars), and low (blue asterisks) oxygen abundance. Filled black squares mark the local star bursts from the sample of Engelbracht et al. (2005). The 3 σ error bars are indicated for each data point. Open black stars indicate the location of the non-thermal sources (Seyfert 2s or LINERs), and open black circles indicate extended background sources. The best-fit line through the high-metallicity (red) data points is shown as a solid line, while the dashed line is the linear fit through the same data points with fixed slope of 1 (Calzetti et al., 2007).

Hinz et al. (2004) found that the infrared emission at 24 and 70 μm agrees closely with the structure of the HII region, which means that it is heated largely by young, ionising stars. But the 160 μm emission matches to the structure of the old red stellar population distribution. Through data analysis of Hα and 24 μm and total IR (TIR) emission (24 to 160 μm), Kennicutt et al. (2009) found that a considerable fraction of the TIR radiation in normal star-forming galaxies is heated by stars older than 100 Myr. 50% of the TIR emission could be from dust heated by the evolved stellar population.

Calzetti et al. (2010) observed a weaker correlation between infrared flux density and SFR with increasing wavelength. In Fig. 1.14, the defination of $\sum_{SFR}$ is
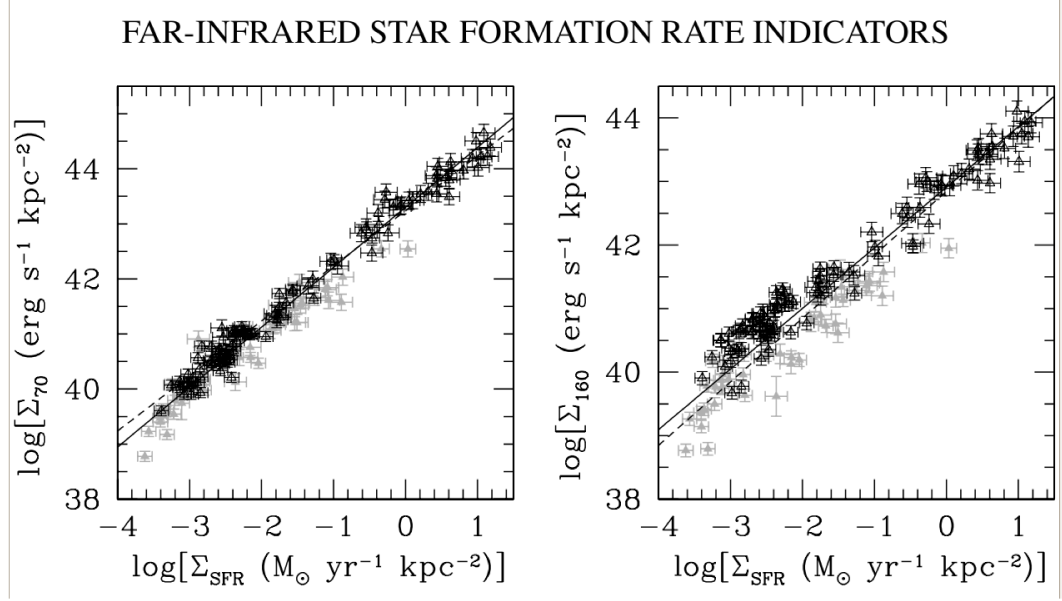
Figure 1.14: 70 μm LSD (left) and 160 μm LSD as a function of $\sum_{SFR}$. The examples are high metallicity galaxies which have been divided into two sample groups accoding to the galaxy's oxygen abundance: 8.1<12+log(O/H)≤8.5 (grey triangles) and 12+log(O/H) > 8.5(black triangles). The continuous and dashed lines in both panels are the best fit and the unity slope lines respectively (Calzetti et al., 2010).

$$\sum_{SFR}(M_\odot yr^{-1}kpc^{-2}) = \frac{\sum_{70}(erg\ s^{-1}\ kpc^{-2})}{1.7 \times 10^{43}}$$

,

for $7 \times 10^{40} erg\ s-1\ kpc^{-2} \lesssim \sum_{70} \lesssim 5 \times 10^{44}\ erg\ s^{-1}\ kpc-2$, and

$$\sum_{SFR}(M_\odot yr^{-1}kpc^{-2}) = \left(\frac{\sum_{70}(erg\ s^{-1}\ kpc^{-2})}{3.3 \times 10^{44}}\right)^{0.65}$$

,

for $6 \times 10^{38}\ erg\ s^{-1}\ kpc^{-2} \lesssim \sum_{70} \lesssim 7 \times 10^{40}\ erg\ s^{-1}\ kpc^{-2}$.

The 160 μm panel shows a serious scatter of data around the trend line than the 70 μm one. This weaker correlation means at longer wavelength, the infrared fluxes have a different heating source other than the young stars. The only explanation is that the longer wavelength dust emission is heated not only by hot young stars, but also by evolved stars.

Dust emission from 100 to 500 μm by *Herschel*

Bendo et al. (2012a) analysed *Herschel*'s data of hot dust emission ($\leq$ 160 μm) and demonstrated that 70/160 μm surface brightness ratios are strongly correlated with Hα emission, which is star-forming region emission, in M81, M83, and NGC2403. 100-250 μm emission from compact sources in M33 was also found to be strongly correlated with star forming regions (Boquien et al., 2010, 2011; Verley et al., 2010). Star forming regions were detected by Hα emission, 24 μm emission or a combination of the two. However at longer wavelengths, researchers have come to a different conclusion.

Bendo et al. (2010a, 2012a) showed that 100 to 500 μm emission strongly correlates with Hα emission only when uses a single wavelength for comparison. However, by the colour temperature method (using wavelength ratio instead of single wavelength), Boquien et al. (2011) showed that the cold dust emission at wavelengths longer than 250 μm traces the total stellar population instead of the star formation. They demonstrated (Fig. 1.15) that 250/350 μm and 350/500 μm surface brightness ratios are more strongly correlated with 1.6 μm emission, which comes from star light. The similarity of the 250/350 μm and 350/500um panel to the 1.6 μm panel indicates that these regions are heated by the total stellar population instead of star-forming regions. Their research on M83 and NGC 2403 shows the same result. These results show that comparing a single wavelength with Hα might not be a good method to indetify dust heating sources.

Galametz et al. (2010) observed NGC 6822, and found is that the ratio of 250/500 μm also peaks in the H II regions. This means the cold dust is heated by the star forming regions in NGC 6822. Since we know that NGC 6822 is a low-metallicity galaxy, this may indicate that the dust heating process at low metallicity is different.

Dust emission longer than 250 μm is classified as coming from cold dust, usually at about 10 to 20K. The dust can be cold if a star forming region is behind a thick dust cloud: the outer dust could not be heated as much as the inner dust close to the star forming region. The cold dust emission is supposed to be a good SFR indicator.
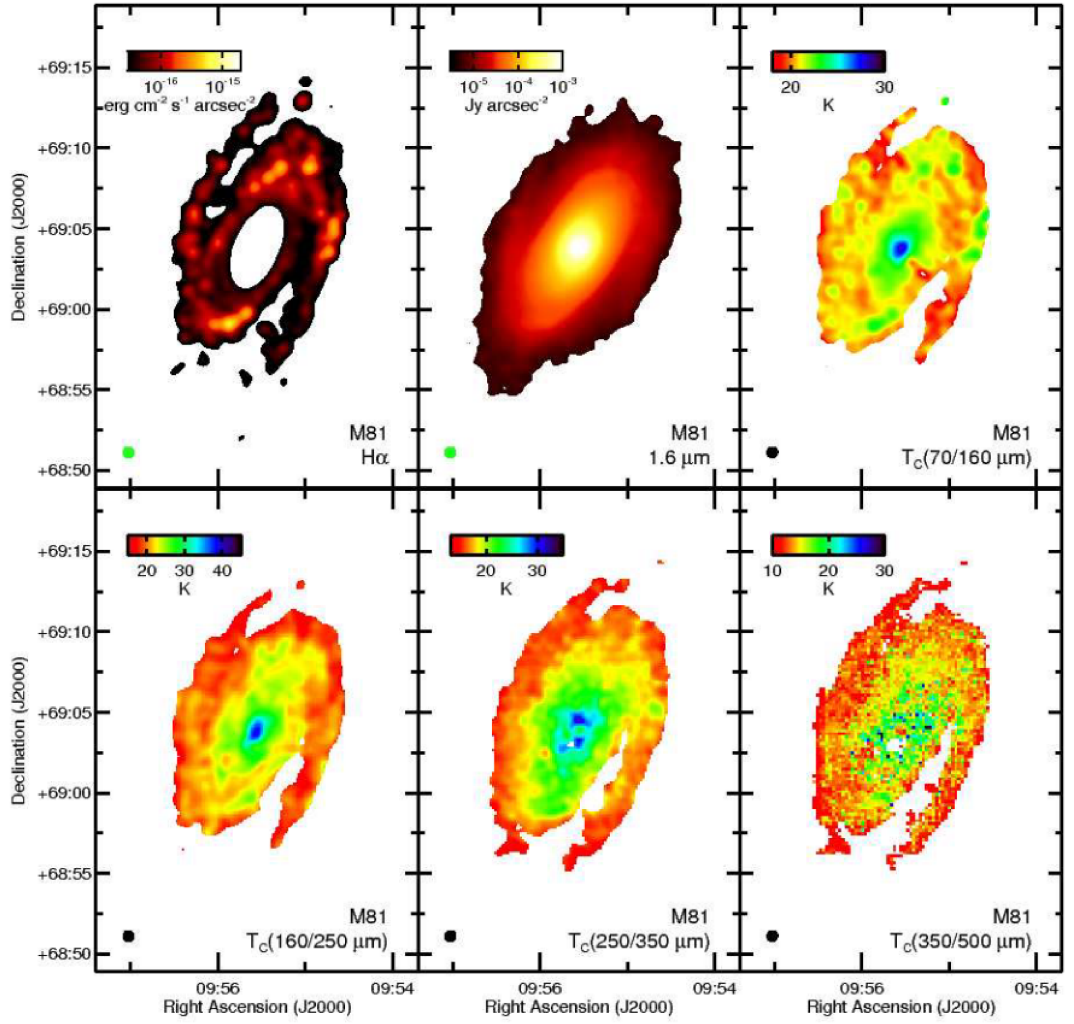
Figure 1.15: Six images of M81 which are the colour temperature of 70/160 μm, 160/250 μm, 250/350 μm and 350/500 μm maps of M81 and Hα and 1.6μm images at the same resolution. All the panels have a FWHM of 36 arcsec shown by the black circles in the lower left corner of each panel. This is because all the maps were created from data where the PSF was matched to the PSF of the 500 μm data. Signals lower than 5 σ were discarded and were left white on the panels. Each map is 30 x 20 arcmin, and north is up and east is left in each panel (Bendo et al., 2012a).

With SFRs as shown by Bendo et al. (2012a), Boquien et al. (2010), Boquien et al. (2011), and Verley et al. (2010), The Schmidt law (Schmidt, 1959) states that SFR $\propto$ Density of Gas. There is also a proportional relation between density of gas and density of dust. This means that the density of dust is proportional to the SFR (Kennicutt, 1998c). High density of dust usually yields a low temperature. Bendo et al. (2012a) and Boquien et al. (2011) explicitly showed that the cold dust emission at wavelengths longer than 250 μm can appear to be correlated with star formation even if the dust is not directly heated by star forming regions.

The data produced by *Herschel* is still being analysed. Early results have already raised the argument of whether cold dust emission should be a indicator of SFR or not, as discussed above. The key point being whether cold dust is heated by star-forming regions or evolved stars.

1.5 Goal of This Thesis

Our understanding of interstellar dust has been exponentially increased after space observatories made IR and FIR observation possible. Thousands of new galaxies, near and far, were found in IR and FIR photometry. The nearby galaxies have been studied in detail for the relationship between their dust emission and star-formation regions. '*Herschel* is observing at much longer wavelengths than other telescopes so made possible the analysis and results described here. Dust emission at 24 μm strongly correlates with star forming regions. This correlation was also found for 60, 70,100, 160, 250, 350 and 500 μm emissions but the relation becomes weaker and weaker. Some studies have shown that dust emission longer than 250 μm is only strongly correlated with the stellar population but not with young stars. Many authors have argued that total infrared dust emission can be correlated with star formation in nearby galaxies, while many others have shown that a significant fraction of the dust in nearby galaxies is heated by evolved star populations. It is important to indicate that the above results are only found in spiral galaxies.

Whether there is star formation in the dust heating area is still a mystery. More detailed research is required in this field. The *Herschel* Reference Survey (HRS) observed 323 nearby galaxies at 250, 350, and 500 μm. These 323 galaxies cover the whole range of morphological types (all Hubble types plus irregular) and environments (from low density field to centre of clusters). They are located within 15 to 25 Mpc (Boselli et al., 2010). The HRS data is good for continuing analysis on dust heating sources and I will be working on these data in colour temperature in later research.

In this thesis, I will examine the far-infrared emission of a number of nearby galaxies. This emission traces the cold dust in the Interstellar Medium (ISM) of the host galaxy. The main goal will be to investigate the heating mechanism of this dust. Dust is heated through the absorption of photons. In regions of recent star formation, the radiation energy is very high, because of the presence of short-lived high mass stars which are very luminous. Star formation therefore provides the conditions for efficient dust heating in their environment. But evolved stars also provide high luminosity environment for dust heating machanism, hence the heated dust can represent different heating source behind it. Through data anylysis of far infrared images of nearby galaxies taken by Herschel Reference Survey, The heating source behind the heated dust is discussed.

Chapter 2

Target Selection and Observations

To study the cold dust emission, we use FIR data from the Herschel Space Observatory at 100, 160, 250, 350, and 500 μm. The galaxies were selected from the Herschel Reference Survey (Boselli et al., 2010), but the Far-infrared data are from the Herschel Virgo Cluster Survey (HeViCS) (Davies et al., 2012). The Hα and 1.6 μm data are also being used for analysis. The Hα images are used to represent the star forming regions which are from Boselli & Gavazzi (2002) and 1.6 μm images are used to represent the total stellar populations. They are from Two Micron All Sky Survey (2MASS) (Jarrett et al., 2003). We also used 24 μm image for foreground star subtraction which is form Bendo et al. (2012b).

The wavelength selection, target galaxy selection and instruments and observation are discussed in this chapter.

2.1 Selected Wavelengths

Dust grains absorb photons emitted by the hot young star and re-emit in infrared and far-infrared. Figure. 1.7 (presented in section 1.2.3) shows a dust emission peak between 100μm to 200μm.

Assuming dust emission is a modified blackbody emission, the dust temperature can be calculated by using Wien's Law (we will discuss other ways of calculating dust temperature in later sections):

$$\lambda_{max} = b/T_{max}$$

where b is the Wien's displacement constant, $b = 2898\mu m$ K

With this relation, if we want to investigate the properties of colder (5 K to 30 K) dust, we need to look into the dust emission at wavelengths from about 100 μm to 500 μm. Also, cold dust beyond 200 μm has been poorly studied before. Herschel data covers 100μm, 160μm, 250,μm 350μm and 500 μm, and the corresponding blackbody temperatures are 29K, 18K, 11K, 8K and 5.8K respectively.

Hα is used to trace star formation. It traces the ionisation by O/B type stars. It also traces ionising photons in either diffuse regions or compact regions (reference to Fig. 1.10 in section 1.4.1). The 24 μm is used for identifying and subtracting stars. 24 μm also traces hot dust at T$\gtrsim$100 K (reference to Table. 1.2) and could also be used for star formation (Prescott et al., 2007). But it also traces very small grains in the diffuse ISM that may be heated by evolved stars (Li & Draine, 2001; Kennicutt et al., 2009), so we only use Hα by itself for tracing star formation.

We choose 1.6 μm data as a tracer for total stellar population for three main reasons:

- It traces emission from all stars including evolved stars and not just star forming region.

- From Figure. 1.7 (presented in section 1.2.3), we see that the total stellar emission peaks between 1 and 2 μm.

- It is not strongly affected by dust extinction.

- It is free from hot dust emission which may be seen at wavelengths as short as 3.6 μm(Mentuch et al., 2009, 2010).

2.2   Targets

The galaxies were selected from the Herschel Reference Survey (HRS), a sample of 323 galaxies observed at 250, 350 and 500 μm with Herschel. The Herschel Reference Survey is a Herschel guaranteed time key project and it focused on the study of dust in the nearby galaxies. 'Nearby galaxies' are defined in HRS as galaxies with distances between 15 to 25 Mpc. The HRS galaxies also have a flux limit of K (λ=2.2μm) band to exclude low mass galaxies, dwarf galaxies and elliptical galaxies. The 323 HRS galaxies have a whole range of morphological types from ellipticals to late-type spirals and environments from the field to Virgo Cluster.

Although the galaxies used in the analysis are from the HRS, the data used for this project originate from the Herschel Virgo Cluster Survey (HeViCS), which has an agreement with the HRS to share data on galaxies falling within both surveys. The data are SPIRE and PACS photometry data. HeViCS covers four 4×4 regions at wavelength 100, 160, 250, 350 and 500 μmusing the SPIRE/PACS parallel scan-map mode.

Since the dust rich galaxies are usually spiral galaxies, to have the maximum data of dust heating, we only chose the face-on spiral galaxies (axial ratio between minor axis and major axis greater than 0.5) of Sb or Sc type, and larger than 5 arcmin from the total samples for my dust heating study. To make sure I have the best targets to work with, I selected them totally from the Herschel Virgo Cluster Survey (HeViCS) (Davies et al., 2012) which are all nearby galaxies. In this way we can see how the dust, stars and star forming regions are distributed within the galaxy even at the resolution of the 500 μm data. The HRS and HeViCS have an agreement to share data for the HRS galaxies in the Virgo cluster. As the HeViCS also contains 100 and 160 μm data, we also use the data for warm-cool dust analysis.
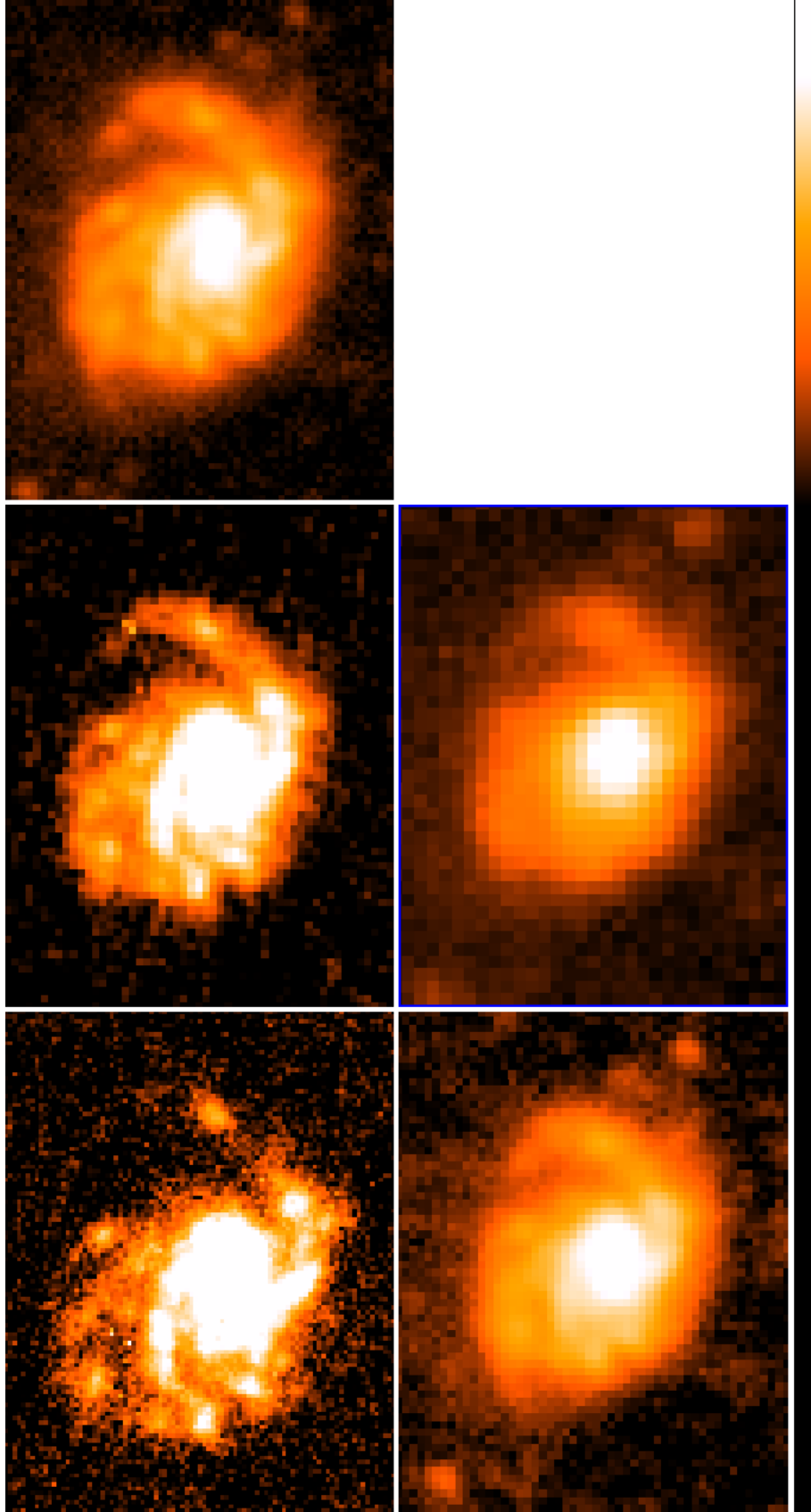
Figure 2.1: Herschel image of NGC4254 in 100μm, 160μm, 250,μm 350μm, 500 μm from top left. The colours are scaled logarithmically. Each image has its own unit so the colour is a relative way to present the emission distribution of dust heating.
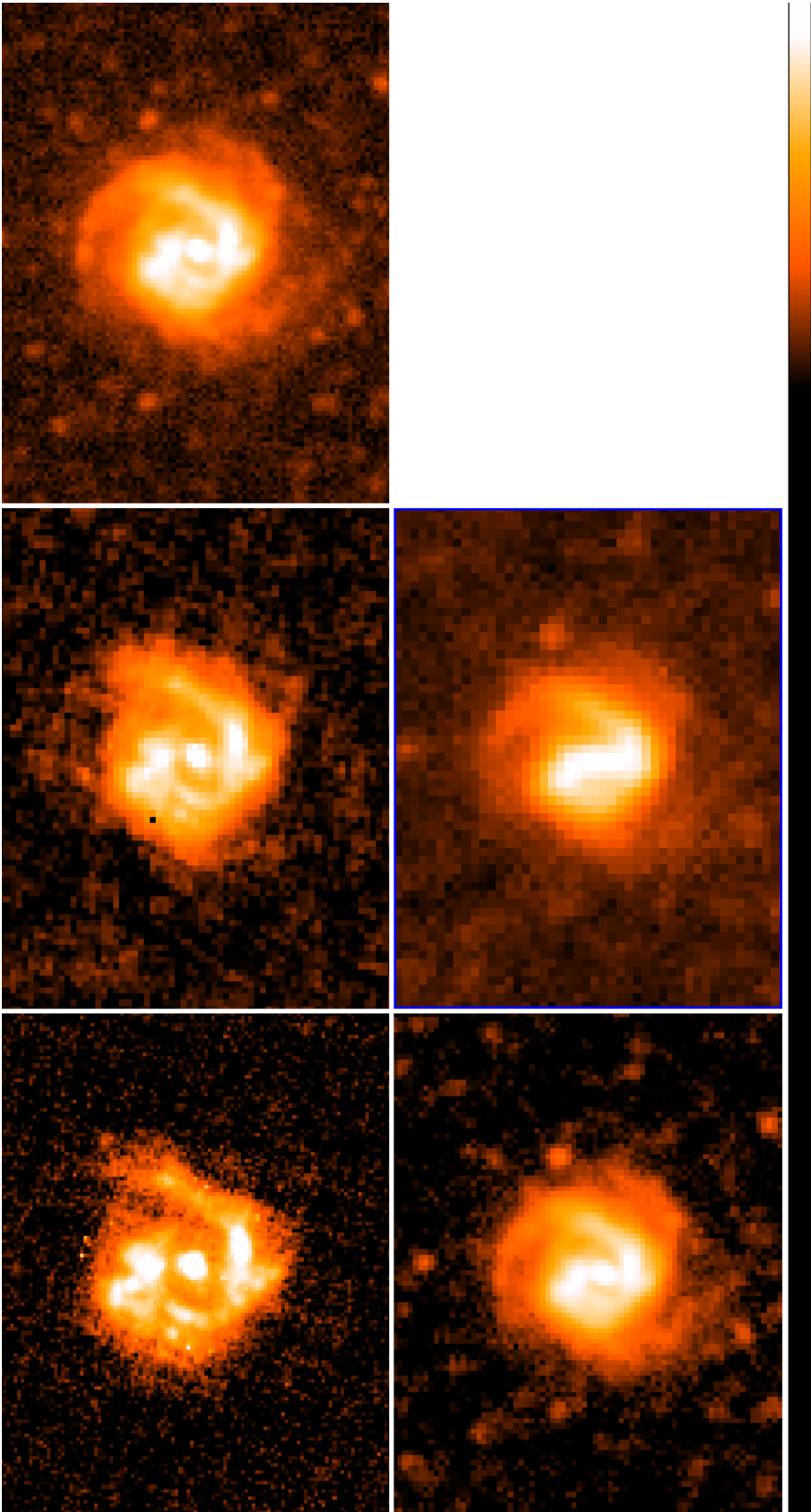
Figure 2.2: Herschel image of NGC4303 in 100μm, 160μm, 250,μm 350μm, 500 μm from top left.
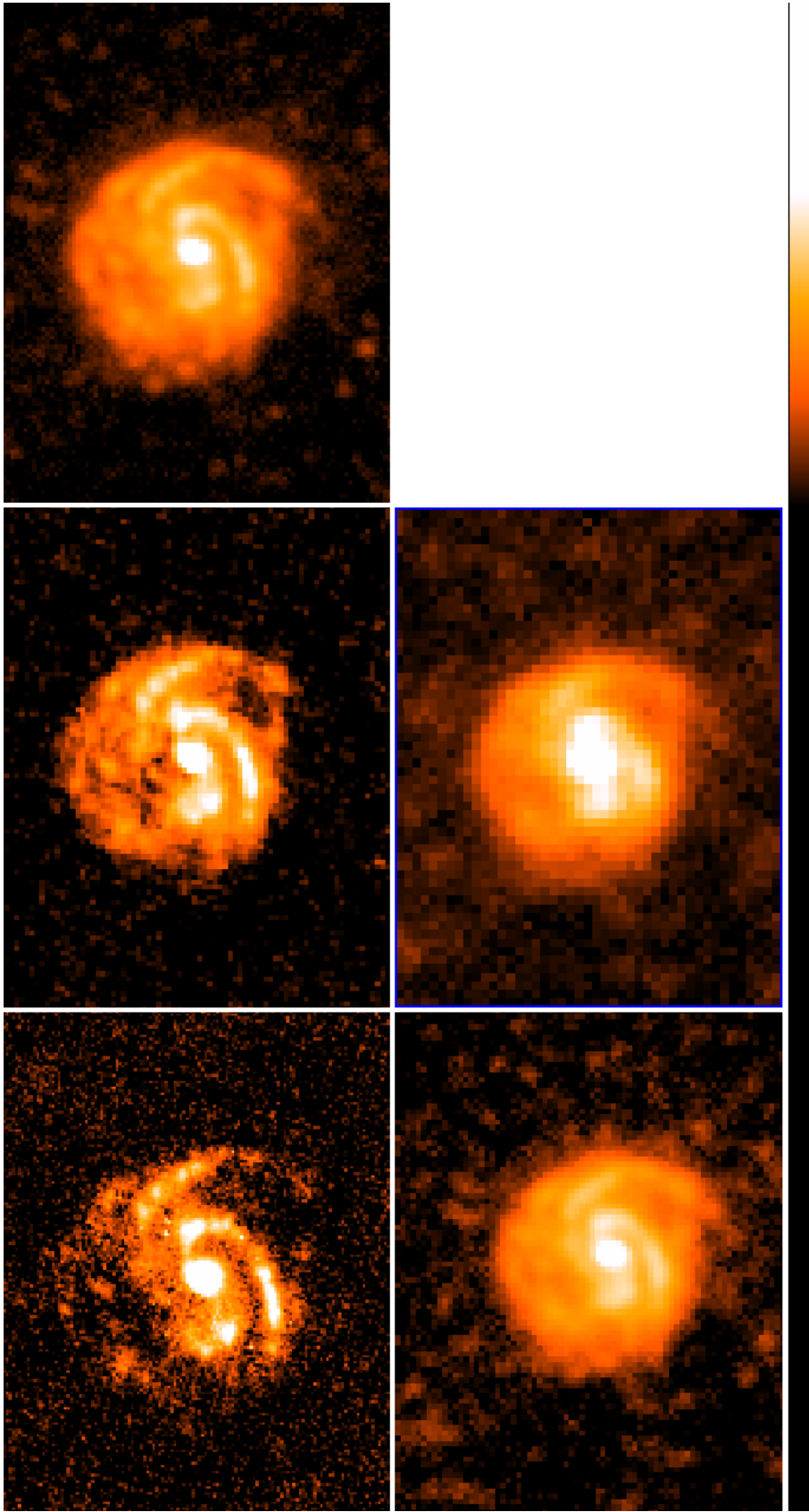
Figure 2.3: Herschel image of NGC4321 in 100μm, 160μm, 250,μm 350μm, 500 μm from top left.
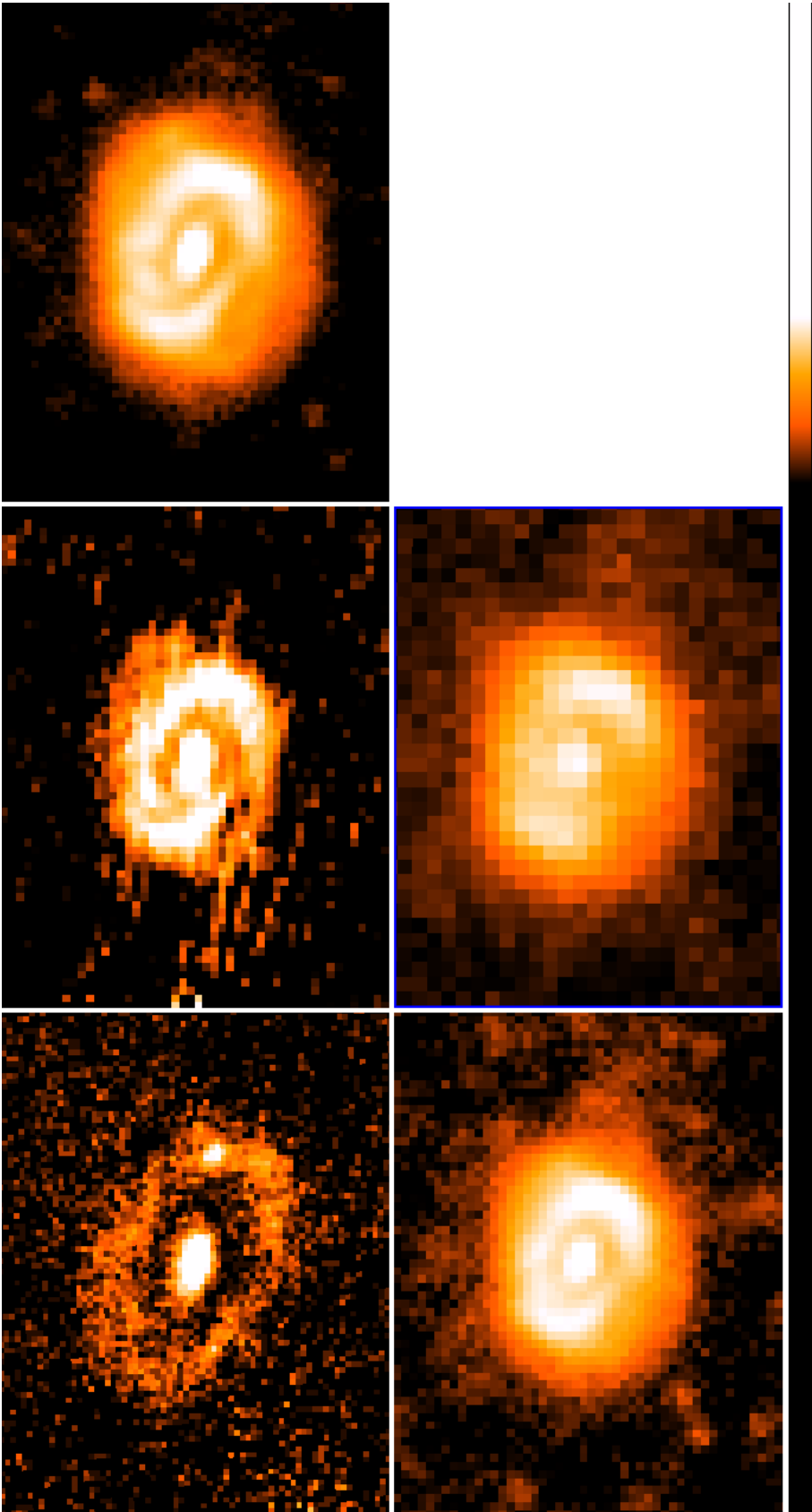
Figure 2.4: Herschel image of NGC4579 in 100μm, 160μm, 250,μm 350μm, 500 μm from top left.

The four galaxies selected with their main physical properties are listed in Table 2.2 with columns arranged as follows (information mainly from Davies et al., 2012; Boselli et al., 2010):

Column (1): New General Catalogue (NGC) name;

Column (2): J2000 right ascension of position;

Column (3): J2000 declinations of position;

Column (4): Heliocentric radial velocity in km s^{-1};

Column (5): Morphological type;

Column (6): Major and Minor axis in arcmin;

Column (7): Distance.

Table 2.1: The four galaxies chosen for analysis from Herschel Reference Survey.

(1) Name	(2) RA (J2000)	(3) Dec. (J2000)	(4) v (km s^{-1})	(5) Type[5]	(6) Major and Minor axis[5] (arcmin)	(7) D (Mpc)
NGC4254	12:18:49.7	14:25:10.8	2404	SA(s)c	5.4×4.7	14.4[1]
NGC4303	12:21:55.1	04:28:27.8	1566	SAB(rs)bc	6.5×5.8	16.8[2]
NGC4321	12:22:54.9	15:49:24.8	1575	SAB(s)bc	7.4×6.3	15.2[3]
NGC4579	12:37:43.5	11:49:05.5	1520	SAB(rs)b	5.9×4.7	16.6[4]

*Most information are from NED website.
(1) SNII optical, Distance reference: Poznanski et al. (2009)
(2) Tully-Fisher based on HI data. Distance reference: Schoeniger & Sofue (1997)
(3) Cepheids, Distance reference: Freedman et al. (2001)
(4) Tully-Fisher. Distance reference: Springob et al. (2009)
(5) Information from de Vaucouleurs et al. (1991)

The Herschel far-infrared images of the four galaxies in five bands are shown from Fig.2.1 to Fig.2.4. The 100 and 160 μm images are taken by the PACS instrument and the 250, 350 and 500μm images are taken by the SPIRE instrument on Herschel.

In each map, north is up, and east is left. These images are original images without being convolved or any other data process mentioned in this project. All the galaxy images show enhancement of emission in the galactic core area and the spiral arms. The structure of the core and spiral arms is more clear in shorter wavelength images like the 100 and 160 μm images and becomes less clear when the wavelengths get longer. This because at shorter wavelength the image have a better resolution (R=λ/D).

The 160 μm image of NGC4321 shows some sharp triangle like dark black area at the top left inside the galaxy optical disk. The 100 μm one seems also to have this extra dark area while the images taken by SPIRE doesn't have this. This indicates that the PACS image may be effected by data processing artifacts in that area. This error will be dealt with during data preparation.
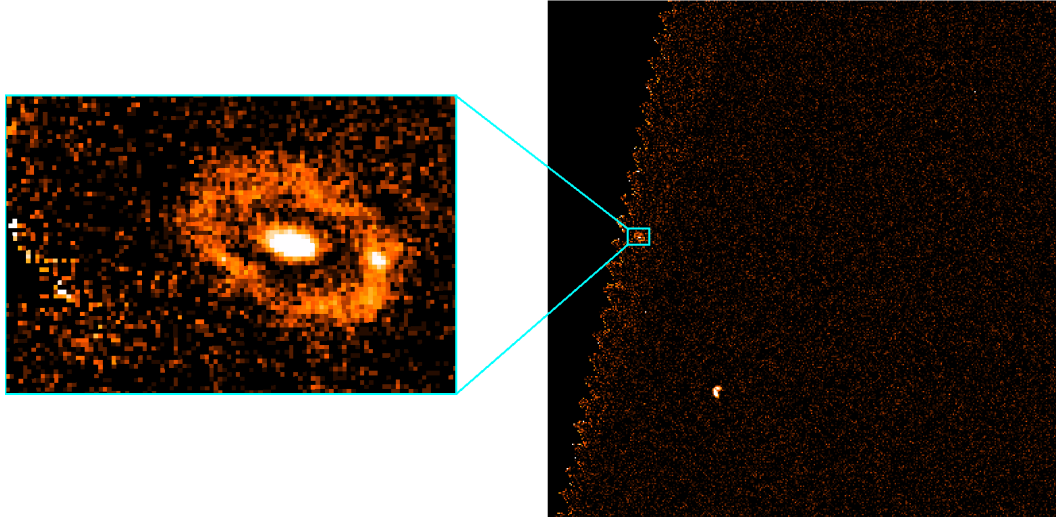
Figure 2.5: The edge location of NGC4579 at SPIRE image of Virgo A.

We can see that the 100 and 160 μm images of NGC4579 in Fig.2.4 are more noisy than the other 100 and 160 μm images in other galaxies. They look more noisy and unclear even than the 250, 350 and 500 μm images though the later ones

have lower resolution. This is because this galaxy is located at the edge of PACS scans from the Virgo A image and it has poor coverage as an effect of exposure time as shown in Fig. 2.5. This is not a problem in SPIRE images because it is not at the edge in the SPIRE image of Virgo A.

2.3 Instruments and Observations

2.3.1 PACS Instrument

The PACS instrument is shown in Fig. 2.6. The 100, 160 μm data in this project is observed by PACS instrument on Herschel Space Telescope. The PACS instrument has two modes: photometry and line spectroscopy. We use photometer maps of the PACS instrument.
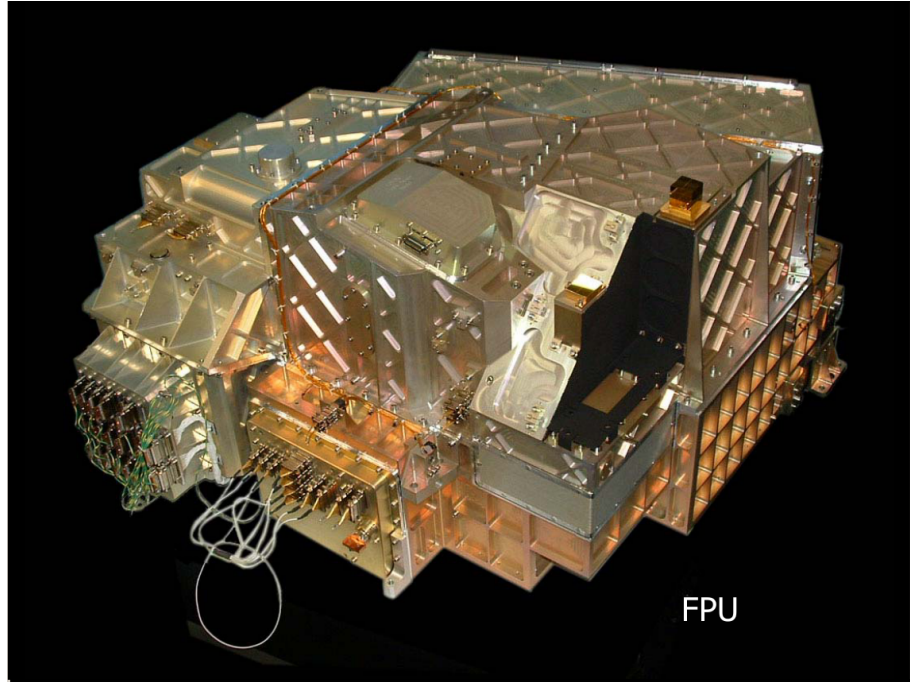
Figure 2.6: The PACS instrument. Picture from $http://herschel.esac.esa.int/science\_instruments.shtml$.

The PACS field of view is 1.75×3.5 arcmin. The imaging photometry have two bands operating simultaneously (70 μm and 160 μm or 100 μm and 160 μm) with dichroic beam splitter. Two filled bolometer arrays (32×16 (red) and 64×16 (blue) pixels, full beam sampling). The 100 μm image is taken by 'Blue Photometer'

Table 2.2: PACS Performance From the PACS Observer's Manual.

λ	100 μm	160 μm
FWHM of PSF (parallel mode)	6.98 × 12.7 (arcsec)	11.64× 15.65 (arcsec)
Flux calibration uncertainty	3%	5%

Camera and the 160 μm image is taken by the 'Red Photometer' Camera. The photometer focal plane geometry/distortions are determined with a bout 1/20 pixel accuracy. For small source photometry, use small 2×2 raster and 200"× 100" field of view (FOV)(Poglitsch et al., 2010). The key parameters of PACS [1]are stated in Table 2.2.

2.3.2 SPIRE Instrument

Fig. 2.7 shows the picture of the SPIRE instrument. The 250, 350 and 500 μm data are from SPIRE instrument. SPIRE has large field of view ($4\prime \times 8\prime$). Its sensitivity is about 7mJy, 5σ in 1 hour in point source mode (from the SPIRE Observer's Manual[2]).The key parameters of SPIRE are stated in Table 2.3.
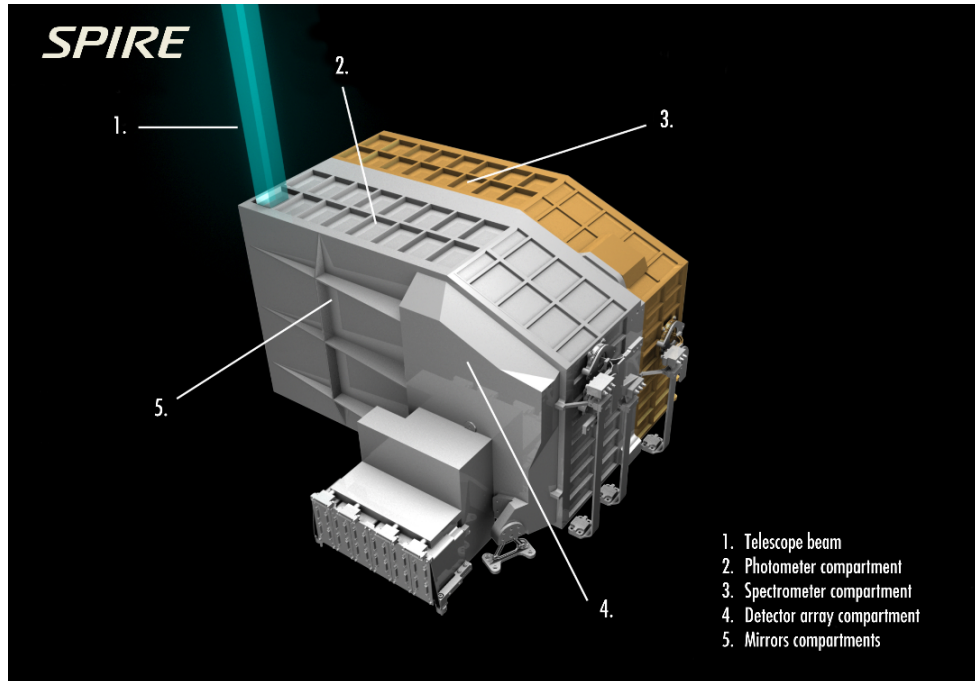
Figure 2.7: The SPIRE instrument. Picture from
$http://herschel.esac.esa.int/science_instruments.shtml$.

---

[1]Information from the PACS Observer's Manual: $http$: $//herschel.esac.esa.int/Docs/PACS/html/pacs\_om.html$
[2]The SPIRE Observer's Manual website: $http://herschel.esac.esa.int/Docs/SPIRE/html/spire\_om.html$

Table 2.3: SPIRE Performance From the SPIRE Observer's Manual.

λ	250 μm	350 μm	500 μm
Angular Resolution	18.2"	24.9"	36.3"
Flux calibration uncertainty	7%	7%	7%

SPIRE have both spectral and photometric modes. The images we used in this project are photometric.

2.3.3 Observations

The 100, 160, 250, 350 and 500 μm data used in this project are all obtained with the Herschel space observatory (shown in Fig. 2.8) observed between November 2009 and July 2011 and processed through the HeViCS pipeline in July 2011.

The HeViCS data are obtained using the SPIRE/PACS parallel scan map mode. The parallel scan map mode means the PACS and SPIRE instrument image the sky simultaneously. The 100, 160, 250, 350 and 500 μm data are obtained at the same time. The settings are nominal detector and a fast scan rate of 60 arcsec s^{-1}. The scan is set to two orthogonal cross-linked scan directions. Each region was observed four times using these settings.

Figure 2.8: The Herschel Space Observatory. Picture from
$http://herschel.esac.esa.int/science\_instruments.shtml$.

2.3.4 Data processing

PACS data reduction used the standard pipeline for both the 100- and the 160-μm channels. The two orthogonal scans were combined, and the maps are made using the naive map-maker. For more details see (Davies et al., 2012).

The SPIRE photometer time-line data were processed with a custom-driven pipeline script. This script is adapted from the official pipeline. A custom method called BriGAdE (Smith et al., 2010) is used to remove the temperature drift. The two orthogonal scans were combined, and the maps are made using the naive map-maker as the same with the PACS data processing (Davies et al., 2012) .

The FITS data is generated by Herschel software - HCSS Fits Product Version.

2.4 Complementary Data, the Hα 1.6 μm and 24 μm images

2.4.1 Hα Instrument and Observations

Hα ($\lambda = 6562.8\mathring{A}$) images is used as a tracer of the star formation area in the galaxies. I tried to use different versions of Hα images from NED Knapen et al. (2004); Kennicutt et al. (2003) with maximum of a FOV of 10.4$\times$10.4 arcmin but they are too small for my research and some of them have a background that are not flat. The images are smaller than 1.5 times the optical disc so does not have enough space outside the optical disc for background subtraction. All the Hα images used for data analysis in this project are from Boselli & Gavazzi (2002). They are obtained at the 1.2 m Newton telescope of the Observatoire de Haute Provence (OHP;France)in 1998 and 2000. The OHP telescope has $f/D = 6$ with a thinned TK1024$\times$1024 pixels CCD detector. The pixel size is 0.69 arcsec. The observation was through two narrow band interferometric filters. One filter included the redshifted Hα line (ON) and the other measured the red continuum near Hα (OFF). The integration time is 30-45 min ON- and OFF- band, generally split in 3 shorter exposures(Boselli & Gavazzi, 2002). We worked with Hα images where the continuum subtraction

had been applied.
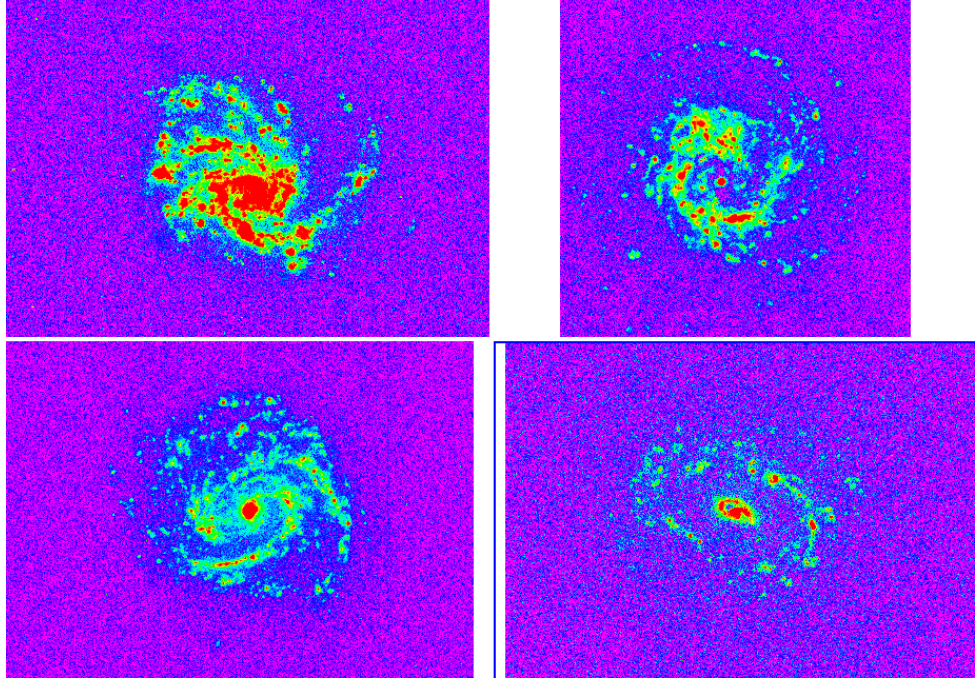
Figure 2.9: Original Hα images of the four galaxies for analysis. The order from top left to right is NGC4254, NGC4303,NGC4321,and NGC4579. The DS9 setting for these images in scale are log and ZMax, colour set in Rainbow.

The images are downloaded from the GOLDMine website. [3] These Hα images for the four galaxies are represented in Fig.2.9. .

2.4.2   1.6 μm Instrument and Observations

The 1.6 μm images for the four galaxies are represented in Fig.2.9.

These images are from the Two Micron All Sky Survey (2MASS) (Jarrett et al., 2003). The observations were conducted during 1997 and 2001 from two 1.3 m diameter telescopes located at Mount Hopkins, Arizona, and Cerro Tololo, Chile. The integration time is 7.8 seconds which yielded a 10 σ point-source detection level. Bright source extractions have 1 σ photometric uncertainty of <0.03 mag. Calibration offsets between any two points in the sky are <0.02 mag (Skrutskie et al., 2006).

The 1.6μm contains many foreground stars which needed to be removed from the image so the flux of star light which is not part of the galaxy image would not

---

[3]the GOLDMine website: $http://goldmine.mib.infn.it/db/byname.py$.
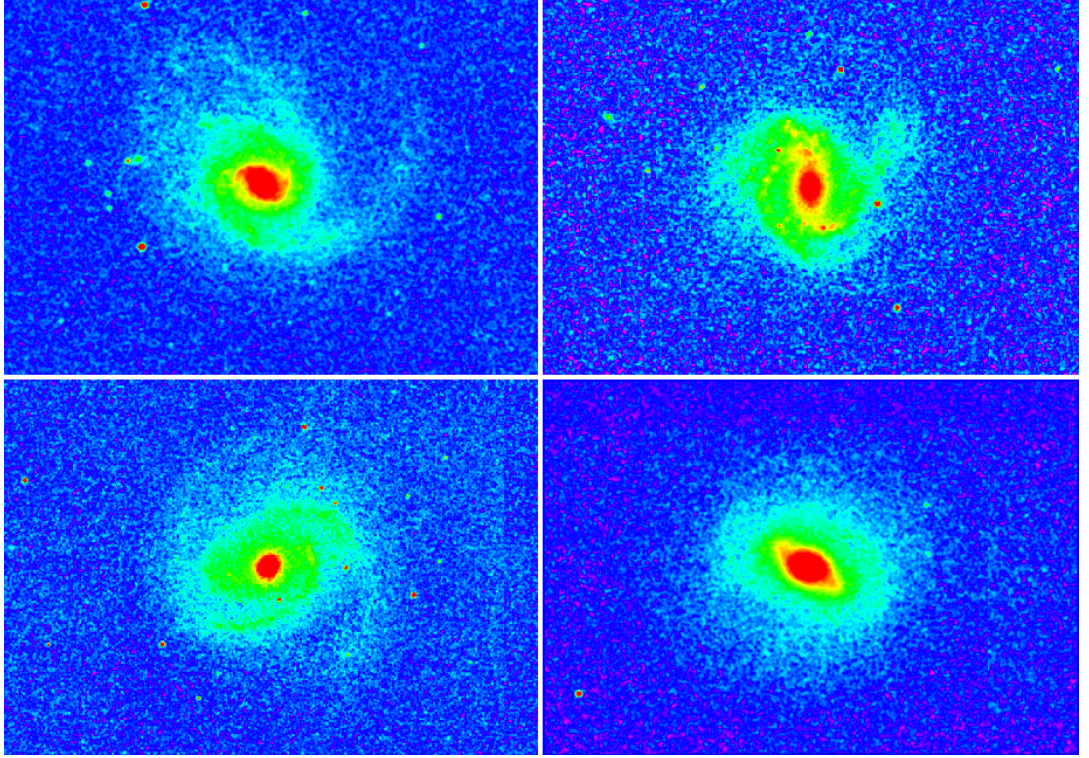
Figure 2.10: Original 1.6μm images of the four galaxies for analysis. The order from top left to right is NGC4254, NGC4303,NGC4321,and NGC4579. The DS9 setting for these images are LOG and ZMAX in scale and colour set in RAINBOW.

influence the result of the galaxy flux data analysis. This is done in the following chapter.

2.4.3 24 μm

The 24 μm image were used for star filtering in data preparation. The images are from the Multiband Imaging Photometer for Spitzer (MIPS) instruments from Spitzer Space Telescope (Bendo et al., 2012b). Bendo et al. (2012b) created these images from archival raw Spitzer Space Telescope data. The data were processed using the MIPS Data Analysis Tools (Gordon et al., 2005) along with additional custom processing steps. Additional details are given by Bendo et al. (2012b).

Chapter 3

Data Preparation

As described in Chapter 2, we have a range of galaxies observed at different wavelengths. The observed wavelengths for data analysis are: Hα, 1.6μm, 100μm, 160μm, 250μm, 350μm and 500μm. Because these data are taken with different instruments, they all have different pixel sizes and resolution, and the pixel values are given in different units.

The data analysis method used in this project requires these different images comparable so the data need to be converted. This chapter describes in different section how data preparation is carried out including removing foreground stars, unit conversion, convolution of data, subtract background, rebin and data selection. At the end of this chapter, we also discussed how to deal with image problems and how to remove bad data.

3.1   Remove foreground stars from the original image

It is important to subtract the foreground stars because they are not part of the galaxy which is to be analysed and would affect the photometry of the galaxy. The Hα images and the 1.6μm images have foreground stars which need to be subtracted before subsequent photometric analysis. We used the 24 μm image as a comparison image to locate the foreground stars. This is because stars are very
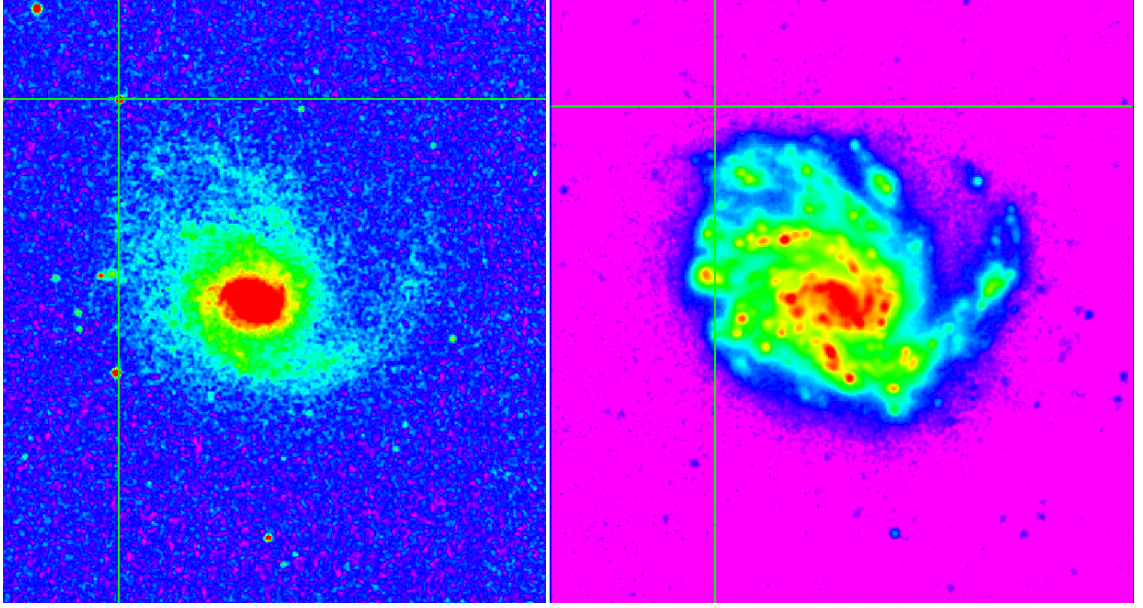
Figure 3.1: The technique used to located foreground stars by DS9. The cross hair at the top left corner of both panel are the same WCS which locate a star shown in the 2MASS image on the left panel and not shown on the 24 μm on the right panel.

hot (in comparison) and peak in visible bands and 24μm is in the infra-red where their emission is much fainter. So most foreground stars are not shown in the 24μm image. We assume that the point sources which appear in the Hα image and the 1.6μm image but do not appear in the 24μm image are foreground stars. The procedure used is by opening the Hα or the 1.6μm image and the 24μm image in Tile Frames (multi-window mode) of DS9 and then lock the cross hair with the World Coordination System (WCS) which shows the declination and right ascension of the pixel. Then the location of the foreground stars are read off in the Hα or the 1.6μm image. Fig. 3.1 shows how the 1.6 μm 2MASS image of galaxy NGC4254 is compared with its 24 μm image to identify the foreground stars.

Through comparing the bright point sources that appear in the 2MASS galaxy image of NGC4254 but not shown in the 24 μm image, the foreground stars are located and marked in circles and the position and size of these circles are saved in a region file. The size of the circles are made sufficiently small so they will not have a significant influence on the image. After saving the region file, an IDL program is used to call this region file to locate the marked circles and to subtract the circled areas. The circled regions which are subtracted are refilled by interpolating the
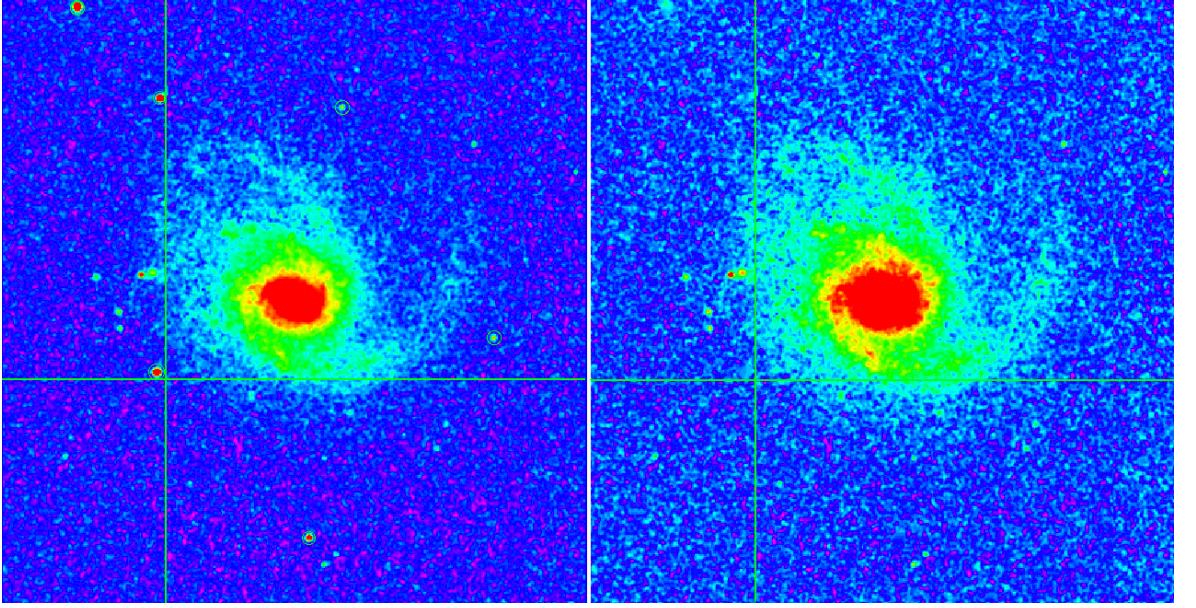
Figure 3.2: The left image showing the star regions marked by circles of the 2mass image of NGC4254, the right image shows the same image with stars filt.

background through the region using the value of the pixels at the edge of the circle. In this way the stars are removed without leaving dark "holes" in the images. Fig. 3.2 shows a comparison of images before and after stars are subtracted.

3.2 Unit Conversion to Jy/arcsec^2

To make the images comparable, the units of the different images will be all converted to Jy/arcsec^2 from the different units of the original images.

3.2.1 Conversion of Hα FITS images

The original unit in the Hα images are image counts, from the HEADER information. To convert image counts to surface brightness, I need the ratio Jy/image count and need to find out the total square arc-second per pixel. The formula to calculate the total flux is found in the HEADER information of the Hα FITS file. I will take the HEADER information of the Hα FITS image of NGC4254 as example.

From the HEADER information we find that the total flux is in unit of erg.cm^{-2}.s^{-1} and the formula for flux is:

$$\log Flux = zp + \log(Cnts) - \log(Texp) \tag{3.1}$$

where zp is the zero point given in HEADER as 'P_ZEROPO=-14.36'; logCnts is the logarithm of the image counts given in the image; Texp is the exposure time in seconds which is given in the HEADER as 'TM-EXPOS=1800.01'.

The image counts in the image have negative numbers because of the continuum subtraction which will make the result of logarithm not a number. The above formula is converted to the following

$$Flux = 10^{zp} \times Cnts/Texp \tag{3.2}$$

To change the unit of the flux from erg.cm^{-2}.s^{-1} per pixel to Jy.arcsec^{-2} I used the following transformation

1 erg cm^{-2} s^{-1} = 10^{-7} Watt s /10^{-4}m^{-2} s^{-1} = 10^{-3} Watt m^{-2}

1 Jy = 10$^-$26 Watt m^{-2} Hz^{-1}

So, to convert the unit

1 Jy = 10^{-23} erg cm^{-2} s^{-1} Hz

So, the transform equation used in unit conversion is:

$$\frac{F_\nu(old)}{[\text{erg.cm}^{-2}.\text{s}^{-1}]} = \frac{F_\nu(new) \times 10^{23}}{[\text{Jy.Hz.arcsec}^{-2}]} \tag{3.3}$$

The final unit is converted to Jy.Hz.arcsec^{-2} from erg.cm^{-2}.s^{-1} per pixel. The conversion of pixel to arcsec^2 is derived from the HEADER information as 1 pixel = 0.69 arcsec. I did a comparison of the value at the same point with coordination of declination 12 : 18 : 52 : 770 and right ascension 14 : 25 : 46 : 88 of the Hα image of NGC4254. It shows the value before unit conversion was 2050.76 erg.cm^{-2}.s^{-1}. The value after unit conversion is $1.06077e - 14$ Jy.Hz.arcsec^{-2}.

The program I wrote to convert the unit of Hα images is in the Appendix A.1.

3.2.2   1.6μm FITS images

The unit of the 1.6μm images is converted to the unit of $Jy/arcsec^2$ by a given program using

$$img = img \times 1050. \times 10^{(-sxpar(head,'HMAGZP')/2.5)}$$

where sxpar extract the value of the zero point in the header information of the FITS file, and 1050 is the flux density in Jy at magnitude 0 (Cox, 2000, From table 7.5).

3.2.3   100μm, and 160μm FITS images

The unit of 100μm, and 160μm FITS images are in $Jy/pixel$. The pixel size can be derived from multiplying the length of the side of the pixel which is given in the HEADER information by CDELT1 and CDELT2. The unit of CDELT1 and CDELT2 are in degree. So to convert $pixel$ to $arcsec^2$ I used the the following equation:

$$1 pixel = CDELT1 \times CDELT2 \times 3600 \times 3600 arcsec^2 \qquad (3.4)$$

Then, the unit can be changed to $Jy/arcsec^2$ simply by dividing by the above computational result.

3.2.4   250μm, 350μm and 500μm FITS images

The unit of 250μm and 500μm FITS images data are in Jy/beam found from the HEADER information 'QTTY=Jy/beam'. The beam size in arcsec^2 is shown in Table. 3.1 which is obtained from the SPIRE Observers' Manual (ESA, 2011).

To get an accurate result of new unit Jy/arcsec^2, we used colour correction. The

Table 3.1: Basic 2-D Gaussian parameters for measured beams on maps with a 1 arcsec pixel size. Uncertainties in the beam FWHM values and areas are estimated at $< 1\%$. Data Table from SPIRE Observers Manual (ESA, 2011).

Band	Major$\times$ Minor FWHM	Geometric mean FWHM	Average beam area
(μm)	(arcsec)	(arcsec)	arcsec^2
250	18.3 $\times$ 17.0	17.6	423
350	24.7 $\times$ 23.2	23.9	751
500	37.0 $\times$ 33.4	35.2	1587

surface brightnesses from the data are calibrated for sources with slopes where νf_ν is constant. Colour corrections are used to adjust the surface brightnesses to more accurately match what is expected from sources with 15-25 K blackbody emission modified by λ^{-2} emissivities. All the data used are from the SPIRE Observers Manual. The equation for this conversion is (take 250μm as example):

$$1 \text{ Jy/beam} = 423 \text{ beam/arcsec}^2 *0.98279*0.994 \text{ Jy/arcsec}^2$$

where 0.98279 and 0.994 are colour corrections for the 250μm image. Then the unit of the image can be converted by multiplying by the above result.

After the foreground stars removed and units are converted, all the images are convolved to the same resolution.

3.3   Convolution

3.3.1   Mathematical Introduction of Convolution

Convolution is a mathematical operation on two functions, one of which is a created kernel function that acts on the original function and producing a third one. Basically, convolution performs a 'weighted average' of all the pixels in the original image neighbourhood specified. That is, it multiplies the value of each nearby pixel by the amount given in the kernel, then adds all those values together to produce the final result which is presented as the third function, the convolved image. For example if the kernel is a 3$\times$3 matrix K, and the original image is a n$\times$n matrix I, the convolved image C will be a matrix with the same dimensions as the original one, n$\times$n. n is a integer starting from 1. Any pixel value C_{nn} will be calculated as

the sum of the 3×3 matrix centred on this pixel from the original image, multiplied by the kernel. So the convolved image C will have the result value given by the following formula:

$$
\begin{aligned}
C_{nn} &= I_{(n-1)(n-1)} * A_{11} + I_{(n-1)n} * A_{12} + \\
&\quad I_{(n-1)(n+1)} * A_{13} + ... + I_{(n+1)(n+1)} * A_{33}
\end{aligned}
\tag{3.5}
$$

This formula will calculate the value of any pixel in the image, except the edge and corner ones. For example I_{11} or I_{12} or I_{n3}, need a value for I_{00} or $I_{(n+1)3}$. There are different calculation methods defined for the edge effect which will be discussed later.

3.3.2   The Point Spread Function and Beam Size

The resolution of a telescope is defined as following

$$
R = \frac{\lambda}{D},
$$

where λ is the wavelength of the observed radiation and D is the diameter of the telescope's objective. The resolution also represents the beam size. The concept of beam comes from a point source. The point spread function (PSF) is usually an Airy function peaking at the centre and surrounded by side lobes at the edge. The width of the function at the half maximum to the peak is called full width half maximum, or FWHM, which usually represents the resolution of the image. The FWHM is also called the beam size.

To prevent the beam effect influence during the comparison, it is necessary to match the beam size of the point spread functions (PSFs) at different wavelengths to the PSF of the longest wavelength that has the lowest resolution. In this analysis, I matched the beam size of all the images to the PSF of the 500μm data which has the lowest resolution.
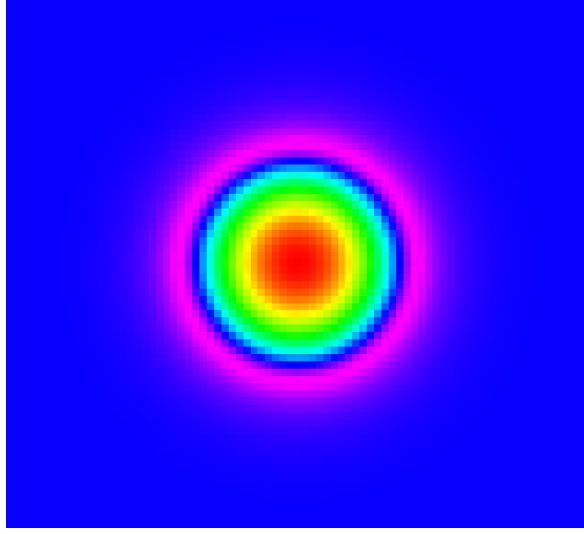
Figure 3.3: Gaussian kernel function used in convolution. The panel shows the function as an image.

The convolution operation acts as a function that smooths the original image and matches the resolution to the required one. It changes the shape of the PSF and makes it broader, with a lower peak so that the flux is conserved. I used this technique on galaxy image processing, treating the galaxy image as arrays of data, which is the original function, and using a Gaussian function as the kernel function. The kernel function has a smaller size than original array. It is an exponentially distributed data array peaked at the centre. We use a Gaussian as kernel function because the SPIRE images have small side lobes which are only 2% of the peak, so the point spread function (PSF) is very similar to the Gaussian shape. The kernel function used in this project has the form of

$$K(r) = \exp\left(\frac{-r^2}{2((\sigma_1/2.35)^2 - (\sigma_2/2.35)^2)}\right), \tag{3.6}$$

where σ_1 is the FWHM of the PSF of the longest wavelength image. In this project we use the FWHM of the PSF of the 500μm image so that all the images have the same resolution as the 500μm image. σ_2 is the FWHM of the PSF of the original image which is to be convolved. r is a variable for the radius of the array function (Bendo et al., 2012a). The Gaussian function has FWHM of 2.35σ. Fig.
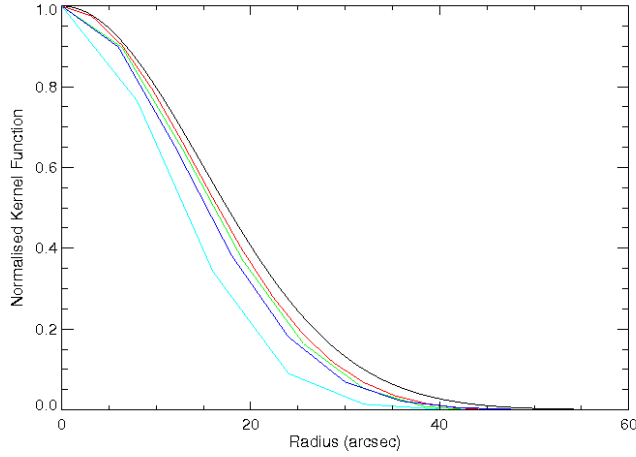
Figure 3.4: Gaussian kernel function as linear plots used in convolution. The functions are shown from the centre. X-axis is in arcsec. Totally there are 5 kernel functions plotted for all the different wavelength images being convolved to the $500\mu m$. From right to left are the kernel functions for Hα (black), $100\mu m$ (red), $160\mu m$ (green), $250\mu m$ (blue) and $350\mu m$ (yellow) respectively. The $1.6\mu m$ kernel function is the same as the the Hα one. Program to plot the right panel is in Appendix A.15.

3.3 shows this Gaussian kernel function in image and Fig. 3.4 shows this Gaussian kernel function in plots. We show all the kernel functions for convolving different wavelength. They are different because the value of σ_1 and σ_2 are different in different instrument images, and r is also different from different instrument images because the differen scales of pixels. The kernel functions are shown in linear scale from the centre of the kernel image. All the kernel functions are normalised to a peak of unity.

The beam of the SPIRE images ($250\mu m$, $350\mu m$ and $500\mu m$ images) are shown in Fig. 3.5. The beam sizes of SPIRE images are listed in Table. 3.1.

The PSFs of the PACS instrument have bigger sidelobes which peak at levels that are 10% of the central peak, so we used specialised convolution kernels to match the PACS PSFs to the $500\mu m$ PSF. The beam size of the PACS instrument is shown in Fig 3.6. The pixel scale of the $100\mu m$ image is 3.2 arcsec, and for the $160\mu m$ image is 6.4 arcsec (ESA, 2009).
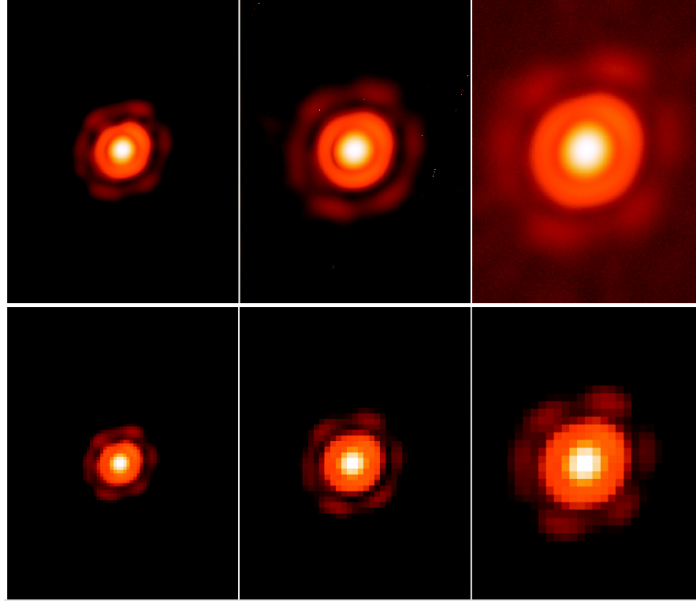
Figure 3.5: Log scale images for the empirical SPIRE beam model at 250, 350, and 500 μm from left to right respectively. The top row uses a 1 arcsec pixel scale for all maps, and the bottom row uses the nominal SPIRE map pixel scales of 6, 10, and 14 arcsec from left to right respectively. Image from Sibthorpe et al. (2011).

3.3.3 Using Convolve as a Command

Convolution is carried out as a command in IDL. It has several versions which act differently to the edge of the original image as an edge effect. Each version has a different way to define the value of I_0 and $I_{(n+1)}$. There are five versions of convolution and Fig. 3.7 shows all their effects. The Hα image of NGC4254 is being used here as an example. All the six images are in the same scale of zoom so we can see the edge of the image and compare the differences. The order of the images are (from left to right from first line) the original image, convolved with no parameter, and with parameter of EDGE_MIRROR, EDGE_TRUNCATE, EDGE_WRAP and EDGE_ZERO. In this order we call these panels 1 to 6.
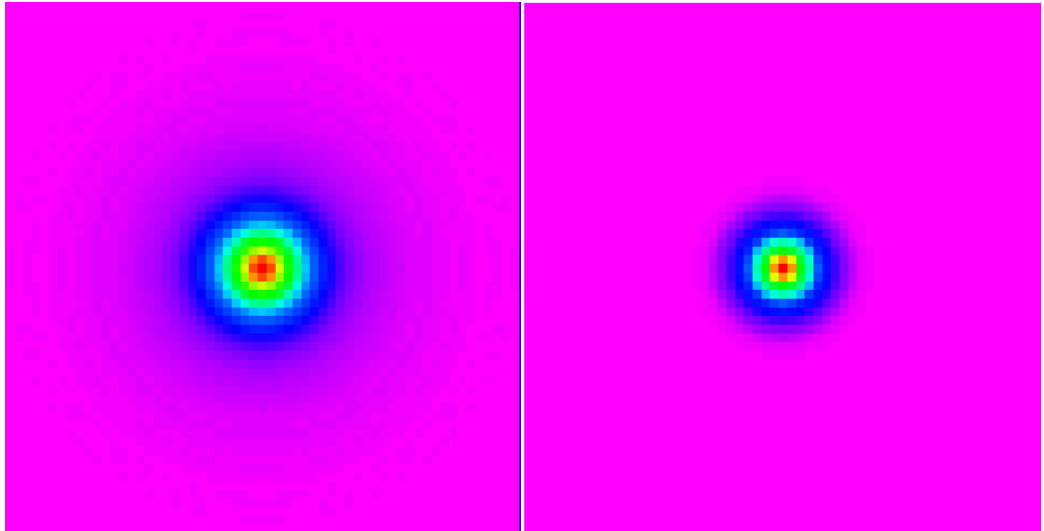
Figure 3.6: Log scale images for the empirical PACS beam model at 100 and 160 μm from left to right respectively.
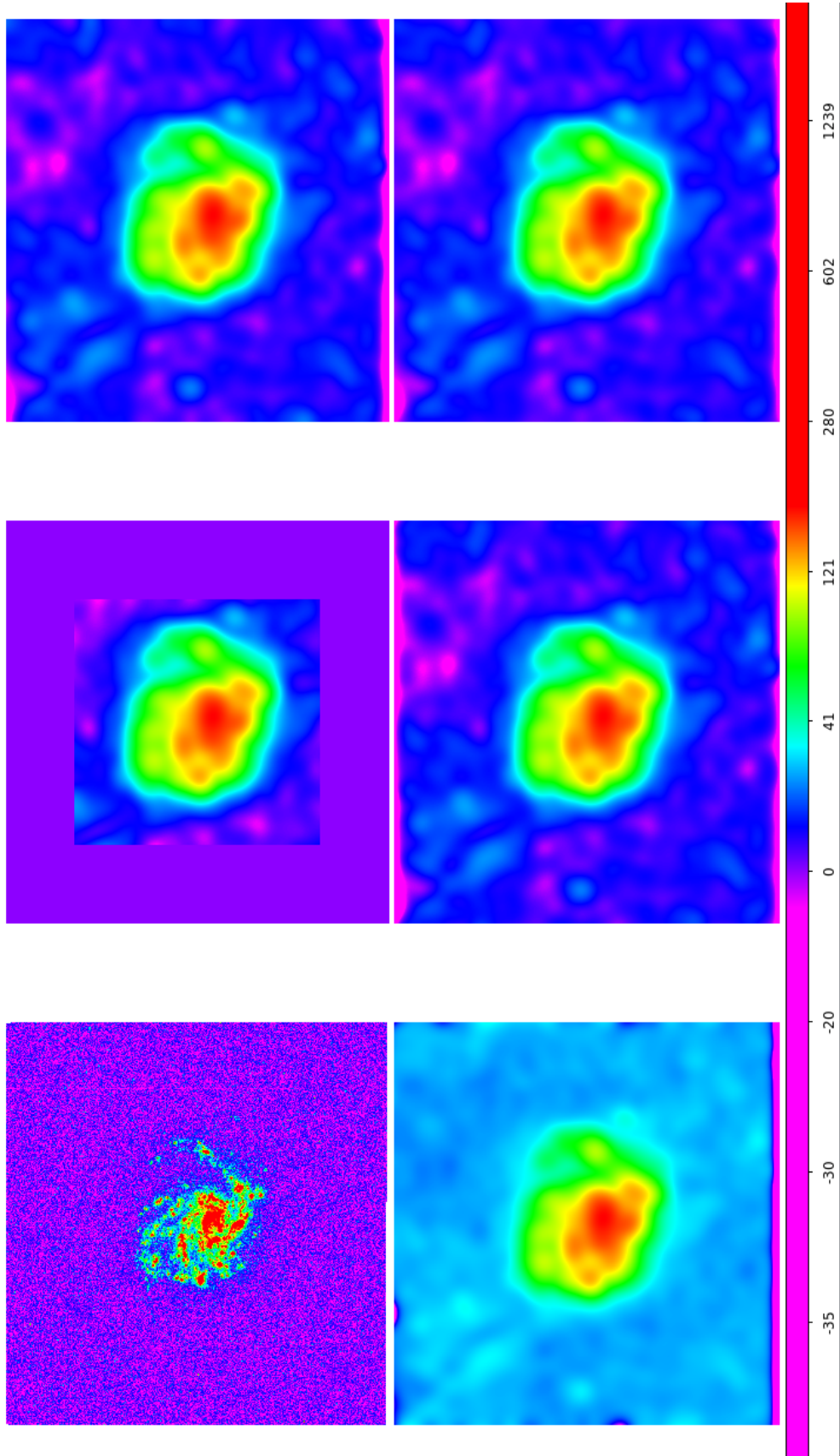
Figure 3.7: Hα image of NGC4254 as an example of how convolution with different edge effect works.

Panel 1 is the original image. There are bad data at the bottom edge on the image, which is not visible at this scale. Fig 3.8 shows an enlarged image of the bottom edge and the pink bad data line can be clearly seen compared to the blue background of the image.
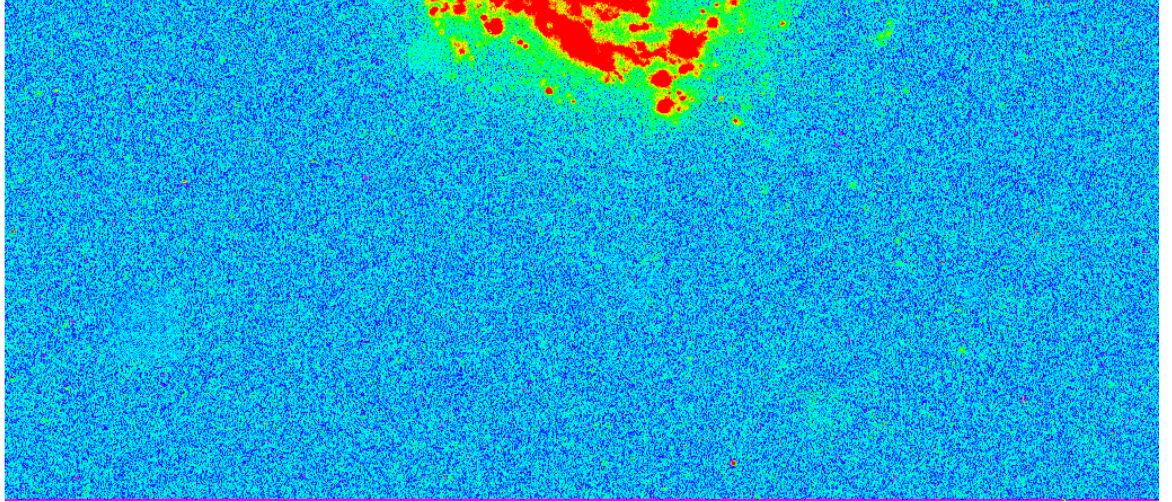
Figure 3.8: Hα image of NGC4254 enlarged 12 times to panel 1 in Fig 3.7 to show there is a pink bad data line at the bottom of the image.

Panel 2 is the convolution without any edge effect defined. We can see that the area in the image with usable data becomes much smaller. This is because the CONVOL sets the results to zero beyond the edge of the kernel. This removes the bottom bad data line.

Panel 3 is the convolution with keyword of EDGE_MIRROR, which computes the values of elements at the edge of array by 'mirroring' the subscripts of the array at the edge. This means it assigns the value of $I_{(n-1)n}$ to $I_{(n+1)n}$. Because $I_{(n-1)}$ contains bad data, and the bad data line is 'mirrored', it shows an enlarged pink bad data area at the bottom.

Panel 4 is the convolution with keyword of EDGE_TRUNCATE, It will compute the values of elements at the edge by repeating the subscripts of the array at the edge. This means it assign the value I_{11} to I_{00} and I_{nn} to $I_{(n+1)(n+1)}$, so the bad data is repeated for calculating the edge of the convolved image. We can see the bad data line is greatly enlarged by this way of calculation.

Panel 5 is the convolution with keyword of EDGE_WRAP. It will make CONVOL

compute the values of elements at the edge of array by 'wrapping' the subscripts of array at the edge. That means it gives the value of the bottom line to the line above the top line, which is the data in line I_n to I_0 and give the value of the top line I_1 to the $I(n+1)$ line. The results of this will obviously copy a bad data line from the bottom to the top for the calculation. The result of the 'wrapping' is shown in panel 5. It shows the bad data line at the top edge of the image as well as the bottom line.

Panel 6 is the convolution with keyword of EDGE_ZERO. This keyword will make CONVOL compute the values of elements at the edge of array as if the array were padded with zeroes. This means the line I_0 and $I_{(n+1)}$ are all given the value 0. Compared to all the other convolution image, the edge bad data line is least enlarged. This is what's needed for my data analysis, so I choose this keyword for my convolution in this project.

Another important keyword used is NAN in the convolution procedure. It sets the missing data to not a number (NAN) data points so that during calculation the missing data are ignored for neighbouring elements. In the result, missing elements are replaced by the convolution of all other valid points within the kernel.

3.3.4 Convolved Images for Herschel Data

Fig 3.9 shows the comparison before and after convolution. The image on the left is the original image, which is the 250 μm image of NGC4254. The right image is the convolved image. We can see that the convolution operation blurred the original image.

Fig. 3.10 shows the comparison of the PACS image of 100 μm of NGC4254 before and after convolution.

Convolution is carried out for all the images apart from the 500μm one as a step to match the resolution to the 500μm image.
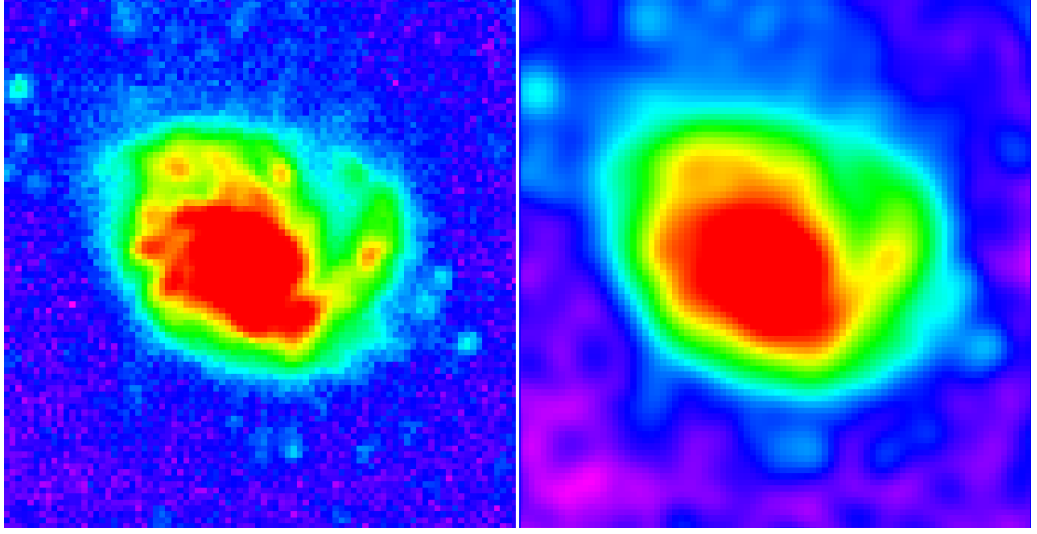
Figure 3.9: Comparison of SPIRE image (250μm) of NGC4254 before and after convolution.
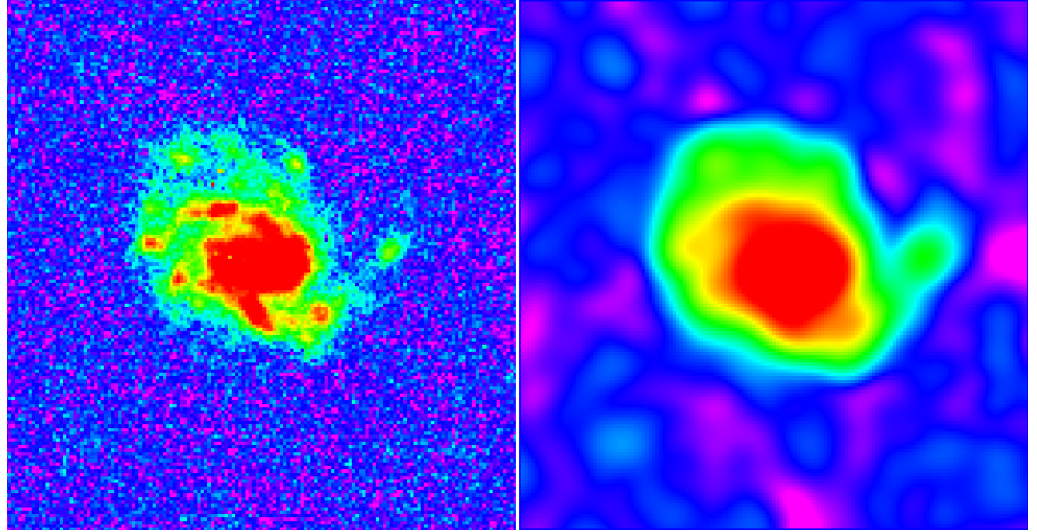
Figure 3.10: Comparison of PACS image (100μm) of NGC4254 before and after convolution.

3.4   Subtract the background

After the image had been prepared by the steps of removing foreground stars, changing units to Jy/arcsec^2, and convolving to the resolution of the 500μm image (which is defined as Photometer Long Wavelength(PLW)), we need to subtract the background.
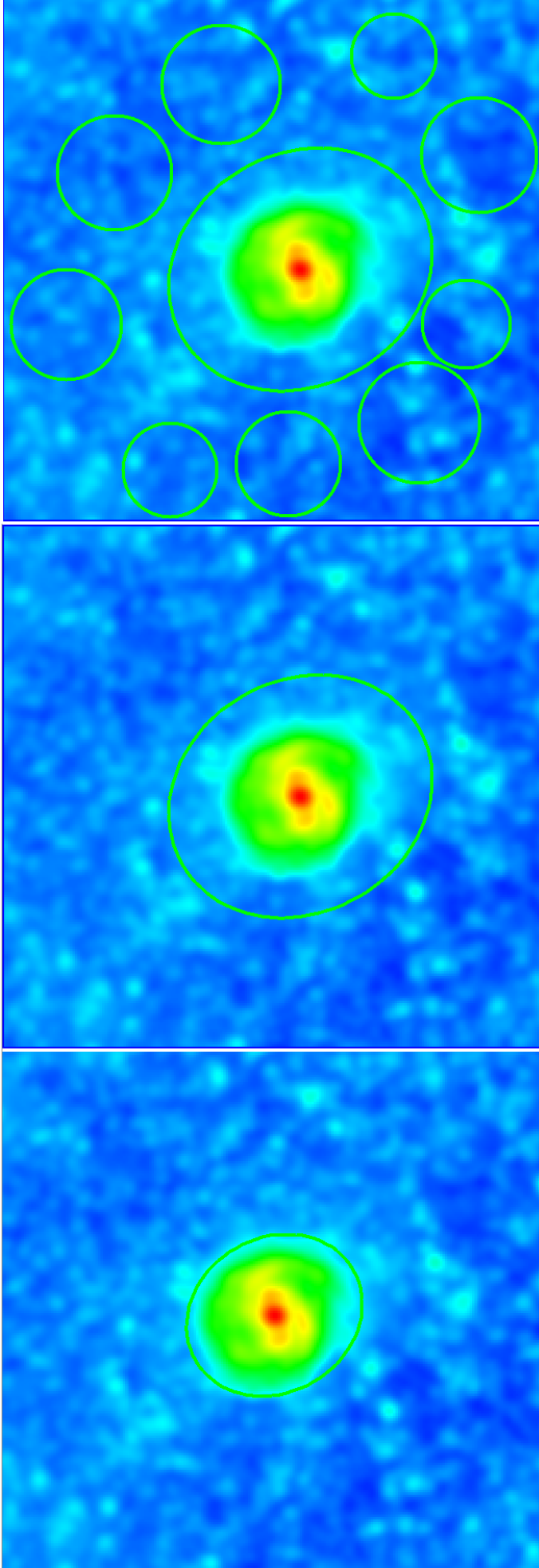
Figure 3.11: Figure shows how background regions are marked with $250mum$ image of NGC4321. The small circles outside the 1.5 optical disc are the marked background regions.

The background is identified by the following ways. I will take the 250μm image of NGC4321 as example. First, I located the optical disc (the optical disc is the elliptical isophote where the B-band surface brightness is 25.0 magnitude/arcsec^2) of NGC4321 on the image of the galaxy by using the load regions command in DS9. The optical disc of the galaxy Fig. 3.11 as a green ellipse surrounding the galaxy is shown on the left panel.

Second, we change the radius of the ellipse by multiplying the minor and major radius by 1.5. So for NGC4254, the minor radius is changed from 189 arcsec to 283.5 arcsec, and the major radius is changed from 222 arcsec to 333 arcsec. The location of the centre of the galaxy and the angle of the galaxy was not changed. The 1.5 times enlarged disc of NGC4321 is shown in the middle panel of Fig. 3.11

Third, outside the enlarged optical disc, which is assumed to be the background area, some background regions were chosen. The right panel of Fig. 3.11 shows the background regions in smaller circles outside the enlarged optical disc. These background regions are saved as region files for calculating the background and subtracting the background from the image.

In IDL, the background areas marked as circles in Fig. 3.11 is identified by using mask arrays where the background regions are marked as '1' and other areas are marked as '0'. The background noise is calculated as the 'MEDIAN' of the values of the background regions. Then the background noise is subtracted from the image.

3.5 The Size of the Extraction Box

We need to match the images of different sizes to the same size. The size of the extract box is calculated according to the the following formula:

Size of Extract Box = Major (or Minor) Radius $\times 2 \times (1.5/36) \times 36$

Explanation for the formula: First, get the value of the major and minor radius of the galaxy from loading the optical disc and then multiply it by 2 to make it the diameter of the galaxy, then multiply by 1.5 to make it the temporary full size of the image needed. Second, divide it by 36 and round it to an odd integer. Then

multiply it by 36 again to make the proper full size box. This step is make sure that the length of the side of the extract box can be divided exactly by 36 (This is explained in the rebin part). As the optical discs are ellipses, the above calculation needs to be done for both the major radius and the minor radius. Take the $250\mu m$ image of NGC4321 as example again, The size of the box in arcsec is

Length of Short Side $= 189 \times 2 \times 1.5/36 \times 36 = 540$

Length of Long Side $= 222 \times 2 \times 1.5/36 \times 36 = 684$
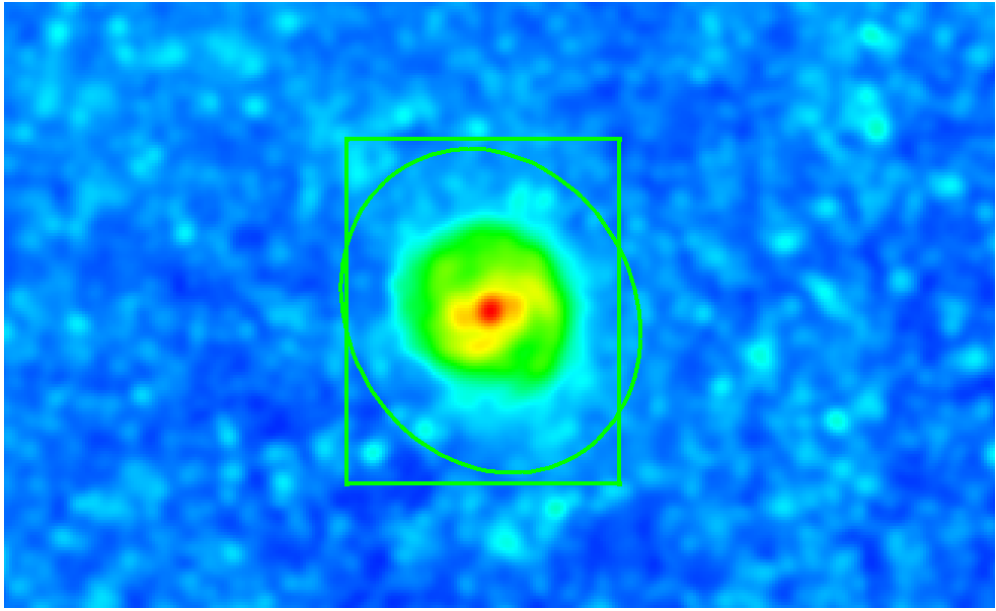
Figure 3.12: Comparison of extract box and the 1.5 optical disc of $250\mu m$ image of NGC4321.

Then, in DS9, through choosing the region shape of box and defining the box by the above values, we make a box centred at the galaxy. Fig. 3.12 shows the galaxy and the extract box. The 1.5 times optical disc is also shown to have a comparison of the two. We can see that they do not match perfectly. This is because the angle of the galaxy is not taken into consider in this extraction box size choosing. Data analysis is mainly from data inside the optical disc so the size of the extraction box doesn't influence the result when it is about 1.5 times of the optical disc of the galaxy. Also, the short side of the box is shorter than the 1.5 times optical disc and the long side of the box is longer than the 1.5 times optical disc. This is because when calculating the length of the short side, the result is 15.75 at the step after divided by 36. To round it to the nearest odd number, it has to shrink to 15 and

then multiply by 36, which made it shorter than the 1.5 optical disc. The long side had the result of 18.5 and the nearest odd number is 19 which made the final result bigger than the 1.5 optical disc.
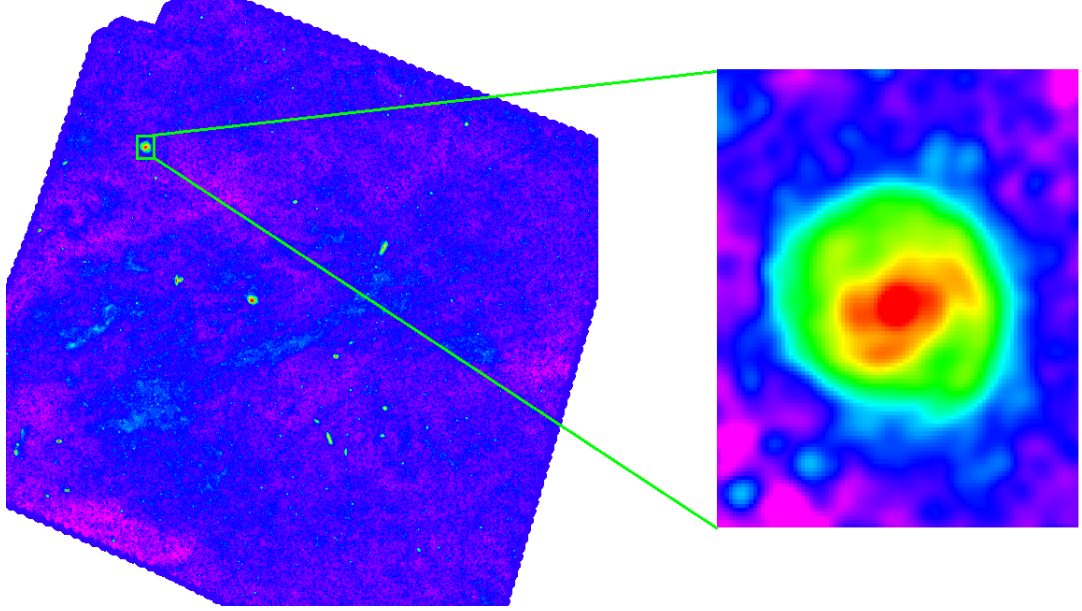
Figure 3.13: The original image of NGC4321 in Virgo cluster in 250μm on the left panel and the extracted image of NGC4321.

When the extract box is correctly loaded, the location of the box can be read by locating the cross hair at the bottom left corner and the top right corner to get the coordinates of the box as x_0, y_0 and x_1, y_1.

Finally, by using the IDL procedure 'HEXTRACT' together with the coordinates above, the box image can be 'cut' from the original image. Fig. 3.13 shows the original image and the extracted box of the galaxy. The left panel, shows the original 250μm image which contains many galaxies in the Virgo cluster, including NGC4321, which is at the left top corner with its extract box. The right panel shows the extract box which only contains the galaxy of NGC4321.

3.6 Coordinate Alignment

The extract box position is identified in the 250μm image. All the other extract boxes in the images of Hα, 1.6μm, 100μm, 160μm, 350μm and 500μm are taking the same extract box as the 250μm image by using the coordinate alignment command

'HASTROM' as a IDL procedure. The pixel coordinates of the other images are matched to the coordinates of the extract box of the 250 micron image.

'HASTROM' is a very powerful command to fix coordinate mis-alignment problem. It is used again as a good example in section 3.11 in this chapter.

3.7   Rebin

3.7.1   Define the bin size

Since all the images in this project have different wavelengths ranging from Hα to 500μm taken by different instruments, they have different resolutions and different pixel sizes. To compare the image and to make surface brightness ratios between difference wavelength images, we need the images to have the same resolution and pixel size. Convolution has fixed the problem of different resolution, and rebin can solve the problem of different pixel sizes.

To match the pixel size of all the images of different wavelengths to the same pixel size, usually the largest pixel size among the images will be defined as the bin size. The largest pixel size among all the images are the 500μm image which is 14 arcsec/pixel. But as we found in section 3.3.2, the FWHM of the PSF (beam size) of the 500μm image is 36 arcsec/beam which is about 2.5 times bigger than the pixel size. In this case we use the beam size as our bin size instead of the pixel size of the 500μm image. This is because if we use smaller bins, one beam will be separated into several pixels and the values of neighbourhood pixels of the same beam will not be independent to each other. This will cause fake correlation to the data analysis later, and so we can avoid having more pixels with the same PSF (Bendo et al., 2012a).

After choosing the bin size, all the different pixel sizes of different images are rebinned to this chosen bin size. This procedure is called rebin.

3.7.2 Rebin

Mathematically, the 'HREBIN' function in IDL re-sizes a vector or array to different dimensions given by the parameters. The supplied dimensions must be integral multiples or factors of the original dimensions. This function can expand an array or compress it. For example, an 20×30 array can be expanded into a 40×60 array or compressed into a 2×3 array.

In this project, we use the the beam size of 36 arcsec/pixel as our bin size. All the other images are compressed to the arrays of the 500μm image.

To match all the images from their original pixel size to 36 arcsec per pixel, we have made the length of the extract box as an integer times 36 so that we can get integer number of pixels for the extract box (refer to section 3.12). Taking the 250μm image of NGC4321 as example again, the size of the box in number of pixels are

$Length of Short Side = 540/36 = 15$

$Length of Long Side = 684/36 = 19$

That means the images in different wavelengths of NGC4321 are all made into the same image size of 540×684 arcsec^2 which is in $15 \times 19 = 285$ pixels. Fig. 3.14 shows the comparison of the original, convolved and rebinned image of NGC4254 in 250μm.

To realise this I used IDL and the command 'HREBIN' with the size of its extract box in pixels as parameter.

All the galaxies images in this project are prepared and rebinned using the above technique.
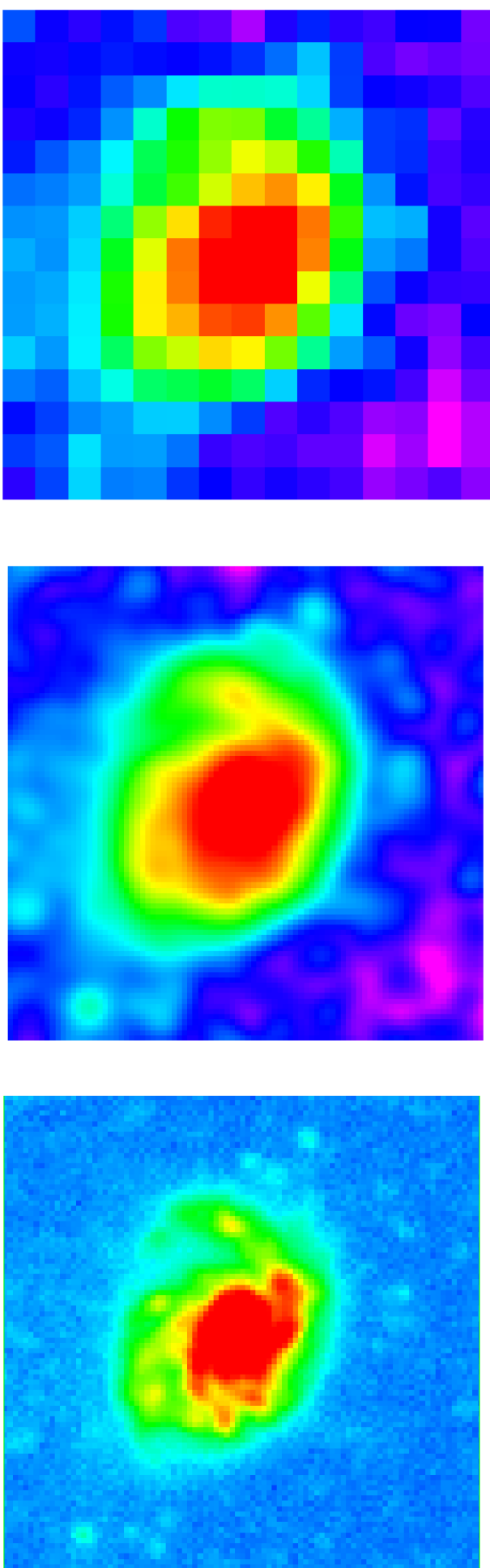
Figure 3.14: The comparison of image NGC4254 in 250μm. Left panel is the original image, the middle panel is the convolved image, the right panel is the convolved and rebinned into $15 \times 15 = 225$ pixels image.

3.8 Data Selection

After the data is prepared, we selected the data for analysis.

Though the median of the background has been subtracted, the image still contains a background noise. The background noise is measured by the standard deviation of the value of the pixels of the background area. The background area is normally located at the four corners of the cropped galaxy image. "Normally" here means if there is no abnormal bright spot of un-background like object, otherwise, we will ignore that corner or move to another more normal background area on the edge near that corner. 9 pixels were chosen for each corner, so we have 36 pixels for standard deviation of background noise calculation for most of our galaxies. For some galaxy image we had less than 36 pixels for the standard deviation calculation because of abnormal bright flocculent object in the background area. The standard deviation is defined as σ and only pixel with image values higher than 5σ in all the wavelength bands were chosen for analysis, except for the 500μm one. The reason for the exception of the 500μm one is because the data points would be very limited if we include the 5σ level for 500μm image, as it has low signal to noise (S/N).

The IDL Program doing the data preparation and data selection is attached in Appendix A.2.

3.9 Colour Temperature Map

After the data selection (without rebinning in 36 arcsec) I made the 100/160, 160/250, 250/350 and 350/500 μm ratio maps. Based on these ratio maps, I converted them (the calculation uses $\beta = 2$)into colour temperature maps so the colours shown on the map represents temperatures. I also made the legend for the colour temperature maps using the following method.

The histogram on the top of the left panel of Fig. 3.15 shows the pixel distribution with temperature from the lowest of 9.5 K (marked by the red line) to the highest of 28.6 K. The colour bar at the bottom of the panel shows the temperature legend with colour for the map. We can see that there are not many data points
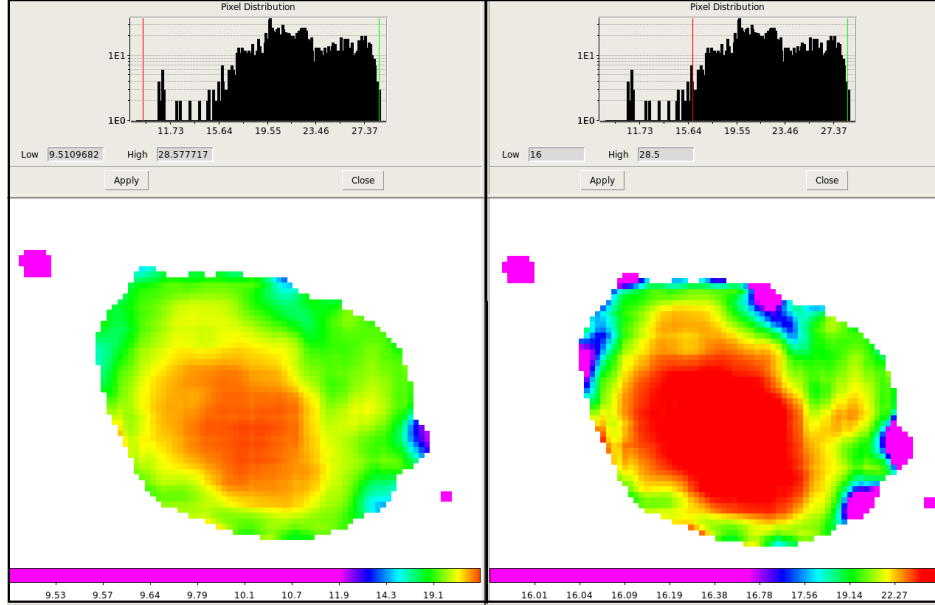
Figure 3.15: Temperature margin choosing with colour temperature map of 250/350 μm of NGC4254. The left panel shows the pixel distribution with temperature before margin choosing, the right panel shows the pixel distribution with temperature after margin choosing.

under 16 K from the pixel distribution. So we only choose the pixel distribution for temperature bwtween 16 K as the lowest temperature (see the red line in the pixel distribution on the right panel) and 28.5 K as the highest temperature (see the green line in the pixel distribution on the right panel). This shows more detail in the cooler region. The cold dots shown out side the galaxy disc may be background galaxies. They show up in these maps but not the shorter wavelength maps because the SPIRE instrument is more sensitive than PACS instrument.

3.10 Remove Bad Data Point

After the data selection I made the ratio plot for data analysis. In the original plots that I made, sometimes there were data points (usually one or two) which were away from most of the other data points. For example, shown in the left panel of Fig. 3.16, there is a data point on the left top of the all the other data points which seems a bad data point because it is not with all the other data. The plot is the surface brightness ratio of 350μm/500μm against 1.6μm. We used the following technique to remove this bad data point.
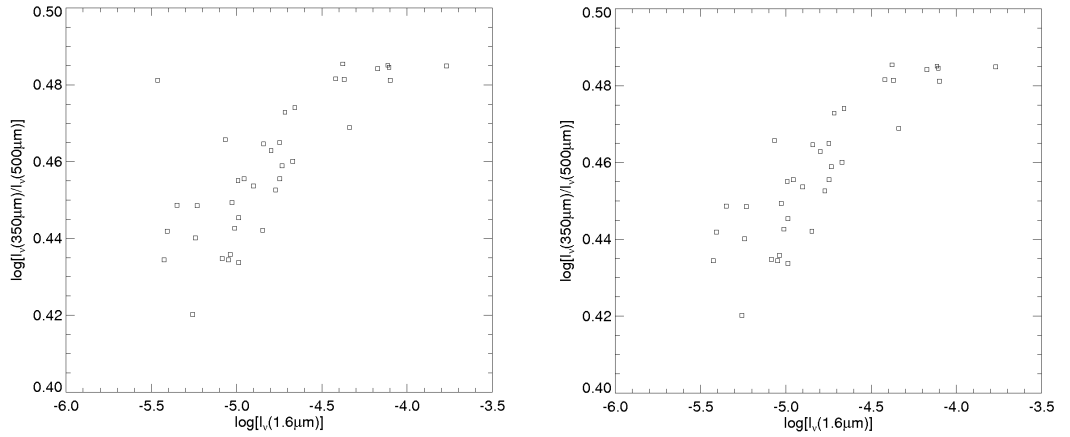
Figure 3.16: The ratio plot of 350μm/500μm against 1.6μm of NGC4254 as an example of comparison of before bad data being removed and after. The ratio is in logarithm. Program for this ratio plot is in Appendix A.17.

From the plot, this point is the only data point to have a value greater than 4.8 in 350μm/500μm and less than -5.4 in 1.6μm. So through checking the location of the data point greater than 4.8 in the data array of ratio of 350μm/500μm using the IDL command 'WHERE', the locations of all the data greater than 4.8 can be found. Using that location we can find the image position of the data on the rebinned ratio map. Since there are a few data points greater than 4.8, I checked the position of the data points less than -5.4 in the data array of 1.6μm as well.

The location of the pixel in both groups is pixel (4,6). Fig.3.17 shows the location of this data point by a green circle. We can see that in all maps, the centre of the galaxy is represented by a hot red colour and the cooler edge is with yellow, green and other colours. In the ratio image this pixel is an abnormal hot red point at the lower left edge of the galaxy and all the other three maps show it as a cool point outside the hot centre. Through checking the value of this pixel at the 500μm image we find it is extra low. So we assume this is the reason for the extra high ratio of 350μm/500μm at this point. The reason for this might be because the 500μm image have a low resolution and when it was rebinned, the background noise might be rebinned into this pixel and made this pixel an extra low value. After we subtract this pixel from the data group, The abnormal top left data point in Fig.3.16 disappeared.

We use the same technique to find bad data points in all images. We use IDL to
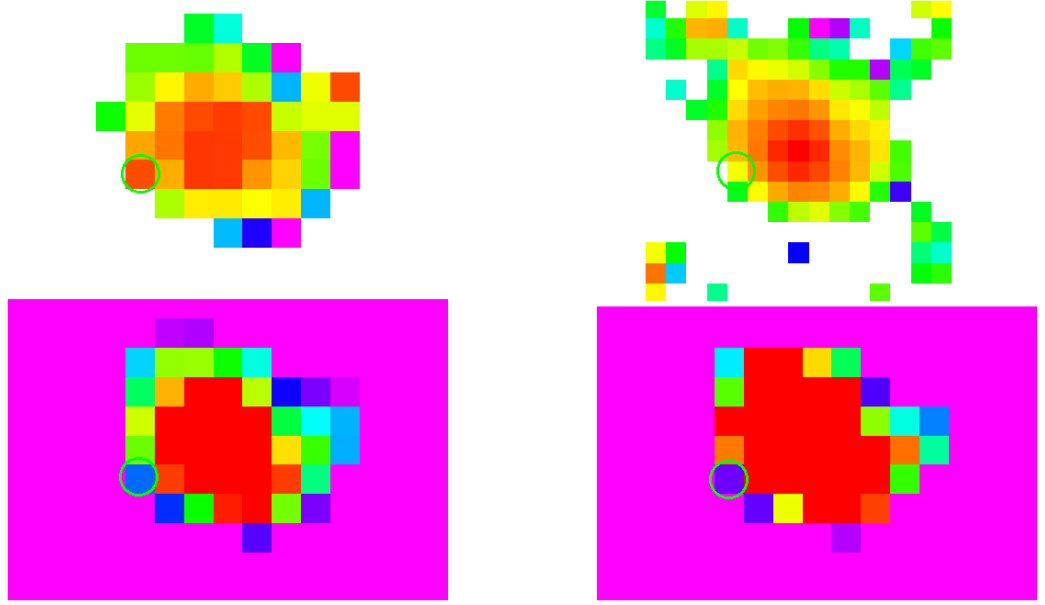
Figure 3.17: The bad data's location in the ratio map of 350μm/500μm (top left) and comparison of the location in 1.6μm(top right), 350μm(bottom left) and 500μm(bottom right). The ratio map and the 1.6μm map is made in logarithm so the value shown is the same with the value in the ratio plot figure. Program for the ratio map is in Appendix A.16.

define these points as not a number (NAN) which remove the bad data pixel. The

right panel of Fig.3.16 shows the final version of the plot without bad data points.

3.11   The Problem of the NGC4321 160μm Image
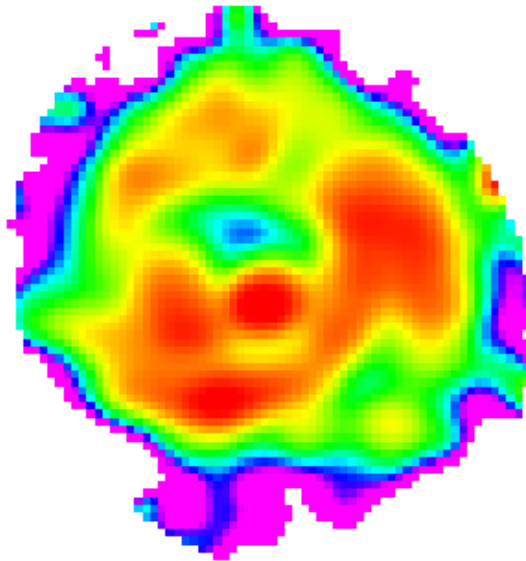
Figure 3.18: The surface brightness ratio of 160/250 μmof NGC4321.

After all the data are prepared, I did the surface brightness ratio images for analysis. The ratio image of NGC4321 160/250 μm shown as Fig. 3.18 seems not the same as the other ratio images. Also, the correlation with the Hαimage is 0.39 and with 1.6μmis as low as 0.19 while all other ratios are mostly more than 70%. In Fig.3.18, there is an unusual cold blue area inside the spiral arms just right above the hot red core of the galaxy. Normally there shouldn't be such a cold area inside the spiral arm area close to the core because of stellar population distribution consistancy. According to empirical experience, we guess this unexpected cold area might be created by misalignment of the two images. So we checked and did find a small misaliagnement as shown in Fig. 3.19.
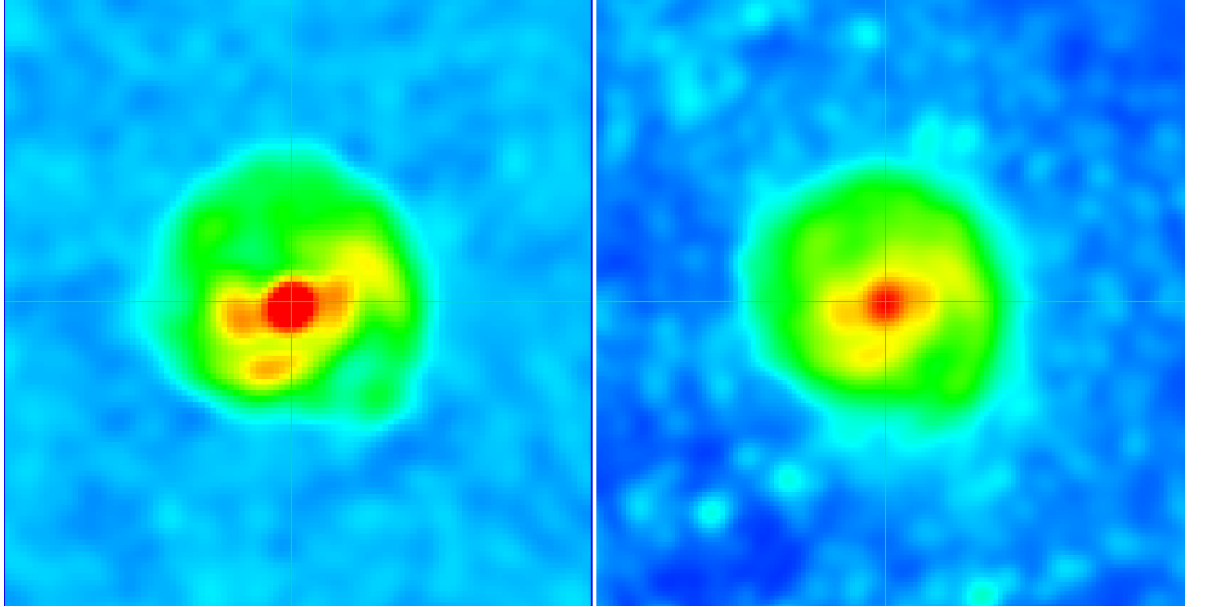
Figure 3.19: The 160μm image (left) and the 250μm image (right) of NGC4321. The cross hair is located at the centre of the 250μm image (right) and the coordinate of the two images are locked.

The coordination's of the two images are locked at the centre of the 250μm image, but the 160μm image on the left panel shows the centre are a little up shifted from the centre.

To solve this problem, a program (see Appendix A.11) is made to change the coordination of the 160μm image to match the coordinate of the 250μm image. The keyword to change the coordinate used is 'SXADDPAR'. The y axis is defined in the header information by CRPIX2. The original value of CRPIX2 is 1640.5.

Table 3.2: Comparison of value of the same pixel of different wavelength (μm) images.

location	160	250	100	70
location 1	0.004	0.247	0.003	4.19
location 2	0.075	0.364	0.012	11.57
ratio	1:19	1:1.5	1:4	1:3

Changing the value of CRPIX2 can adjust the coordinate value of the y axis. By trying a range of numbers from 1650.5 to 1630.5, the best coordinate found was 1639.9 which shifts the coordinate of the 160 μm image to the centre as shown in Fig. 3.20. The coordinate is shifted by 0.6 pixels.
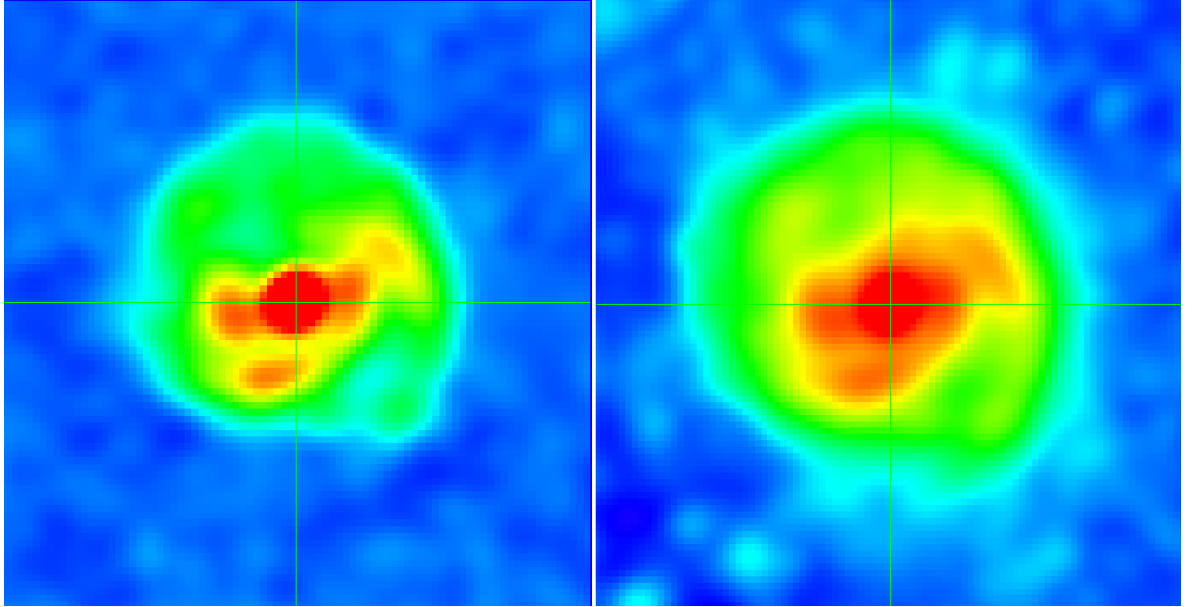
Figure 3.20: The 160μm image (left) and the 250μm image (right) of NGC4321 after the adjust of coordination of the 160 μm image. The cross hair is located at the centre of the 250μm image (right) and the coordinate of the two images are locked.

A new ratio image of 160/250 μm is made and shown in Fig. 3.21 using the new image of the 160μmİt shows a less noisy edge of the galaxy than Fig. 3.19 but the odd cold blue point is still there.

This means the problem may not be caused by the coordinates but may come from the 160μm image itself. Fig. 3.22 shows a detailed comparison of the 160μm image to the other wavelength images.

From Fig. 3.22 we can see that the 160μm has a cold blue area that is very close to the core of the galaxy which is not shown in any other wavelength though they
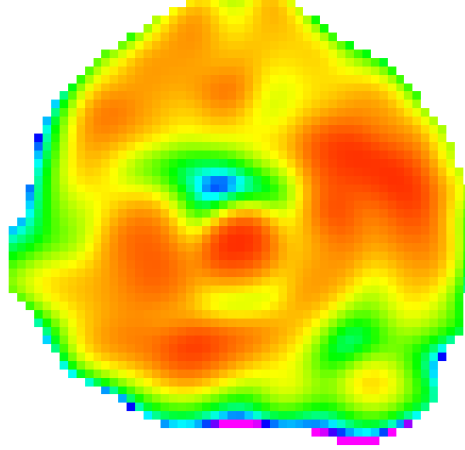
Figure 3.21: The 160/250 μm surface brightness ratio image after the adjustment of the coordination of the 160 μm image.
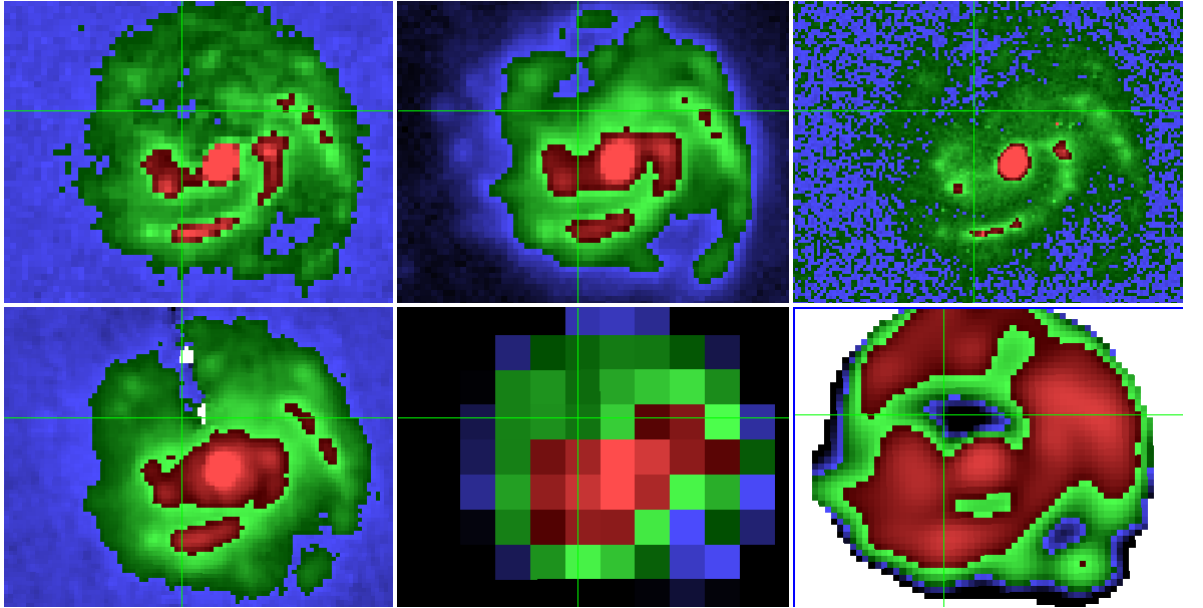
Figure 3.22: The comparison of the 160μm image to other wavelength images of NGC4321. From left top to right bottom the images are: 160μm before coordinate correction, 250μm, 100μm, 70μm, the rebinned 160μm and the ratio of 160/250 after coordination correction. The colour scheme used in DS9 is standard. This scheme shows the temperature from cold to hot in the colour of black, blue, dark green, green, dark red and red. This colour scheme is used because the green cross hair is better shown.

have a cold area at the left top area as well. On the left top there is a bright green area which is shown at the same location in every wavelength image. Locating the cross hair at the blue area (location 1) of 160μm as shown in Fig. 3.22, it shows the

value of that area. Comparing this value to the value shown at the bright green area (location 2) at the left top, we can get a ratio of the value of location 1 compare to location 2. Investigating the other wavelength images in the same way, the results are shown in Table. 3.2.

From the ratio results from Table. 3.2, we can see that the ratio is too large in the 160μm image which means the data there might be wrong. The 160μm image are from PACS instrument which have a different way to subtract the background and there might be a wrong subtraction in the image.

Knowing this, the solution can be subtracting this area by taking off these pixels. The ratio image on the right bottom of Fig. 3.22 shows the black dark area which are supposed to be the wrong value area and the same location is shown in the rebinned image of 160μm. We find the locations are in pixel (7,11) and (8,11). Since in IDL the counting way is different, we use (6,10) and (7,10) for programing.

After subtracting the wrong pixel area, the correlation with Hα become 0.61 and with 1.6μm become 0.45 as calculated which greatly changed from the bad result of 0.39 0.19. I tried to add the coordination modify to the program as well to improve the result, but the correlation with Hα become 0.0.58 and with 1.6μm become 0.48 which is a very small change (3%). So we decide not to make the coordination modification to the 160μm image of NGC4321.

Chapter 4

Data Analysis

4.1 Theory Background

4.1.1 Blackbody Emission

The blackbody emission is described by the Planck function. In terms of frequency ν it is given by:

$$B_\nu = \frac{2h\nu^3}{c^2} \frac{1}{\exp(h\nu/k_B T) - 1},$$ (4.1)

and in terms of wavelength λ:

$$B_\lambda(T) = \frac{2hc^2}{\lambda^5} \frac{1}{\exp(hc/\lambda k_B T) - 1},$$ (4.2)

where B is the surface brightness or specific intensity of the radiation, ν is the frequency, λ is the wavelength, h is the Planck constant, c is the speed of light, k_B is the Boltzmann constant and T is the temperature. The unit of the surface brightness in frequency is W m^{-2} Hz^{-1} sr^{-1}, and in wavelength it is W m^{-2} μm^{-1} sr^{-1}.

We first assume that dust emits as a blackbody, so that the intensity of the dust emission of each dust grain is $I_\nu = B_\nu$.

Fig. 4.1 shows the logarithm of the specific intensity of the dust emission B_λ (Eq. 4.2) versus wavelength λ, as function of the temperature T of the dust. The
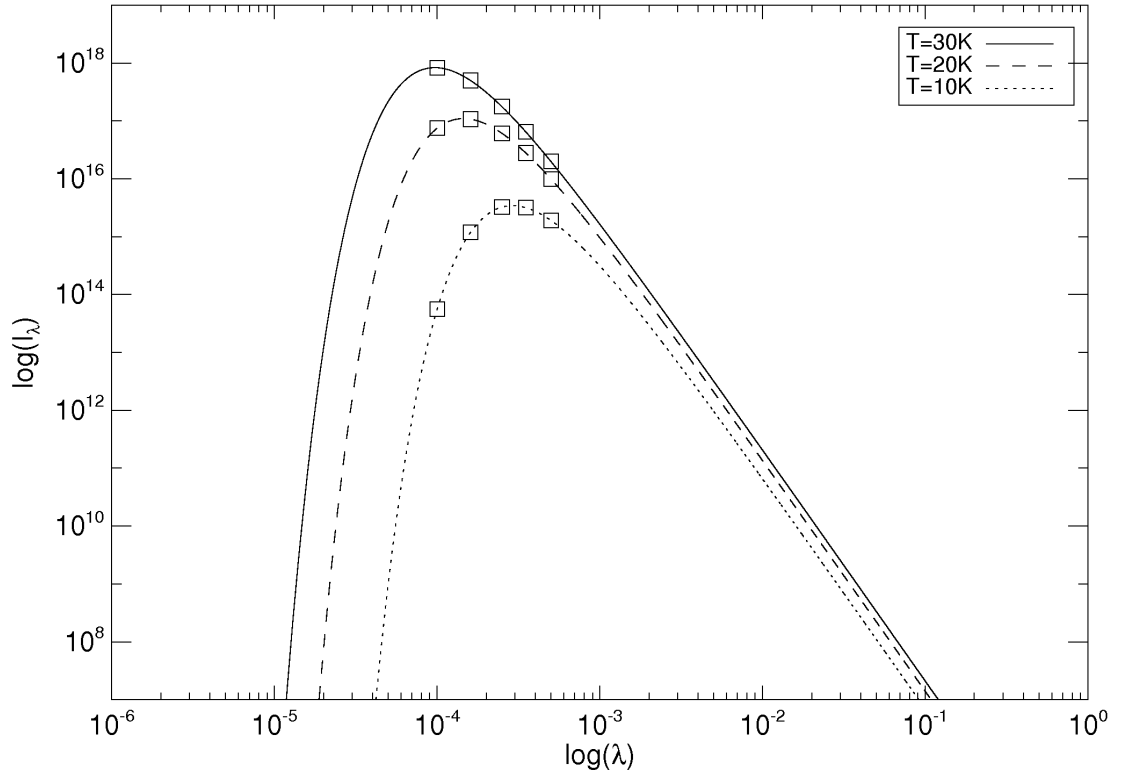
Figure 4.1: Plot of the logarithm of the blackbody function (assuming dust emission as blackbody). The unit of $\log I_\lambda$ is arbitrary. The unit of $\log(\lambda)$ is log(meter). The five square points on each curve are at wavelengths of 100μm, 160μm, 250μm, 350μm and 500μm respectively. This plot is made in IDL see Appendix A.3.

dotted curve is the intensity for a temperature of 10 K, the dashed curve for 20 K and the solid line for 30 K. From the plot we can see that

1. At any λ, the hotter dust emits the highest intensity.

2. The shorter λ's are not sensitive to cold dust. Roughly, dust has negligible emission at about $\lambda \leq 0.2\lambda_{peak}$. In other words, colder dust only shows detectable emission at longer wavelengths. We can see that the peak for 30 K is at about 100μm, and the emission is negligible below 20μm. At 10 K, the peak is at about 300μm, and the emission effectively ceases at 60μm.

3. At $\lambda \gg \lambda_{peak}$, all temperatures give the same slope. This part of the plot is also called the Rayleigh-Jeans tail where the gradient becomes constant.

A blackbody emission is defined per surface area, and the plot in Fig. 4.1 assumes the same surface area at each temperature. In terms of dust emission, the equivalent

assumption is that the dust mass (or more precise, grain surface area times number of grains) is the same at each temperature.

There are five data points chosen on each curve which are from left to right at 100μm, 160μm, 250μm, 350μm and 500μm respectively. We choose these wavelengths because the galaxy images for analysis are taken at these wavelengths. These wavelengths correspond to blackbody temperatures of 30 K to 6 K.

Comparing the intensities at the same wavelength but at different temperatures, we can see from Fig. 4.1 that the ratio of $I_{\lambda,T=20K}/I_{\lambda,T=10K}$ is always larger than the ratio from the higher temperature pair (30K, 20K). This relation holds true over all wavelengths. The ratio difference is larger at shorter wavelengths. At longer wavelengths, at the Rayleigh-Jeans tail, it becomes a constant. The constant ratio at the Rayleigh-Jeans tail can also be proved by the following equation:

At longer wavelength, $\frac{hc}{\lambda k_B T} \ll 1$, so

$$\exp \frac{hc}{\lambda k_B T} - 1 \simeq \frac{hc}{\lambda k_B T}$$

Hence the ratio is

$$\frac{I_{\lambda,T_1}}{I_{\lambda,T_2}} = \left(\frac{2hc^2/\lambda^5}{2hc^2/\lambda^5} \right) \left(\frac{1/\exp(hc/\lambda k_B T_1) - 1}{1/\exp(hc/\lambda k_B T_2) - 1} \right) = \frac{T_1}{T_2}, \qquad (4.3)$$

which is a constant independent of wavelength.

The intensity ratio between different wavelengths also shows a trend. At higher temperature, the ratio between different wavelengths $I_{\lambda_1}/I_{\lambda_2}$ ($\lambda_2 > \lambda_1$) is always smaller than the corresponding value at lower temperature. For example, the gradient of $I_{100\mu m}/I_{160\mu m}$ at 30 K is negative, but at 10 K and 20 K it is still positive. Even the gradient of $I_{350\mu m}/I_{500\mu m}$ at 30 K is steeper than the 20 K one and the 20 K one is much steeper than the 10 K one. This trend is studied in detail in later sections.

At longer wavelengths within is the Rayleigh-Jeans tail part, for a certain temperature T, the ratio become

$$\frac{I_{\lambda_1,T}}{I_{\lambda_2,T}} = \left(\frac{2hc^2/\lambda_1^5}{2hc^2/\lambda_2^5}\right)\frac{1/(\exp hc/\lambda_1 k_B T - 1)}{1/(\exp hc/\lambda_2 k_B T - 1)} = \left(\frac{\lambda_2}{\lambda_1}\right)^4 \tag{4.4}$$

which is independent of temperature.

4.1.2   Absorption Opacity κ of Dust Emission

Only ideally in strict thermodynamic equilibrium, does dust emit exactly like a blackbody, $I_\nu = B_\nu$. In the real universe, the dust clouds can be affected by optical depth effect which can adjust the blackbody emission.

The absorption opacity is described by the total interaction cross section between dust and the radiation. This include the absorption and the scattering cross sections. So the absorption opacity can be described as

$$\kappa \propto C_{abs} + C_{sca} \tag{4.5}$$

In the long wavelength limit, The cross sections are (Draine, 2011)

$$C_{abs} \propto \lambda^{-2}$$

$$C_{sca} \propto \lambda^{-4}$$

So

$$\kappa = \kappa_0 \lambda^{-\beta} \propto \lambda^{-2} + \lambda^{-4} \tag{4.6}$$

where β is defined as the dust emissivity coefficient that indicates how the emissivity scales as a function of wavelength. The range of β is $\beta = 1 \sim 2$ (Draine, 2011).

In dust radiative transfer, κ is often approximated as
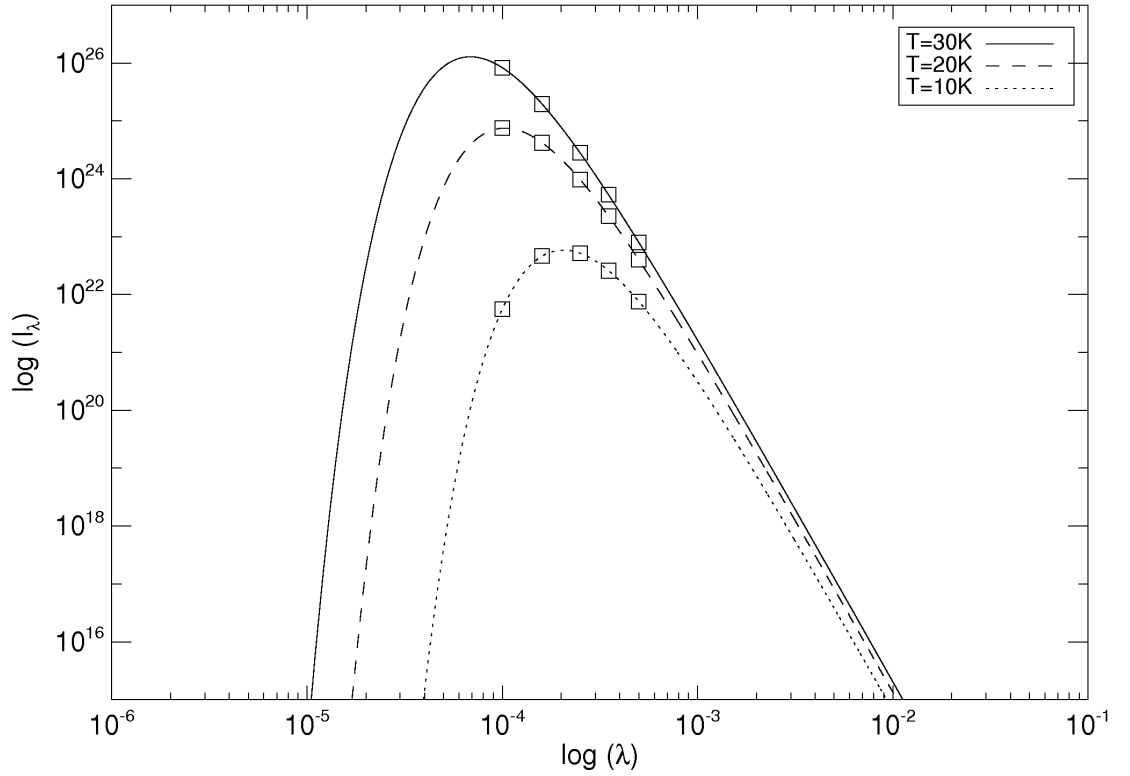
Figure 4.2: Plot of the logarithm of equation 4.8 against λ. The five square points on each curve is at wavelength of 100μm, 160μm, 250μm, 350μm and 500μm respectively. This plot is made in IDL. See Appendix A.7.

$$\kappa = C\nu^{\beta} = C'\lambda^{-\beta} \tag{4.7}$$

So the intensity I_{ν} can be written as (taking $\beta = 2$)

$$I_{\nu} = \kappa B_{\nu} = C\nu^2 B_{\nu} = C'\lambda^{-2}B_{\nu} \tag{4.8}$$

The new relation of dust intensity described by equation (4.8) is shown in Fig. 4.2. The unit of $\log(I_{\lambda})$ is arbitrary, the unit of $\log(\lambda)$ is $\log(\text{meter})$. Comparing Fig. 4.2 to Fig. 4.1, we find they share all of the properties described in the last section. But the peak of the intensity has moved to shorter wavelengths for all temperatures. The 100μm data point of the 30 K curve is located around the peak in Fig. 4.1, but falls after the peak in Fig. 4.2.

If we assume that the photons travel in straight lines, the change of a beam of specific intensity I_{ν} along a distance ds taken along a light ray is

$$\frac{dI_\nu}{ds} = -\kappa_\nu I_\nu + j_\nu \tag{4.9}$$

The first part on the right hand side of the equation is the absorption and the second part is the emission (Spitzer, 1978). The emission part is also related with the absorption opacity κ_ν. The optical depth τ and κ_ν have the following relation

$$d\tau_\nu = -\kappa_\nu ds \tag{4.10}$$

This lead to a proportional relation between τ and κ_ν which we can write

$$\tau_\nu = C\kappa_\nu \tag{4.11}$$

where C is a constant.

By using the solution to the equation of radiative transfer, the surface brightness or specific intensity I_ν of dust emission is

$$I_\nu = B_\nu(1 - e^{-\tau_\nu})$$

where τ is the optical depth and B_ν is the blackbody emission in the form of frequency given by the Plank function. For very large τ, $I_\nu = B_\nu$, giving a purely blackbody emission.

For small τ which is the optically thin case, $I_\nu = \tau_\nu B_\nu$, where τ_ν can be described as

$$\tau_\nu = \tau_0 \nu^\beta \tag{4.12}$$

or, in the form of wavelength

$$\tau_\lambda = \tau_0 \lambda^{-\beta} \tag{4.13}$$

which is the same form with Equation (4.7) and (4.11). We will use Equation 4.7 in later research and in this project, our research are based on long wavelength dust emission where absorption dominates over scattering (eq.(4.10)), So we take $\beta = 2$ Li & Draine (2001)) for all the calculations in this project.

4.1.3 The Complexity When Dust Mass is Involved

The surface brightness I_λ of the dust emission in the far infrared is not only influenced by wavelength and temperature. The amount of dust is another key influence to the surface brightness I_λ. A large dust mass will create a higher specific intensity. The relation between the flux density and mass of dust is

$$F_\nu = \frac{\kappa_\nu B_\nu(T) M_{Dust}}{D^2} \tag{4.14}$$

(Bendo et al., 2010b). F_ν is the flux density of observed dust, κ_ν represents the absorption opacity of the dust, $B_\nu(T)$ is the blackbody function for the best-fitting temperature (T) and M_{Dust} is the dust mass. κ_ν can be expressed as $\kappa_\lambda = C\lambda^{-2}$ as described in the previous section.

Equation (4.14) is shown in Fig. 4.3. The solid line is for a temperature of 30 K and the dashed line is for a temperature of 20 K, where both have the same amount of mass of dust. The dotted line is also at 20 K in temperature but has six times more dust mass. Part of this curve has a higher intensity than the 30 K curve. This significant change in dust emission makes it harder to tell what is the physical condition of the dust emission. The cross of the 30 K curve and the 20 K curve shows the same data point may contain completely different information.

Because we want to describe both the temperature and the dust mass for the SED, the confusing situation that the curves of Fig. 4.3 shows made the data analysis of dust emission only by intensity not reliable.

Hence, we use ratio plots to solve this problem. For one dust component observed at a certain wavelength with temperature 1 at dust mass 1 and temperature 2 at dust mass 2, the ratio of the flux density at two different observed wavelengths is:
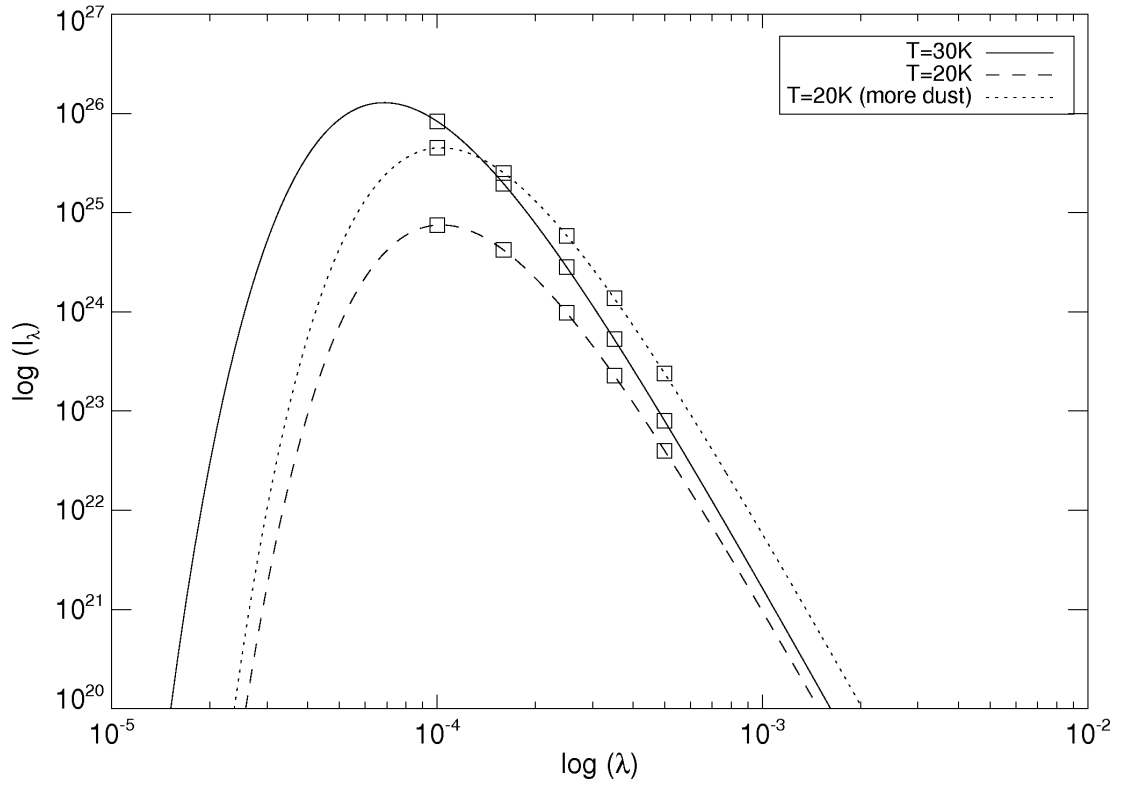
Figure 4.3: Plot of the logarithm of the surface brightness of dust emission I_λ against its wavelength λ. The unit of $\log I_\lambda$ is arbitrary and the unit of $\log\lambda$ is $\log(\text{meter})$. The five square points on each curve is at wavelength of 100μm, 160μm, 250μm, 350μm and 500μm respectively. This plot is made in IDL see Appendix A.4.

$$\frac{F_{\lambda_1}}{F_{\lambda_2}} = \left(\frac{C\lambda_1^2}{C\lambda_2^2}\right) \frac{B_{\lambda_1}(T_1)M_{Dust1} + B_{\lambda_1}(T_2)M_{Dust2}}{B_{\lambda_2}(T_1)M_{Dust1} + B_{\lambda_2}(T_2)M_{Dust2}} = \left(\frac{\lambda_1}{\lambda_2}\right)^{-2} \frac{B_{\lambda_1}(T_{av})}{B_{\lambda_2}(T_{av})} \qquad (4.15)$$

where T_{av} is a weighted average temperature. So the ratio equation solve the problem that mass bring and leave it a temperature related only equation which make things much easier to analyse. The temperature derived here also depends on the value of β taken. If we use a range of value of β from $\beta = 1.5$ to $\beta = 2$, the temperatures derived will also have a range of values for the same flux ratio.

4.1.4 Surface Brightness Ratio and Temperature

We may assume the observed dust is optically thin in the far infrared. If we observe at two different wavelengths λ_1 and λ_2, which originate from a single component

with a single temperature T, the surface brightness ratio $I_{\lambda_1}/I_{\lambda_2}$ is:

$$\frac{I_{\lambda_1}}{I_{\lambda_2}} = \left(\frac{\lambda_2}{\lambda_1}\right)^{5+\beta} \frac{e^{hc/\lambda_1 k_B T} - 1}{e^{hc/\lambda_1 k_B T} - 1} \tag{4.16}$$

In the form of frequency I_{ν_1}/I_{ν_2} :

$$\frac{I_{\nu_1}}{I_{\nu_2}} = \left(\frac{\nu_1}{\nu_2}\right)^{3+\beta} \frac{e^{h\nu_2/k_B T} - 1}{e^{h\nu_1/k_B T} - 1} \tag{4.17}$$

Given observational values of $\lambda_1 = 100\mu m$ and $\lambda_2 = 160\mu m$, the equation of the surface brightness ratio of 100μm over 160μm becomes (taking $\beta = 2$)

$$\frac{I_{100}}{I_{160}} = 26.8 \frac{e^{90/T} - 1}{e^{140/T} - 1}, \tag{4.18}$$

which purely depends on temperature T.

If we assume $I_\lambda = B_\lambda$, the surface brightness ratio becomes

$$\frac{I_{\lambda_1}}{I_{\lambda_2}} = \left(\frac{\lambda_2}{\lambda_1}\right)^{5} \frac{e^{hc/\lambda_2 k_B T} - 1}{e^{hc/\lambda_1 k_B T} - 1}$$

Apply numerically,

$$\frac{I_{100}}{I_{160}} = 10.5 \frac{e^{90/T} - 1}{e^{140/T} - 1} \tag{4.19}$$

The surface brightness ratio function for the two cases at certain observed wavelengths have the same form except for a temperature independent coefficient. We assume that in ideal case, all the dust in the same image pixel has the same temperature. So the temperature in this equation means the physical temperature of the dust. In really, the dust in the pixel may have a range of temperatures then it is a colour temperature that only represent the mathematical temperature of the specific ratio.

Fig. 4.4 shows the relation of surface brightness ratio and the temperature described in equation (4.18).

In the upper panel of Fig. 4.4, the highest temperature is set to 30 K. We can see an almost exponential relation between the ratio and the temperature. All the
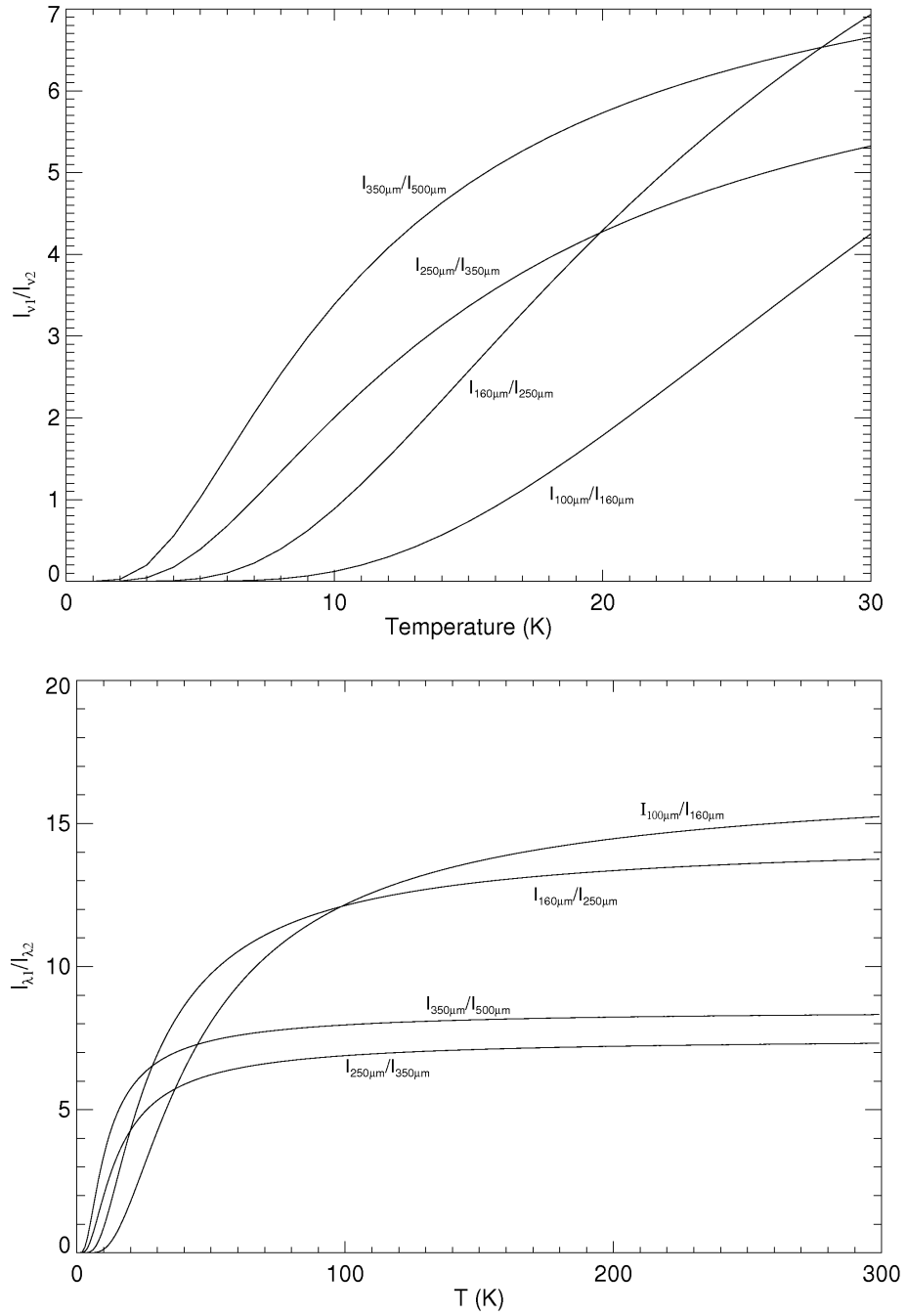
Figure 4.4: Plot of surface brightness ratio (y-axis) as a function of temperature T (x-axis). The surface brightness ratio I_{ν_1}/I_{ν_2}. Temperature is in Kelvin. The upper panel shows the relation to 30 K, the lower panel shows the relation up to 300 K. This plot is made in IDL see Appendix A.5 and A.6.

ratios show a relation that the higher temperature, the higher ratio. Comparing the 4 curves on the upper panel at 10 K, the $350\mu m/500\mu m$ ratio is much higher (about 0.3) than the $100\mu m/160\mu m$ ratio which is less than 0.01. So we conclude that the figure shows at lower temperatures, the longer wavelengths are more sensitive to dust emission. The shorter wavelengths are dominated by hotter dust.

This relation keeps correct until it goes to about 30 K which is shown at the lower panel of Fig. 4.4. We can see that at 100 K in temperature, the emission ratio is still lower at the shorter wavelength ratio but higher in longer wavelength ratio except it is not such a big difference as at low temperature. As the temperature goes up, the intensity ratio of different wavelengths all tend to become constant, as shown in the right panel of Fig. 4.4. The emission ratio are not influenced by the temperature change any more. The surface brightness ratio we observe (through the ratio map) are mostly sensitive to the low temperature/longer wavelength emission.

Based on this relation in Fig. 4.4, we are going to make surface brightness ratio maps to analyse the dust emission at long wavelength (infrared and far-infrared) for our galaxies.

4.1.5   Why Use Logarithm for the Ratio Plots and Correlation Calculation
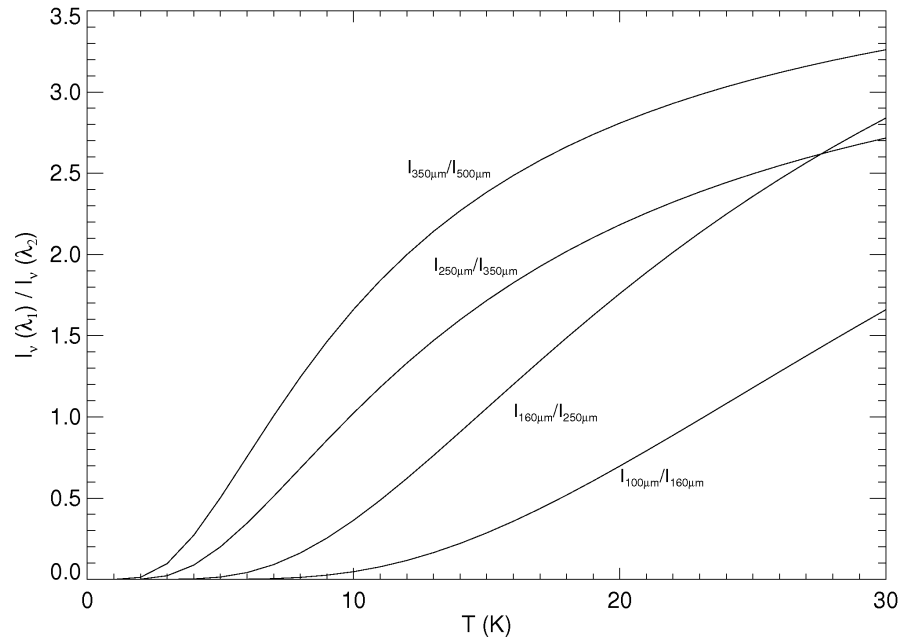
Figure 4.5: Plot of surface brightness ratios as a function of temperature T (in Kelvin). The relation is shown up to 30 K. This figure used the frequency version for the intensity I which is different to the wavelength version for the intensity in the upper panel of Fig. 4.4.This plot is made in IDL see Appendix A.8.

The colour temperatures are based on the surface brightness ratios in the form

of frequency, calculated using equation

$$\frac{I_\nu(\lambda_1)}{I_\nu(\lambda_2)} = \left(\frac{\lambda_2}{\lambda_1}\right)^{3+\beta} \frac{e^{hc/\lambda_1 k_B T} - 1}{e^{hc/\lambda_1 k_B T} - 1}, \tag{4.20}$$

which is equation (4.17) but using λ instead. Fig. 4.5 shows this relation. This plot is very similar to the upper panel of Fig. 4.4 which is a plot in the wavelength form. We use the frequency form here because the galaxy images are all in unit of Jy/arcsec, which is in units based on frequency. (But we are used to present images by wavelength, so we simply converted it by using $\nu = c/\lambda$. This is just for convenience of presenting. We use $\beta = 2$ for this calculation.)
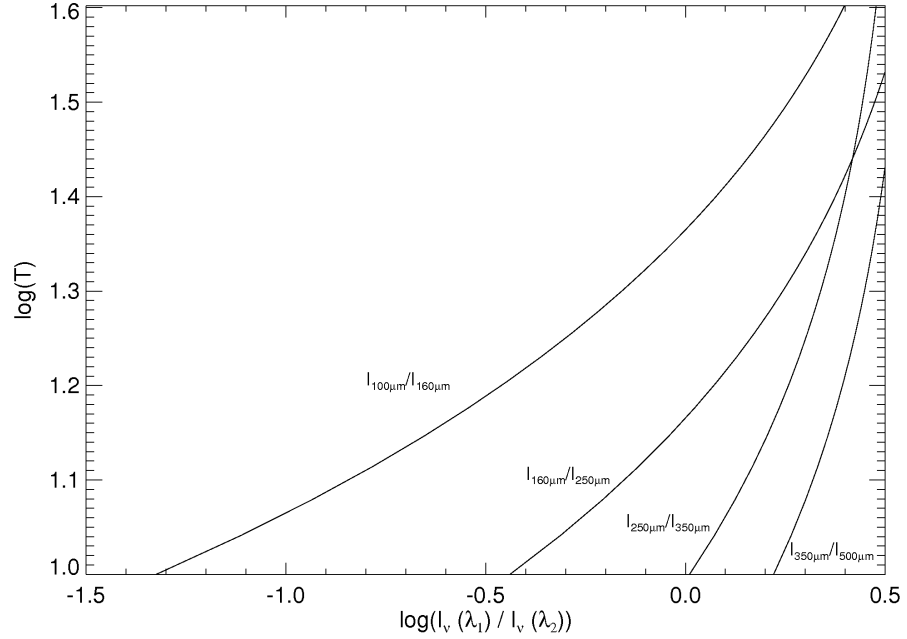
Figure 4.6: The logarithm of temperature from 10 to 40 K against logarithm of surface brightness ratios. This plot is made in IDL see Appendix A.13.

Assuming dust heating/emitting as a blackbody, so the dust is in thermal equilibrium. Assuming the total energy absorbed is derived from SF and is proportional to the Hα emission and it is a fraction of the flux of Hα, so $E_{in} = C_1 F_{H\alpha}$, where C_1 is the fraction coefficient of absorption. For convenience, we change $F_{H\alpha}$ to $I_{H\alpha}$ with another coefficient C_2 because

$$F_{H\alpha} = \int I_{H\alpha} dA. \tag{4.21}$$

where $\int dA$ is the total area.

The total energy emitted by dust is $E_{out} = C_0 T^\gamma$ where C_0 is the coefficient of emission and T is the temperature. The dust is in thermal equilibrium, so the total energy absorbed and emitted equals which gives $E_{in} = E_{out}$. This gives

$$C_2 I_{H\alpha} = C_0 T^\gamma \qquad (4.22)$$

Fig. 4.6 shows the relation of logarithm of temperature from 10 to 40 K against logarithm of surface brightness ratios. The temperature is chosen from 10 to 40K is because the data for analysis is form 100 to 500 μmand their temperatures are in the range of 10 to 40 K. From Fig. 4.6 we can see that at low temperature T can be derived to within 5% (Bendo et al., 2012a). Hence we derive the following equation from this plot

$$\log(T) \cong \alpha \log(I_{\nu_1}/I_{\nu_2}) \qquad (4.23)$$

where α is the proportional coefficient. Therefore

$$T \cong C_3 \left(\frac{I_{\nu_1}}{I_{\nu_2}}\right)^\alpha \qquad (4.24)$$

Substituting T of Equation (4.24) into equation. (4.22), we derive

$$C_2 I_{H\alpha} = C_0 C_3 \left(\frac{I_{\nu_1}}{I_{\nu_2}}\right)^{\alpha\gamma} \qquad (4.25)$$

hence we get

$$I_{H\alpha} = C \left(\frac{I_{\nu_1}}{I_{\nu_2}}\right)^\eta \qquad (4.26)$$

where

$$C = C_0 C_3 / C_2$$

$$\eta = \alpha\gamma$$

This shows a power law relation between the Hα emission and the surface brightness ratio. This power law is conveniently shown by using the logarithmic form of Equation (4.26). As follow to show the relation between the Hα emission and the surface brightness ratio.

$$\log\left(\frac{I_{\nu_1}}{I_{\nu_2}}\right) = \frac{1}{\eta}\log(I_{H\alpha}) + Const \tag{4.27}$$

where $Const = -logC$

The relation with 1.6 μm can be proved by the same way if the dust is heated by the evolved stellar population.

So in later data analysis, we use logarithm for the ratio plots against Hα emission and 1.6 μm. We also use correlation to find out how closely correlated they are.

4.2 Data Analysis of Four Herschel Observed Galaxies

From the data preparation, the maps at different wavelengths have the same resolution and PSFs, matched to the PSF of 500μm data. All these maps are created to the same pixel size of 36 arcsec as explained in previous chapters. We made colour temperature maps for NGC4254, NGC4303, NGC4321 and NGC 4579 as shown in Fig. 4.8,4.11,4.14, and 4.18. Data analysis are carried out for the four galaxies. The images on these galaxies are convolved but not rebinned. The data used in plotting are from the binned data.

We use $\beta = 2$ for the calculation for colour temperature maps. Dust emission in each pixel of the map is treated as from a single source of fixed mass and temperature. The temperature from low to high is represented by colour, from purple, blue, green to yellow, orange and red. This is shown in the colour bar at the bottom of the colour temperature maps. We can see that these colour temperature maps look notably different compared to their original images: the spiral arms in the original ones are more clear, but in these images the spiral arm structures are washed out. The

stellar and dust structures in these maps are shown in different ways. The colour temperature maps at longer wavelength bands (above 250μm) can be interpreted as the physical typical dust temperature as to the reasons discussed in previous chapters, but the shorter wavelength bands do not. The shorter wavelength bands may be dominated by a minor component of hotter dust.

As shown in Fig. 4.8, 4.11, 4.14, and 4.18, all the $350/500 \ \mu$m colour temperature maps looks much noisier than the other ones. This is because both bands sample the Rayleigh-Jeans tail of the dust SED. The Rayleigh-Jeans tail are less sensitive to temperature variations, so, the variations related to noise in the 350, 500 μm images dominate variation in the bands related to temperature.

In data analysis by ratio plots, the data points shown in plots in Fig.4.9, 4.12,4.16,and 4.19 are rebinned data into the bin size of 36 arcsec after selection of $> 5\sigma$. The data points are selected where having $S/N > 5\sigma$ for every analysed wavelength from 100μm upwards except 500μm data. This is because if we include the condition of $S/N > 5\sigma$ at 500μm there will be very few data points left for analysis. For NGC4579, we excluded the condition of 100μm greater than 5σ as well because of the need of enough data points for analysis. There are totally about 30-50 pixels selected as data points in the plots for every galaxy.

As we have described in previous chapters, the Hα image represents the star forming regions and the 1.6μm image represents the total stellar population. The Hα image shows more detail of the structure of the galaxy, in particular the spiral arms where stars are formed and some colder smaller areas where star formation is happening. The 1.6 μm image shows a more smooth radially distribution of total stellar lights concentrated towards the centre.

4.2.1   NGC4254

Colour temperature map

After the data are prepared according Chapter 3, we made the ratio of the selected data into ratio maps which are shown in Fig. 4.7. The colour bar scales are set

to show similar qualitative structure in each image. The ratio maps are made into colour temperature maps (Fig. 4.8) using the conversion described in section (4.1.5). The principal of making every map is to show the most of its structure. We can see they are very similar because they are all based on the same ratios. The ratio maps here are only a step before the colour temperature maps were made. In later galaxies we will not show the ratio maps but only show the colour temperature maps which gives more information.
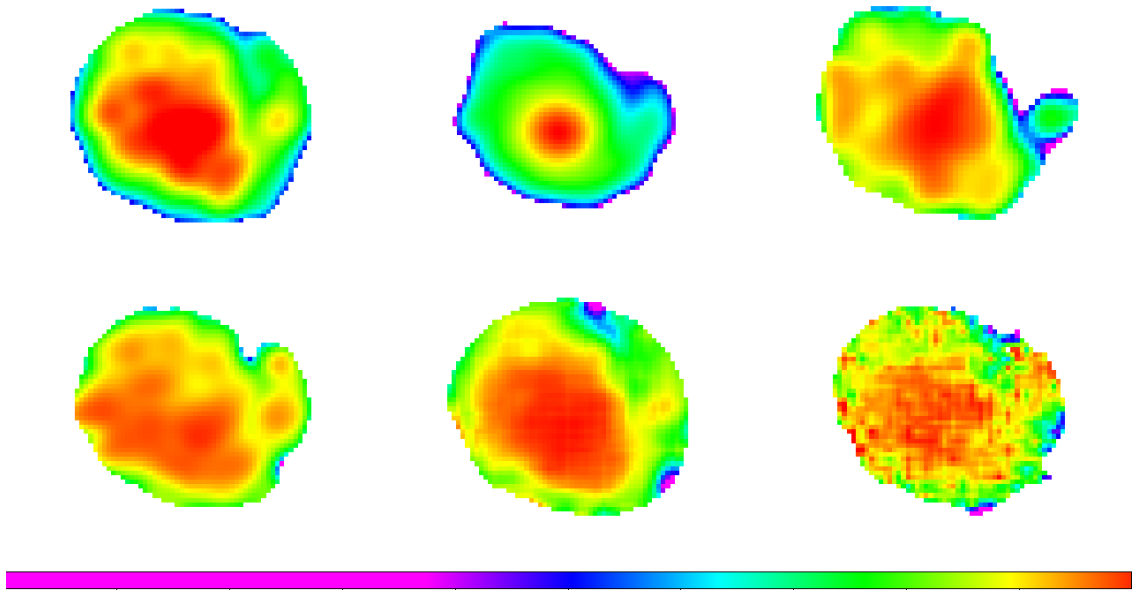
Figure 4.7: The Hα, 1.6μm maps of NGC4254 and its ratio maps. Panels from top row left to right are Hα, 1.6μm map, ratio map of 100/160, 160/250, 250/350 and 350/500 (all in μm) respectively. Data in all pixels in every panel are above 5σ level. Pixels of data lower than 5σ level are left blank (white). Each map is 540$\times$ 540 arcsec^2. The program to make these maps are in IDL in Appendix A.14.

The four colour temperature maps of NGC4254 which correspond to the ratio maps of 100/160, 160/250, 250/350 and 350/500 μm are shown in Fig. 4.8 together with its Hα and 1.6μm maps. The colours in the Hα and 1.6 μm images are not colour temperatures but intensities in unit of Jy/arcsec^2. Red colour means the highest intensity, orange, yellow, green, blue and pink means lower intensity in order. The colours in the colour temperature images represent colour temperatures. The temperature shown here is a theoretical colour temperature which is not the real temperature of the dust. Because the ratio of the longer wavelength (longer than 160 μm) is at the Rayleigh-Jeans tail of the SED so the peak of the temperature is

estimated. These colour temperatures are shown in the bar in each panel.

Figure 4.8: The Hα, 1.6μm maps of NGC4254 and its colour temperature maps. The colour temperature maps are shown in linear scale. Panels from top row left to right are Hα, 1.6μm, colour temperature map of 100/160, 160/250, 250/350 and 350/500 (all in μm) respectively. Data in all pixels in every panel are above 5σ level within the optical disc. Pixels of data lower than 5σ level are left blank (white). Each map is 540× 540 arcsec². The program to make these maps are in IDL in Appendix A.19.

The Hα map shows high intensity of Hα emission at the bulge area and large areas throughout the disc. The brighter regions appear clumpy and asymmetric. The 1.6 μm image appears brightest in the centre. The surface lightness of the star light from total stellar emission decreases with radius smoothly.

In general, all the four colour temperature maps of NGC4254 show enhanced temperature in the star forming regions. We see an asymmetric area with high temperature at the centre of the galaxy (large red area) in every map. It cools down at the outer part of the galaxy (yellow, green) and cold area at the edge (blue, purple).

The 100/160 μm image has a colour temperature range of 17-24 K.

The 160/250 μm image has a colour temperature range of 12.5-27.5 K.

The 250/350 μm image has a colour temperature range of 14.5-28.5 K.

The 350/500 μm image has a colour temperature range of 12-29 K.

Comparing the colour temperatures to the Hα and 1.6μm image, we find all the

colour temperature maps show asymmetric structures that are similar to the Hα image. This indicate that these colour temperatures are linked to star formation activity.

Ratio plots and correlations
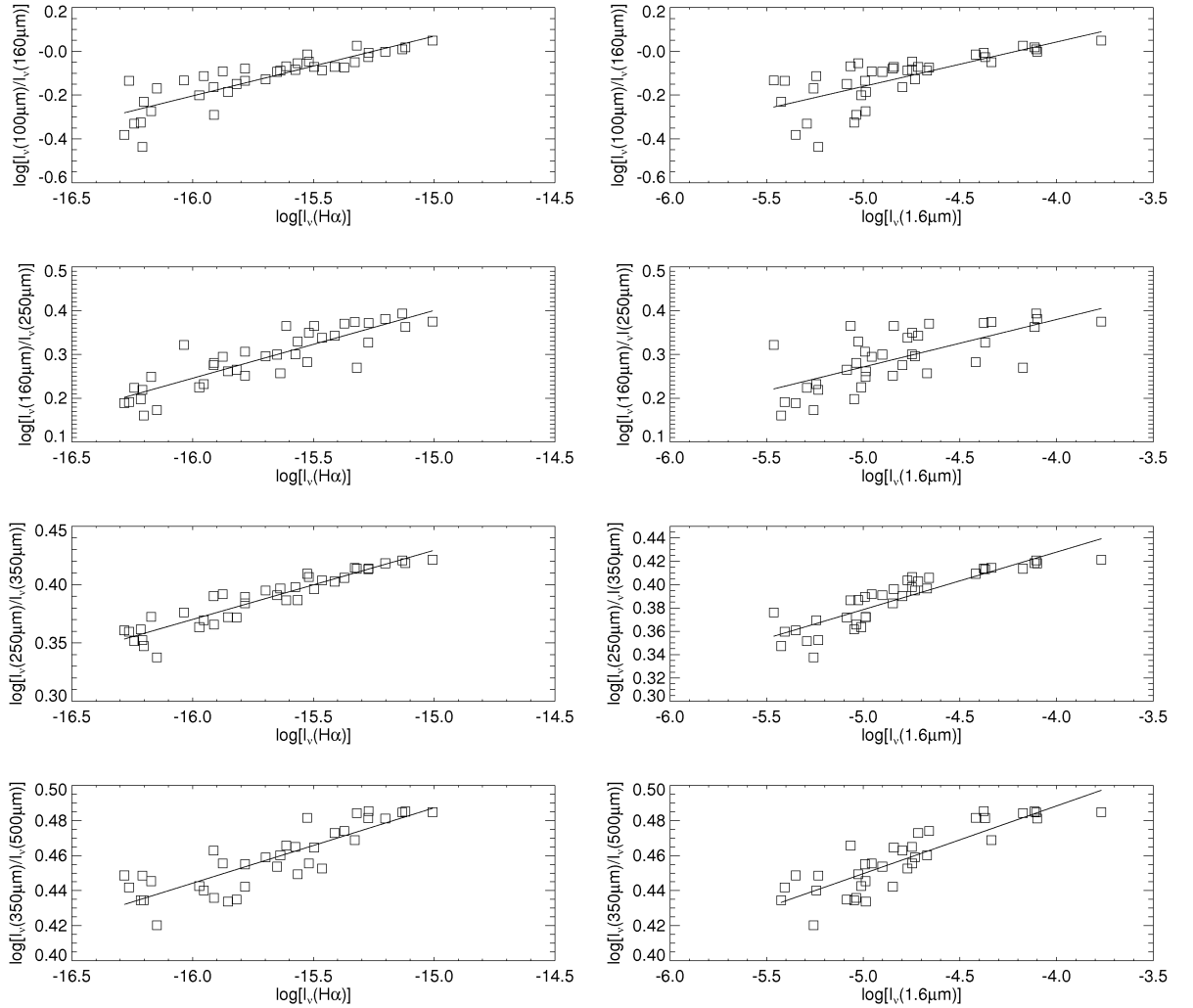
Figure 4.9: The logarithm of the surface brightness ratio against logarithm of the surface brightness of Hα and logarithm of the surface brightness of 1.6 μm. This plot is made in IDL see Appendix A.10.

Fig. 4.9 shows the logarithm of the surface brightness ratios of 100/160, 160/250, 250/350 and 350/500 μm versus the logarithm of the surface brightness of Hα and the logarithm of the surface brightness of 1.6 μm.

We make these ratio plots in logarithm because it shows the correlation more clearly at the low intensities. There are 38 data points in total in the plots. By

Table 4.1: NGC4254 correlation coefficients with Hα and 1.6μm and significant of their difference. Units of the wavelengths are all in μm.

	100/160	160/250	250/350	350/500
Hα	0.86	0.87	0.94	0.85
1.6μm	0.73	0.70	0.89	0.86
Difference	$\ll 0.01$	$\ll 0.01$	$\ll 0.01$	0.5

moving the cursor on the ratio map in DS9, the value of the pixels are readable. So the ratio in Fig. 4.9 can quickly be linked to the physical area in the corresponding colour temperature map of Fig. 4.8.

For the 100/160 μm ratio plots, the data points less than 0.5 are the pixels at the purple outer edge area at the right tail in the colour temperature map of the NGC4254. The ratio between 0.5 to 0.6 is the blue area, between 0.6 to 0.8 is the green area. 0.8 to 1.0 is the yellow and orange area. Above 1 is the red area. A bad data point at 500 μm image at pixel (4,6) is taken out.

Both plots with Hα and 1.6 μm shows an approximately linear relation but the Hα one seems to show a better correlation than the 1.6 μm one. To investigate it in more detail, we calculated the correlations coefficients which are shown in Table 4.1.

We use the CORRELATE function in IDL to calculate the correlation coefficients. The CORRELATE function computes the linear Pearson correlation coefficient of two vectors. There is a relation between the significance of the Pearson correlation coefficient and sample size (number of samples). To quantitatively define a significant difference between two correlations, we use the following method from Press et al. (1986).

First, we transform correlation coefficient r to z using

$$z = \frac{1}{2} \ln \left(\frac{1+r}{1-r} \right). \tag{4.28}$$

As a metric for assessing whether the difference between two correlation coefficients r_1 and r_2 is significant, we use

$$erfc\left(\frac{\mid z_1 - z_2 \mid}{\sqrt{2}\sqrt{\frac{1}{N_1-3} + \frac{1}{N_2-3}}}\right) \qquad (4.29)$$

where z_1 and z_2 are obtained from r_1 and r_2 using Eq.(4.28), and N_1 and N_2 are the number of data points (sample size) in the measurement of r_1 and r_2. If $r_1 = r_2$ and $N_1 = N_2$, the result is 1, which means there is no difference. The smaller the result is, the more significant difference there is. If $r_1 = 1$ and $r_2 = -1$, the result is 0 which means the correlations are unrelated.

We use a small IDL program with Eq.(4.29) to calculate the significant difference between the result of the ratios to Hα and 1.6 μmThe results are shown in Table 4.1.

Form the table we can see that most of the values are either $\ll 0.01$ or > 0.01. So in this project we define that small values ($\ll 0.01$) indicate that one correlation is much stronger than the other; large values (about 0.01 or ≥ 0.01) indicate that the correlations are similar.

The correlation coefficients between the surface brightness ratios and surface brightness of Hα and 1.6 μm image (Table 4.1) both show strong correlation. All the correlations with Hα from 100/160 to 350/500 μm are above 0.80. Interestingly, the results of the surface brightness ratios with the surface brightness of 1.6 μm also show a strong correlation. All the correlation are above 0.70. At the 250/350 μm the correlation with 1.6 μm is as high as 0.89. This means the dust in NGC4254 traces both Hα and 1.6 μm.

Comparing the correlation coefficients, The Hα have significant better correlation than the 1.6 μm correlation at 100/160, 160/250 and 250/350 μm according to the comparing result in Table (4.1). At the 350/500 μm ratio, the difference in correlation coefficient between 1.6 μm and Hα is in-significant. This implies that in this galaxy, the observed dust traces the star forming regions better than the total stellar population. This means that dust in NGC4254 is heated by the star forming regions rather than the evolved star regions. For the coldest dust, the heating source is ambiguous.

The ratio of $I_\nu(H\alpha)$ against $I_\nu(1.6\mu\text{m})$

From Fig. 4.9 we see the wavelength ratios against 1.6μm seems more curvy than the wavelength ratios against Hα. Hence we made the plot of $\log(I_\nu(H\alpha))$ against $\log(I_\nu(1.6\mu$ m$))$ which is shown in Fig.4.10.
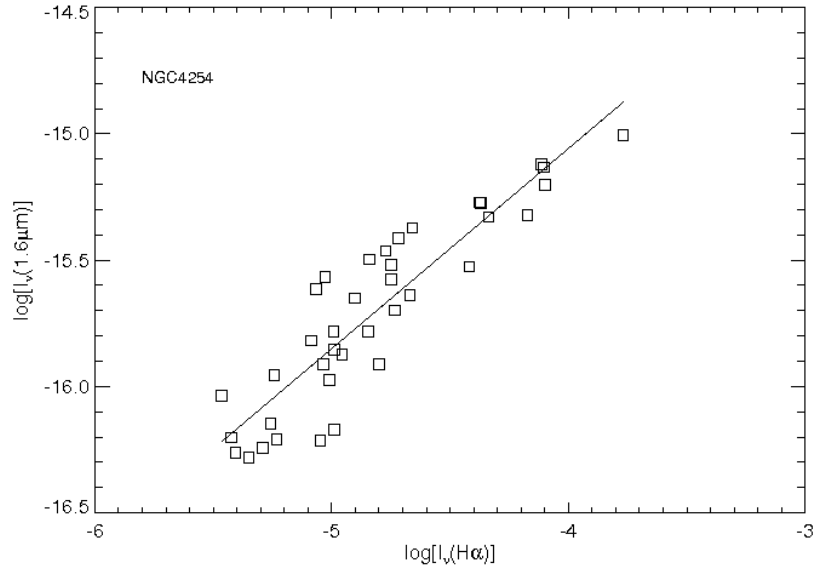
Figure 4.10: Plot of $\log(I_\nu(H\alpha))$ against $\log(I_\nu(1.6\mu\text{m}))$ for NGC4254. Program to make this plot is shown in Appendix A.18.

We can see the plot shows different slope at both ends means it is a curvy structure as well. So it explains the more curvy structure of the 1.6 μm plots.

This can also be seen by looking at the Hα and the 1.6μm maps. The Hα map contains multiple sources with similar brightnesses across the disc but the 1.6 μm image shows a smooth decrease in brightness from the centre to the edge of the optical disc. The ratio of these two maps is not linear. That is why all the 1.6 μm plots show a curved relation with the ratios.

4.2.2 NGC4303

Colour temperature map

The four colour temperature maps of NGC4303 which are 100/160, 160/250, 250/350 and 350/500 μm are shown in Fig. 4.11 together with its Hα, 1.6μm maps. In the Hα image, the centre of the galaxy doesn't have a hot core or a bulge in the centre
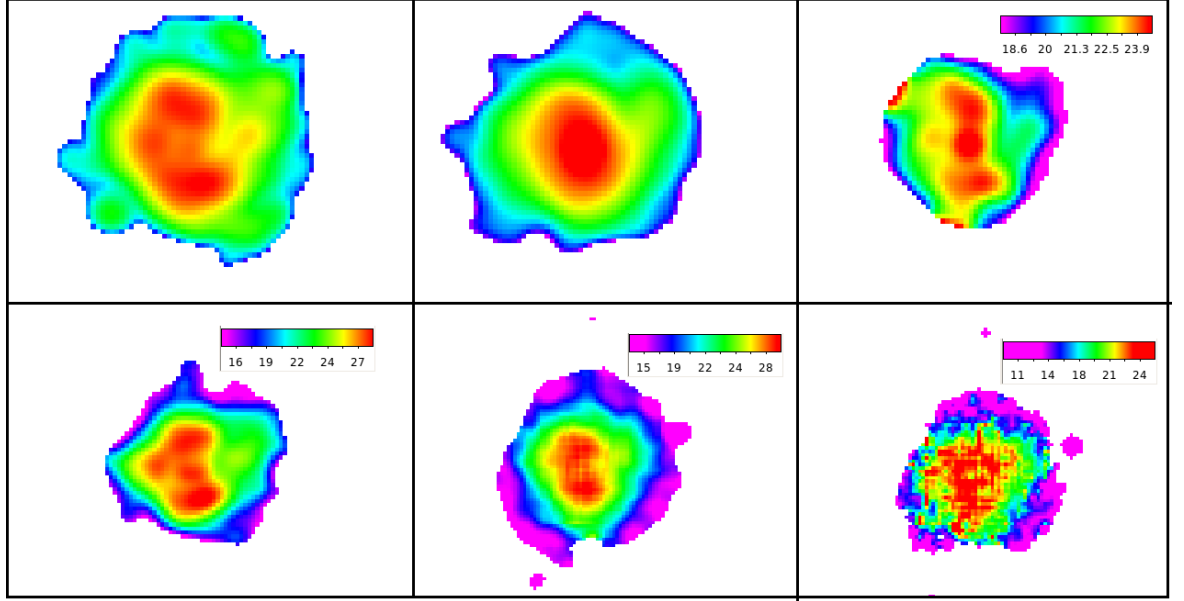
Figure 4.11: The Hα, 1.6μm maps of NGC4303 and its colour temperature maps. The colour temperature maps are shown in linear scale. Panels from top row left to right are Hα, 1.6μm, colour temperature map of 100/160, 160/250, 250/350 and 350/500 (all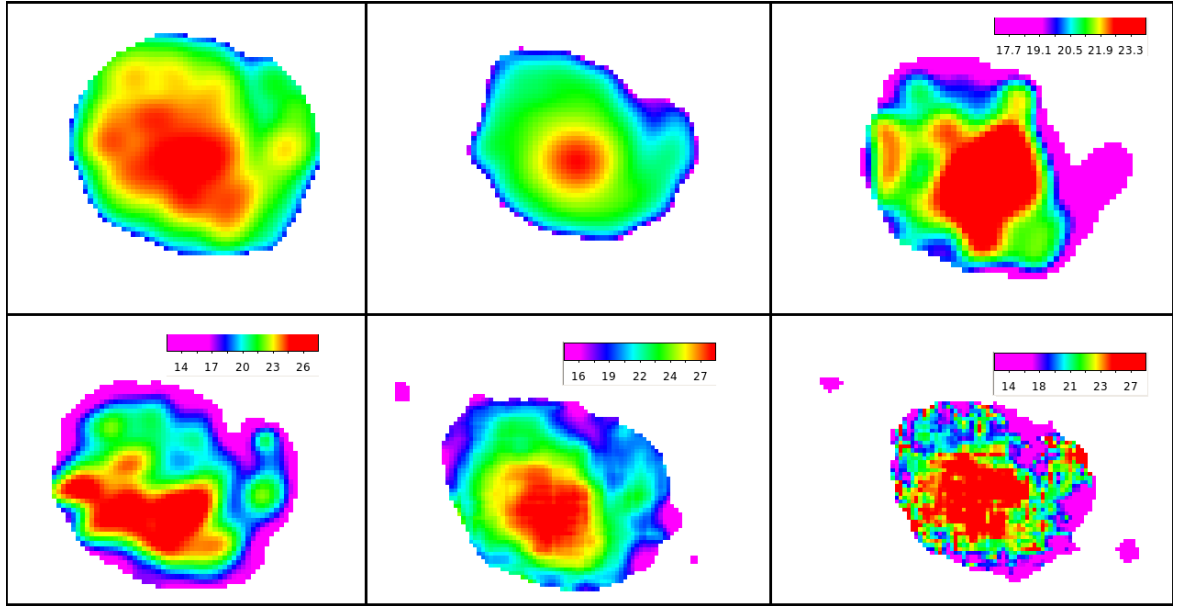 in μm) respectively. Data in all pixels in every panel are above 5σ level within the optical disc. Pixels of data lower than 5σ level are left blank (white). Each map is 612×612 arcsec². The program to make these maps are in IDL in Appendix A.19.

but the spiral arms seems have higher Hα emission than the centre core area. The spiral arms are more tightened into the centre of the galaxy and leave a large low emission area (yellow, green) at the outer part of the galaxy. The 1.6 μm image has a ellipse like high emission zone in the centre which covers the core and part of the spiral arms area of the Hα image. It also has a large lower emission area like the Hα image. The Hα and 1.6 μm images seems have similar size and area of high intensity area.

The 100/160 μm image has a colour temperature range of 18-24.5 K. It shows a hot core area like that shown in the 1.6 μm at the centre and covering part of the spiral arms as shown in the Hα image.

The 160/250 μm image has a colour temperature range of 14.5-28.5 K. The core is not as hot as the spiral arms shown which is just like the Hα image. The spiral arms are partly shown.

The 250/350 μm image has a colour temperature range of 13-30 K. The core at the centre is not as hot as the spiral arms, similar to the Hα image, but the spiral

arms are not very clear so it also looks like the 1.6 μm image.

The 350/500 μm colour temperature map has a colour temperature range of 9.5-25.5 K. It shows similarity to both the Hα image and the 1.6 μm image.

From the above comparison, some colour temperatures show similarity to the Hα image, some to the total stellar population map which is presented by the 1.6 μm image. But just by looking at the maps does not give a quantitative conclusion, so we did the following ratio plots and correlation coefficient calculation to find out the relation between the ratio and the Hα and 1.6 μm.

Ratio plots and correlations

Figure 4.12: The logarithm of the surface brightness ratio against logarithm of Hα and logarithm of 1.6 μmfor NGC4303. This plot is made in IDL see Appendix A.10.

Table 4.2: NGC4303 correlation coefficients with Hα and 1.6μm and significances of their difference. Units of the wavelengths are all in μm.

	100/160	160/250	250/350	350/500
Hα	0.82	0.89	0.92	0.85
1.6μm	0.78	0.88	0.90	0.86
Difference	0.05	0.4	0.04	0.5

Fig. 4.12 shows the logarithm of the surface brightness ratios of 100/160, 160/250, 250/350 and 350/500 μm versus the logarithm of the surface brightness of Hα and the logarithm of the surface brightness of 1.6 μm of NGC4303. Both plots with Hα and 1.6μm shows a good linear like correlation. The Hα one seems more scattered but shows a more linear correlation and the 1.6μm shows strong correlation but seems more curved. The calculated correlation coefficients and significance of their difference are shown in Table 4.2.

All the correlations between the surface brightness ratios and surface brightness of Hα from 100 to 500 μm are above 0.80 and are highly correlated. The result of the surface brightness ratio with the surface brightness of 1.6 μm also shows strong correlations which are all above 0.78. Comparing the correlation results between the Hα and the 1.6 μm, all the correlations have no significant difference (refer to Table 4.2). This implies that the observed dust in NGC4303 at all observed wavelengths traces both the hot young stars and the total stellar population equally well.

These results show that the hotter dust and the colder dust maybe all heated by both the star forming regions and the evolved star regions. So the heating cource of the dust in this galaxy is ambiguous.

The ratio of $I_\nu(H\alpha)$ against $I_\nu(1.6\mu\mathbf{m})$

From Fig. 4.12 we see the ratios against 1.6μm seems very curvy compared to the ratios against Hα. The plot of $\log(I_\nu(H\alpha))$ against $\log(I_\nu(1.6\mu$ m$))$ is shown in Fig.4.13. The plot shows that there are more data points above the best fitted line at the top part, but at the lower part they are mostly under the best fit line. This means it is not a linear relation. So it explains the more curvy structure of the 1.6 μm plots.
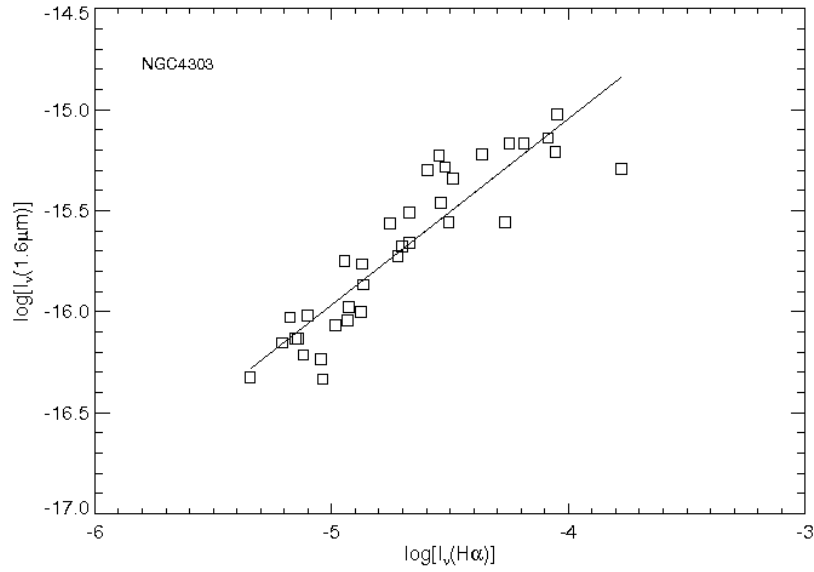
Figure 4.13: Plot of $\log(I_\nu(H\alpha))$ against $\log(I_\nu(1.6\mu$ m$))$ for NGC4303. Program to make this plot is in Appendix A.18.

This can also be explained by looking at the Hα and the 1.6μm maps. The Hα map contains a quite clear spiral arms structure and low emission in the bulge area but the 1.6 μm map shows a centre to edge / high to low smooth decrease in brightness. This is why the ratio of these two maps would not be linear.

4.2.3 NGC4321

Colour temperature map

The four colour temperature maps of NGC4321 which are ratios of 100/160, 160/250, 250/350 and 350/500 μm are shown in Fig. 4.14 together with its Hα, 1.6μm maps. In the Hα image, the centre of the galaxy shows the highest intensity core or bulge at the centre. The spiral arms surrounding it also show high intensity. The spiral arms are also tightened into the centre of the galaxy and leave a lager lower intensity area (yellow, green) at the outer part of the galaxy. The 1.6 μm image has a larger ellipse like high intensity core in the centre which covers the bulge and some of the spiral arms area of the Hα image horizontally, but also shows the outer spiral arms in high intensity as a warm orange colour. It also has a large cooler area, like the Hα image.

Figure 4.14: The Hα, 1.6μm maps of NGC4321 and its colour temperature maps. The colour temperature maps are shown in linear scale. Panels from top row left to right are Hα, 1.6μm, colour temperature map of 100/160, 160/250, 250/350 and 350/500 (all in μm) respectively. Data in all pixels in every panel are above 5σ level within the optical disc. Pixels of data lower than 5σ level are left blank (white). Each map is 540× 684 arcsec². The program to make these maps are in IDL in Appendix A.19.

We can see that all the colour temperatures have a similar hot central core, and the spiral arm structures are much clearly seen than in either NGC4254 or NGC4303. It has large cooler area (yellow, green) at the outer part of the galaxy.

The 100/160 μm image has a colour temperature range of 15-22 K. It has a hot core larger than the hot bulge of the Hα image. It is more like the 1.6 μm image, but part of the spiral arms also show the Hα image structure.

The 160/250 μm image has a colour temperature range of 13-23 K. This colour temperature map of NGC4321 shows an unexpected cold blue area near the centre on the left top spiral arm area and the bulge is shifted lower. This has been studied in section 3.11 in Chapter 3. The figure of 160/250 μm colour temperature map shown in Fig.4.14 is the corrected one but it is still not good enough for data analysis.

The 250/350 μm image has a colour temperature range of 16-25 K. Comparing the 250/350 μm colour temperature map to the Hα image and the 1.6 μm image, it is more of a combination of the two images.

The 350/500 μm colour temperature map appear to be very noisy and it is hard

Table 4.3: NGC4321 Correlation coefficients with Hα and 1.6μm

	100/160	160/250	250/350	350/500
Hα	0.88	0.39	0.91	0.72
1.6μm	0.87	0.19	0.89	0.76

to tell if the dust traces the star forming region or the total stellar population by just looking at the image. The result is analysed from the correlation coefficient calculation later.

Ratio plots and correlations
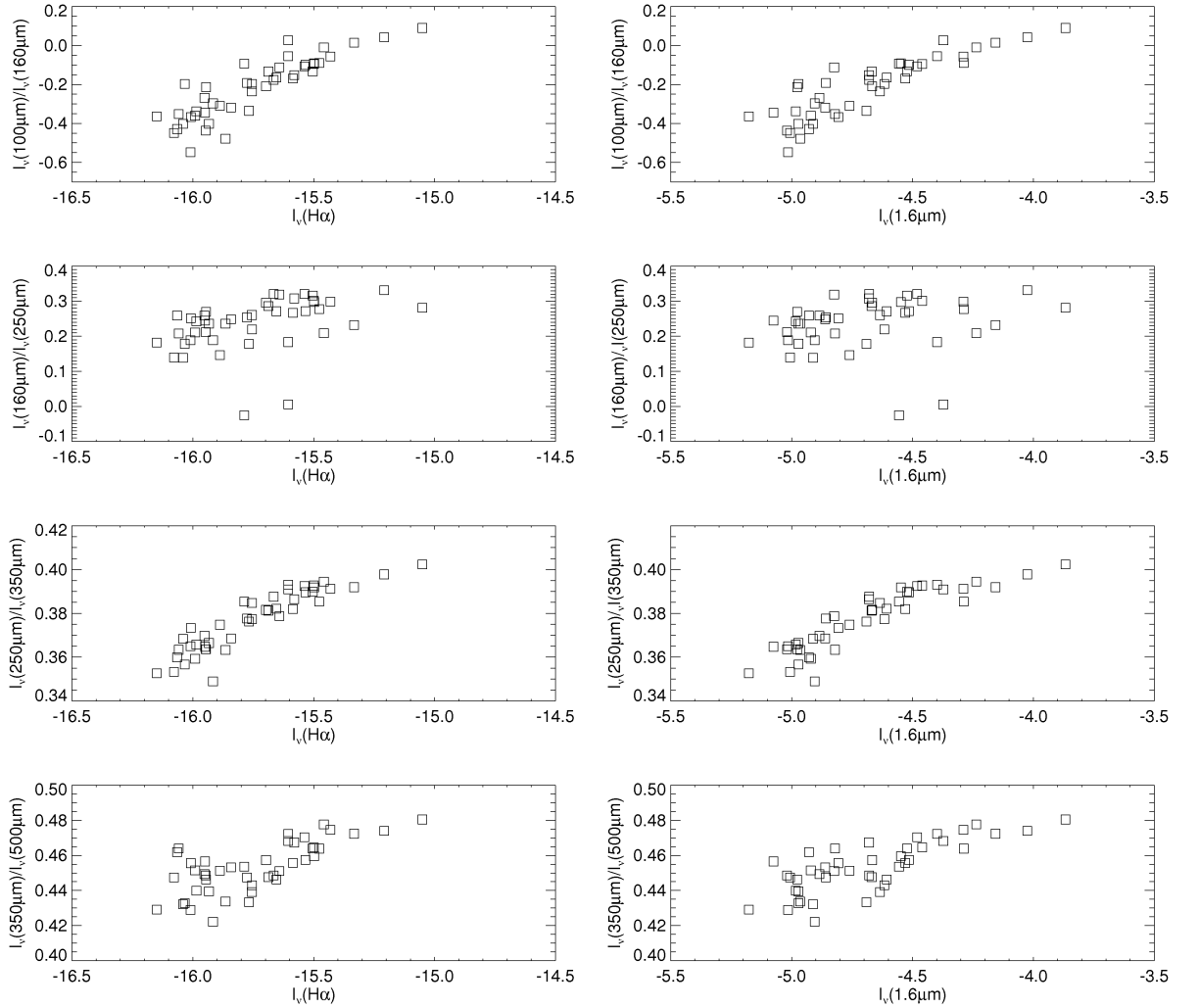
Figure 4.15: The logarithm of the surface brightness ratio against logarithm of Hα and logarithm of 1.6 μm. This plot is made in IDL see Appendix A.10.

Figure 4.15 shows the logarithm of the surface brightness ratios of 100/160, 160/250, 250/350 and 350/500 μm versus the logarithm of the surface brightness

of Hα and the logarithm of the surface brightness of 1.6 μm of NGC4321 before correction. Table 4.3 shows the correlation coefficients according to the plot. We can see that the 160/250 μm plot is very scattered and the correlations also show very poor results of under 0.40.

We ignore this result and plot the new plots and calculate the correlations with corrections according to the study about this in Chapter 3. The two pixels are taken out not only from the 160μm data, they are taken out from all the other wavelength data as well. So all the plots and correlations are changed accordingly.
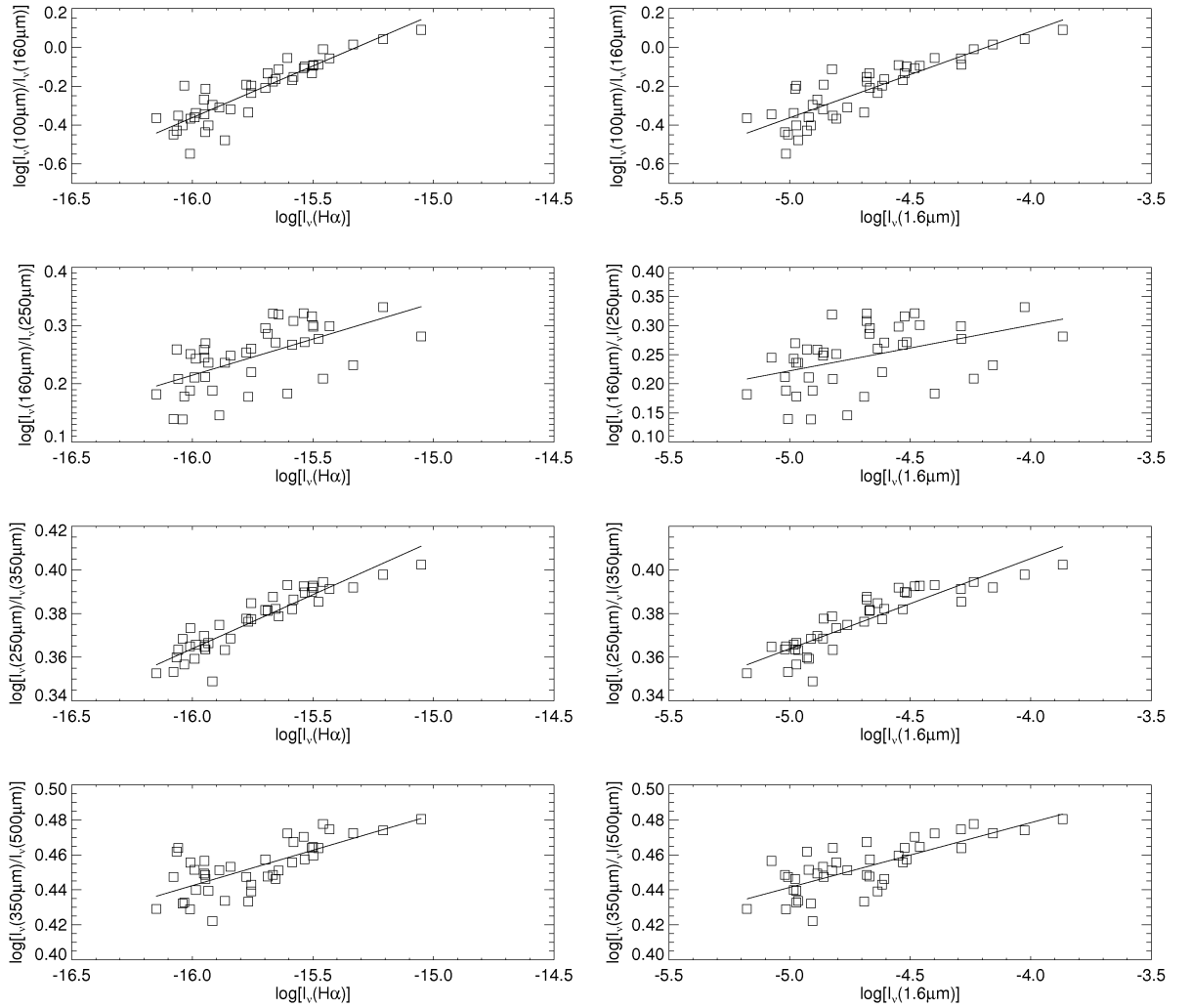
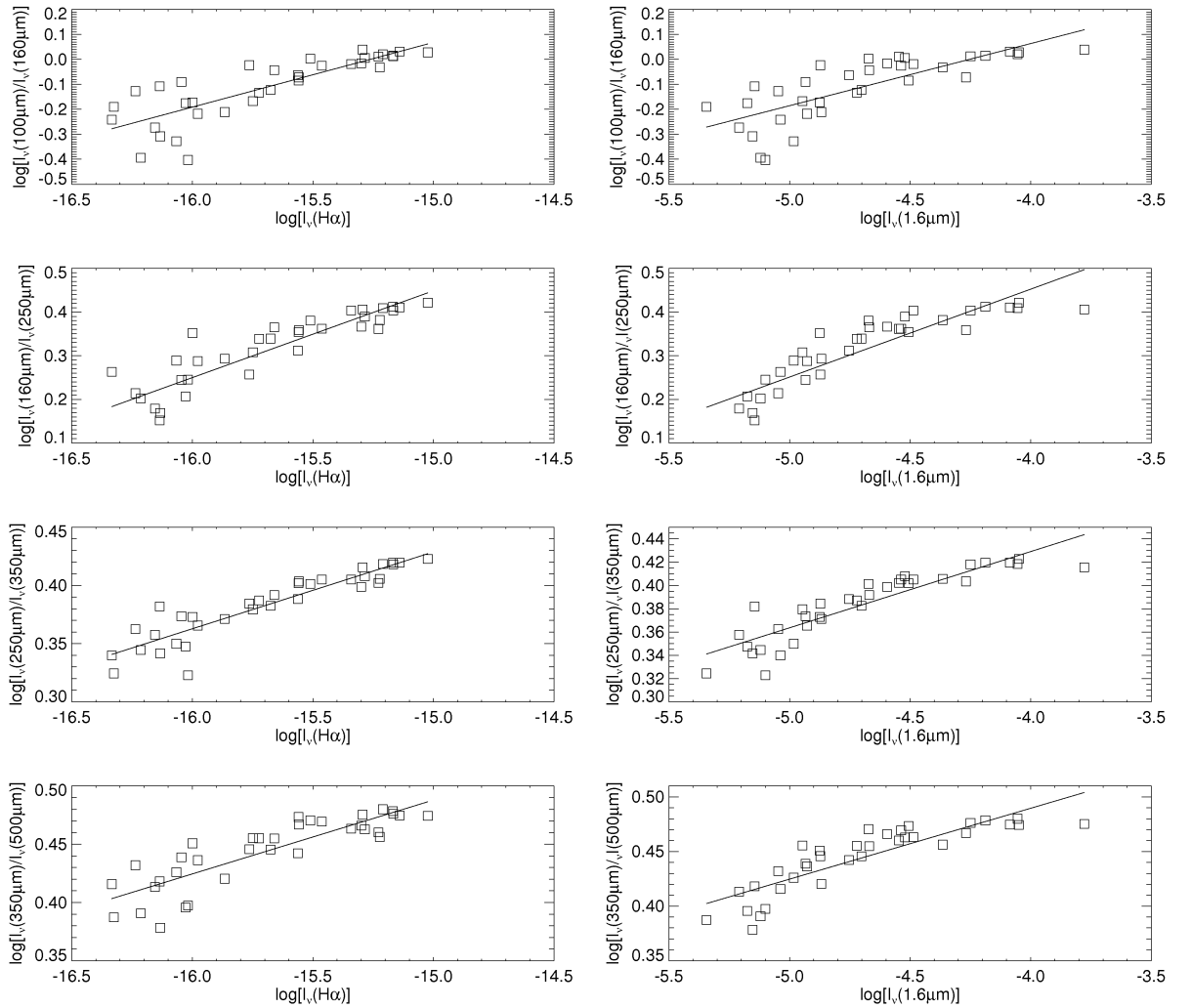Figure 4.16: The logarithm of the surface brightness ratio against logarithm of Hα and logarithm of 1.6 μm with the bad data area subtracted for NGC4321. This plot is made in IDL, see Appendix A.12.

Fig. 4.16 shows the logarithm of the surface brightness ratios of 100/160, 160/250, 250/350 and 350/500 μm versus the logarithm of the surface brightness

Table 4.4: NGC4321 correlation coefficients with Hα and 1.6μm and significances of their difference. Units of the wavelengths are all in μm.

	100/160	160/250	250/350	350/500
Hα	0.90	0.61	0.92	0.71
1.6μm	0.87	0.45	0.89	0.76
Difference	0.01	$\ll 0.01$	< 0.01	0.06

of Hα and the logarithm of the surface brightness of 1.6 μm of NGC4321 after the bad data points are subjected. The correlation coefficients and comparison with differences are shown in Table 4.4. In this galaxy, the 100/160 μm correlation coefficients of the Hα and 1.6 μm have no significant difference. This similarity shows that the dust observed in this galaxy traces both the hot young stars in the star forming region and the evolved stars in the total stellar population. In this galaxy, the hotter dust can also be heated by the evolved stars which is not the same as NGC4254.

The 160/250 μm plots still show very scattered data points after the correction. The correlation have very poor results compare to other results. The Hα plot is less scattered than the 1.6μm one and has a correlation coefficient of 0.61. The 1.6μm one only has 0.45 which is under 0.50. The comparison shows little difference between the two results because of this poor result of correlation. The poor result might be because the wrong data which gives the ultra-cold area in 160μm map is larger than the deleted pixels which causes a large uncertainty on the results. Also, the 160 μm image is taken by PACS instrument and 250μm image is taken by SPIRE instrument. Different instruments may cause differences of these two images together with the wrong data of this galaxy. So we discard this result in our analysis.

The 250/350 μm ratio again shows very close result with both Hα and 1.6 μm in high correlation coefficient results (0.89 and 0.92) and shows no difference in comparison. This indicates the dust at longer wavelength ratios in NGC4321 might be heated by both young stars and older stars.

At the 350/500 μm ratio, the correlation with Hα and 1.6 μm also shows no difference. This again implies that lower temperature dust in NGC4321 traces the total stellar population equally well as the star forming regions. So the heating

source for the cold dust is not defined in this galaxy.

The ratio of $I_\nu(H\alpha)$ against $I_\nu(1.6\mu$ m)

From Fig.4.16 we see the wavelength ratios against 1.6μm and the wavelength ratios against Hα seems linear. We also made the plot of $\log(I_\nu(H\alpha))$ against $\log(I_\nu(1.6\mu$ m)) which is shown in Fig.4.17.
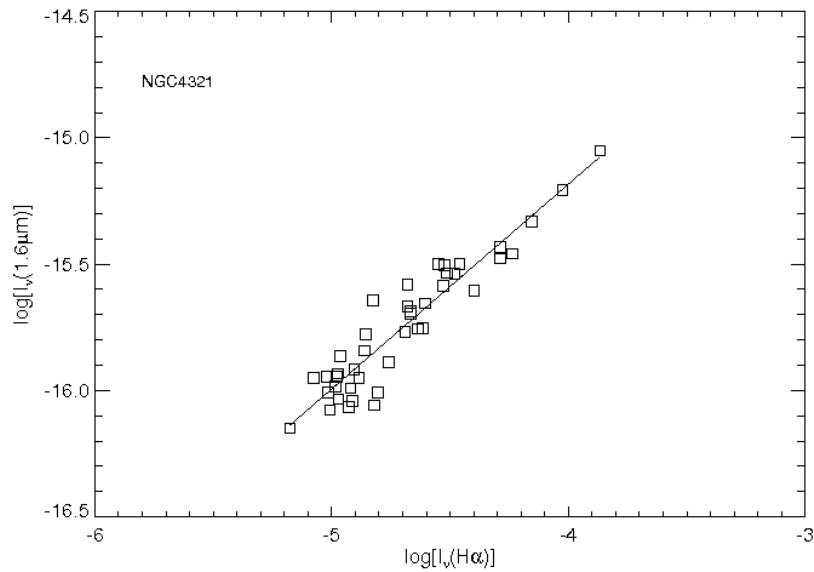
Figure 4.17: Plot of $\log(I_\nu(H\alpha))$ against $\log(I_\nu(1.6\mu$ m)) for NGC4254. The program to make these maps are in IDL in Appendix A.18.

The plot shows a linear relationship between the $\log(I_\nu(H\alpha))$ and the $\log(I_\nu(1.6\mu$ m)) of NGC4321.

Looking at the Hα and the 1.6μm maps, the 1.6μm map roughly shows the outline structure of the spiral arms while the Hα map shows clearer spiral arms but they dominated the same area. This similarity of the maps gives the more linear like relationship.

4.2.4   NGC4579

Colour temperature map

The colour temperature maps of surface brightness ratios of 100/160, 160/250, 250/350 and 350/500 (all in μm) of NGC4579 are shown in Fig. 4.18 together

with its Hα and 1.6μm maps. The Hα map shows high intensity of Hα emission in the bulge area at the centre of the galaxy. The spiral arms also have high Hα emission but the structures are not very clear. They are shown in warm orange colour. The outer galaxy smoothly changes into a lower intensity of emission from yellow to green to blue. The 1.6 μm image also shows a high intensity red circular bulge at the same location as the Hα image. Outside of the bulge, the intensity of the star light from total stellar emission goes down smoothly.
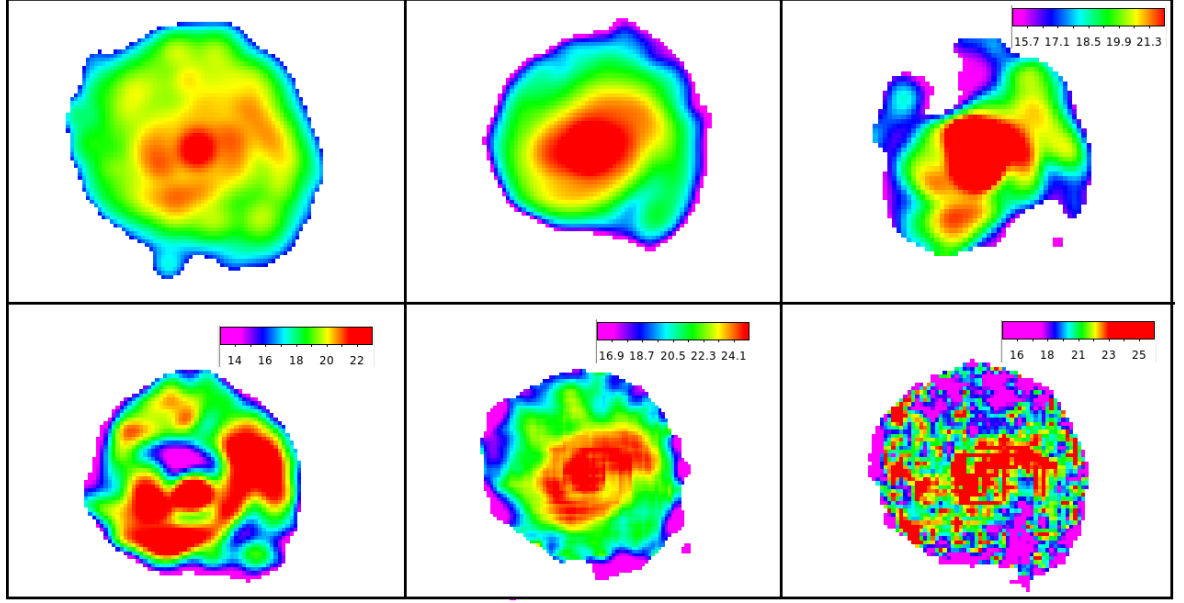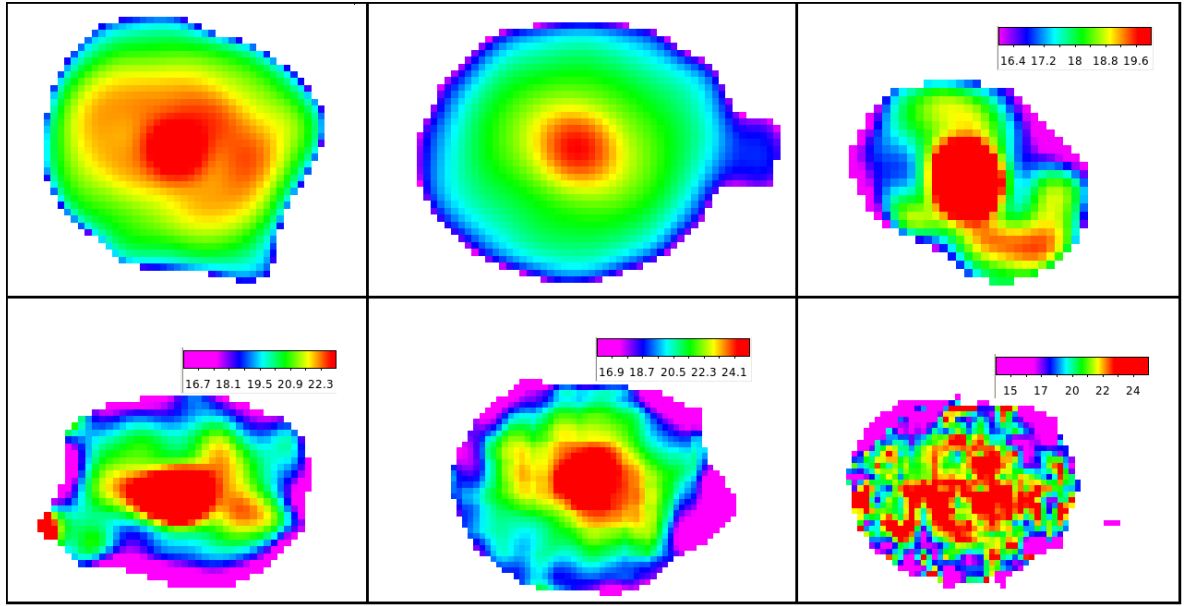

Figure 4.18: The Hα, 1.6μm maps of NGC4579 and its colour temperature maps. The colour temperature maps are shown in linear scale. Panels from top row left to right are Hα, 1.6μm, colour temperature map of 100/160, 160/250, 250/350 and 350/500 (all in μm) respectively. Data in all pixels in every panel are above 5σ level within the optical disc. Pixels of data lower than 5σ level are left blank (white). Each map is 684$\times$ 540 arcsec^2. The program to make these maps are in IDL in Appendix A.19.

From the colour temperature maps, we can see that all the maps have a circular shaped hot red core at the centre of the galaxy (the 350/500 one is not very clear). The spiral arms structure is much less clearly seen but partly shown in different ratios. It has large cool area (yellow, green) at the outer part of the galaxy.

The 100/160 μm image has a colour temperature range of 16-20 K. The bulge area is the hottest area which is the same as the Hα and 1.6 image. The spiral arms shown in this map just show a small part of the spiral arms but is not the strong intensity area shown in the Hα map.

Table 4.5: NGC4579 correlation results and with Hα and 1.6μm and difference comparison.

	100/160	160/250	250/350	350/500
Hα	0.75	0.85	0.97	0.57
1.6μm	0.85	0.84	0.94	0.66
Difference	$\ll 0.01$	0.5	$\ll 0.01$	0.01

The 160/250 μm image has a colour temperature range of 16-25 K. The bulge is hot and red in the centre of galaxy but not in a circular shape like the Hα and the 1.6 μm images. The spiral arms are partly shown.

The 250/350 μm image has a colour temperature range of 16-23 K.The bulge is hot and red in the centre of galaxy and have a enlarged red area half way of where the spiral arms are. It looks both like the Hα and the 1.6 μm images.

The 350/500 μm image has a colour temperature range of 14-25 K. The image seems noisy so it is hard to say which image it follows.

The above comparison indicate that the dust in this galaxy seems to be heated by both the hot young stars from the star forming region and the evolved stars from the total stellar population region.

Ratio plots and correlations

Fig. 4.19 shows the logarithm of the surface brightness ratios versus the logarithm of the surface brightness of Hα and the logarithm of the surface brightness of 1.6 μm in NGC4579. Both plots with Hα and 1.6 μm show a good linear correlation. Different to the other three analysed galaxies, the 1.6μm one shows a stronger linear relation than the Hα one. The calculated correlations and difference comparison are shown in Table 4.5.

Differently to the other three analysed galaxies, the hotter dust in NGC4579 represented by 100/160 μm has a much stronger correlation with the total stellar population than with the star forming regions. So in this galaxy, it has a strange result that the hotter dust traces the total stellar population more than the star forming regions.

The 250/350 μm shows a higher correlation coefficient to Hα than 1.6 μm. This
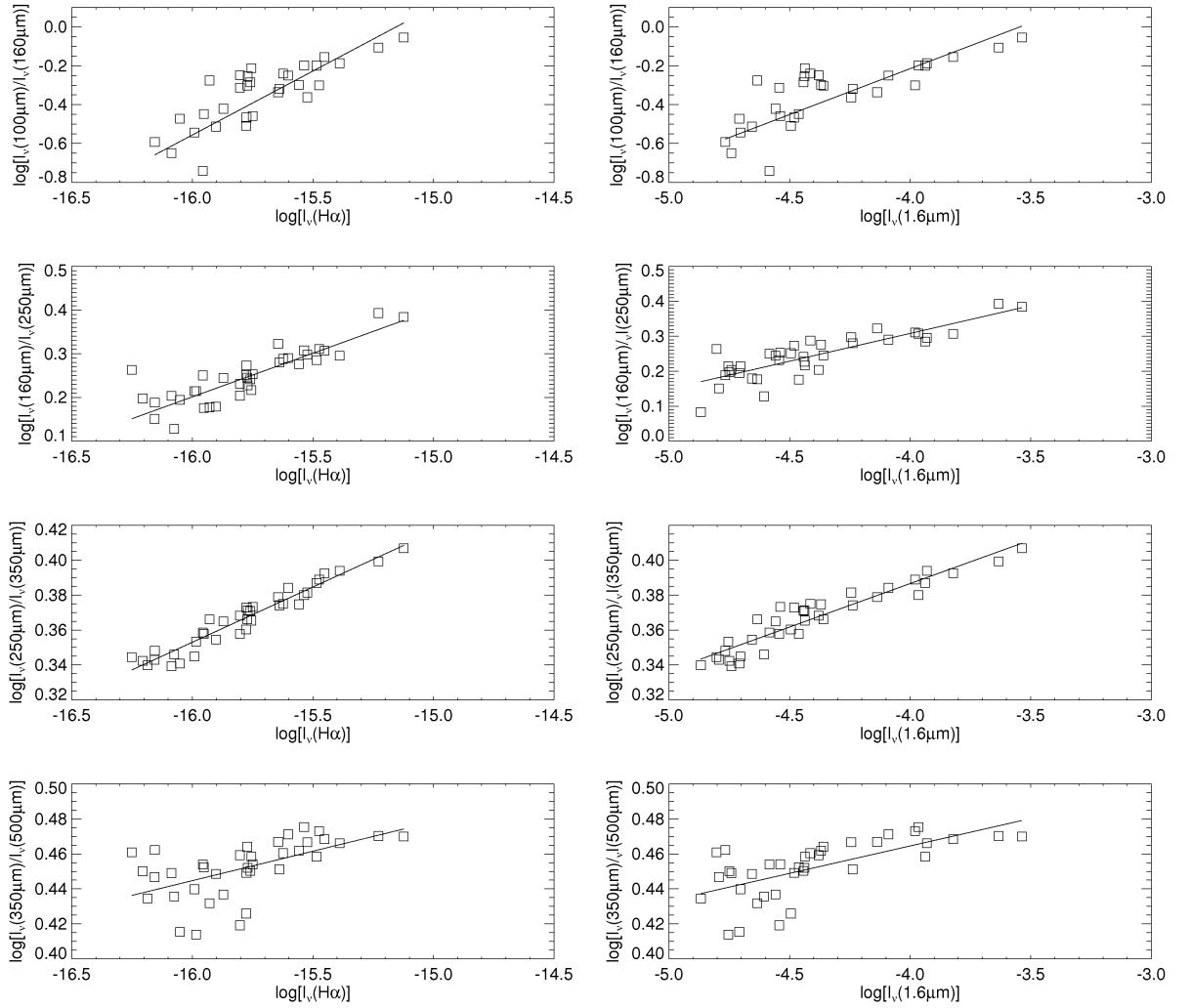
Figure 4.19: The logarithm of the surface brightness ratio against logarithm of Hα and logarithm of 1.6 μmof NGC4579. The unit of the y axis is arbitrary. The unit of the x axis is logarithm of Jy/arcsec^2. This plot is made in IDL, see Appendix A.10.

result indicate that more cold dust in NGC4579 could be heated by the star forming regions.

The 160/250 and the 350/500 μm correlation coefficients do not have any significant difference between Hα and 1.6μm according to Table 4.5: they trace both star forming regions and the evolved stars regions. The 350/500 μm correlations of this galaxy are significantly lower than for other galaxies (both under 0.7). The reason for the low correlation might be because of the low resolution of the image of 500μm of this galaxy.

Also, because the images of 100 and 160 μm have artifacts with the edge effect, the correlations of 100/160 and 160/250 may be ambiguous.

The ratio of $I_\nu(H\alpha)$ against $I_\nu(1.6\mu$ m)

From Fig.4.19 we see the ratios against $H\alpha$ and the 1.6μm seems both linear. We also made the plot of $\log(I_\nu(H\alpha))$ against $\log(I_\nu(1.6\mu$ m)) which is shown in Fig.4.20.
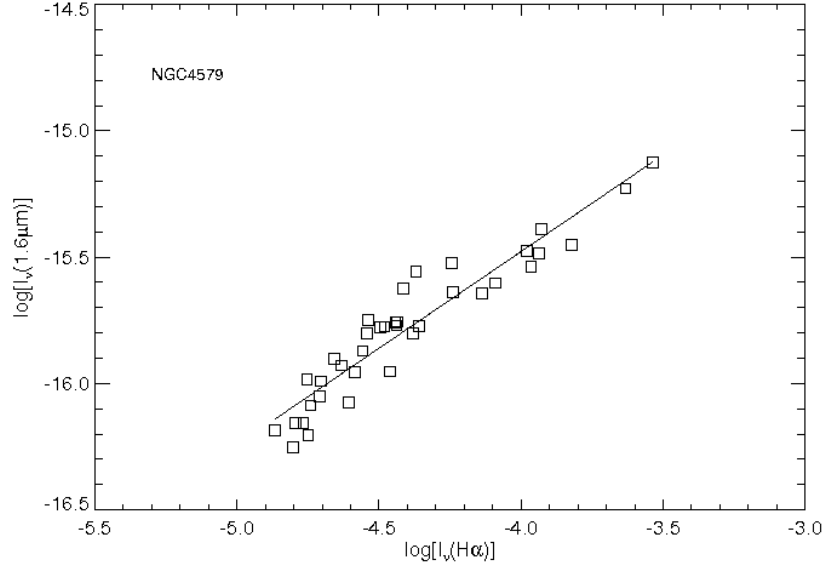
Figure 4.20: Plot of $\log(I_\nu(H\alpha))$ against $\log(I_\nu(1.6\mu$ m)) for NGC4254. Program to make this plot is shown in Appendix A.18.

The plot shows a mainly linear like distribution but there are a few more data points above the best fitted line in the middle. This is consistent with the data distribution in the panels of ratio against 1.6μm in Fig.4.19.

This can also be explained by looking at the $H\alpha$ and the 1.6μm maps. The spiral arms structure is not very clear in the $H\alpha$ map. The centre of the 1.6 μm map is not a circle but stretched to where the spiral arms are, so it is not greatly different to the $H\alpha$ map. So the ratio of these two maps would be more close to be linear.

4.3   Problem of the colour temperatures and the value of β

Looking at the temperatures of the colour temperature maps of the four galaxies, we find that the temperatures are unexpectedly high at longer wavelengths. We expected the temperatures should all have similar temperature range because they
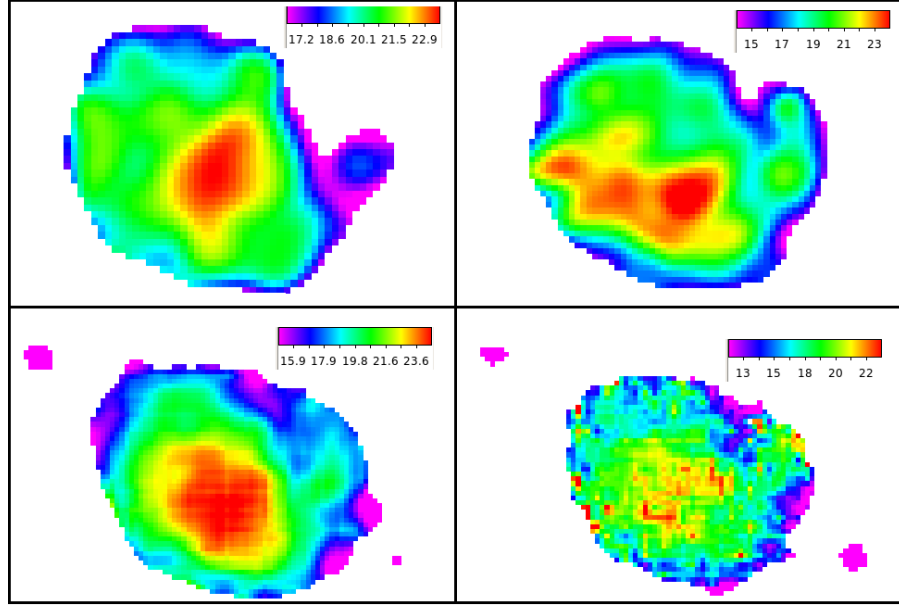
Figure 4.21: Colour temperature maps of NGC4254 using $\beta = 2.2$. The order of the maps are from left top to right of ratios 100/160, 160/250, 250/350 and 350/500 (all wavelengths in μm) respectively.

Table 4.6: Colour temperature value of $\beta = 2.2$ and $\beta = 2$.

Ratio	Colour Temperature with $\beta = 2.2$ (K)	Colour Temperature with $\beta = 2$ (K)
100/160	16.5-23.5	17-24
160/250	13.5-24.5	12.5-27.5
250/350	15-24.5	14.5-28.5
350/500	12-23	12-29

are based on ratios from the blackbody emission which is discussed in the theory part of this chapter. The ratio at the Rayleigh-Jeans tail of any temperature or mass should have the same value. A reason for this higher temperature could be that we took the wrong value of β when we considered the absorption opacity κ of dust emission.

The value of β we took for all the calculation is $\beta = 2$. Here for a trial we changed the value of β and made $\beta = 1$. The result went even worse. The temperature range for 350/500 μm of NGC4254 went up to 91 K. Hence we tried the opposite way, let $\beta = 2.2$. The result is shown in Fig. 4.21 and the temperature is shown in Table 4.6. I also put the temperature for $\beta = 2$ as a comparison.

The colour temperatures all give about the same range for all the ratios. So $\beta = 2.2$ should be the best value for this galaxy. The meaning of the value of β is

not the purpose of this project so I leave it as a future study.

Chapter 5

Conclusion

Dust is heated through the absorption of photons. Dust can be heated by both hot young stars and evolved stars. It is important to find out which one is the main source for dust heating because then we can use dust emission as a SFR tracer or a total stellar population tracer. There is still a lot of argument on this. To find out a clear answer, we use Herschel data from HRS and HeViCS at 100, 160, 250, 350, and 500 μm which trace dust emissions at temperature 5 to 30 K. We find Herschel data is excellent for this study because it provides sensitivity, it gives adequate resolution, and it covers the full range of required wavelengths. Working with the 500 μm image limited my study because we do not see much detail due to the low angular resolution.

We studied the nearby face-on spiral galaxies of NGC4254, NGC4303, NGC4321 and NGC4579 towards the Virgo cluster. The data was convolved and rebinned into 36 arcsec bins for the analysis. We encountered no major issues with the data in the data preparation process except for the 160 μm image of NGC4321, which is affected by a data processing artifact. The 100 and 160 μm images of NGC4579 fall at the edge of the mapped region and are noisier than average. We used three methods to analyse the data: colour temperature maps (based on ratio map), ratio plots and correlation coefficients.

We compared all the data points of the colour temperature maps (100/160, 160/250, 250/350 and 350/500 ratio maps) to the Hα and the 1.6 μm images and

Table 5.1: Table of correlation coefficients with Hα for four galaxies. Units of the wavelengths in ratios are all in μm.

	100/160	160/250	250/350	350/500
NGC4254	0.86	0.87	0.94	0.85
NGC4303	0.82	0.89	0.92	0.85
NGC4321	0.90	0.61	0.92	0.71
NGC4579	0.75	0.85	0.97	0.57

Table 5.2: Table of correlation coefficients with 1.6μm for four galaxies. Units of the wavelengths in ratios are all in μm.

	100/160	160/250	250/350	350/500
NGC4254	0.73	0.70	0.89	0.86
NGC4303	0.78	0.88	0.90	0.86
NGC4321	0.87	0.45	0.89	0.76
NGC4579	0.85	0.84	0.94	0.66

analysed which show a better correlation. The result is not as clear as we had expected. All the results of the four galaxies show a strong correlation with both Hα and the 1.6 μm images. This implies that all the galaxies in this study trace both SFRs and total stellar population. Table 5.1 summarises all the correlations with Hα and Table 5.2 shows all the correlations with 1.6 μm.

NGC4303 and NGC4321 strongly support the above conclusion because both of them show strong and similar correlations to the Hα and 1.6 μm. This indicates that the dust in these two galaxies traces both star forming regions and the total stellar population region. Dust in these two galaxies could be heated by both young hot stars and evolved stars.

NGC4254 shows a better correlation between the colour temperature maps with the Hα image than the 1.6 μm image at wavelength ratio at 100/160, 160/250, and 250/350 μm. If we say the 100/160 and 160/250 μm ratios represent the hotter dust and the 250/350 and 350/500 μm ratios represent colder dust, this result could indicate that hotter dust and some colder dust in NGC4254 are heated by star forming regions rather than the evolved stars. Table 5.3 shows the summarised results of the significant difference.

NGC4579 shows a better correlation at 1.6 μm than Hα at 100/160 and 350/500 μm. This could indicate a possibility that in NGC4579, some hotter dust is heated

Table 5.3: The significance of difference between correlation coefficients of ratio maps to Hα and 1.6μm images.

Ratio of wavelength (μm)	100/160	160/250	250/350	350/500
NGC4254	$\ll 0.01$	$\ll 0.01$	$\ll 0.01$	0.5
NGC4303	0.05	0.4	0.04	0.5
NGC4321	0.01	$\ll 0.01$	< 0.01	0.06
NGC4579	$\ll 0.01$	0.5	$\ll 0.01$	0.01

by the hot young stars and some of the colder dust is heated by the evolved stars. But the result of NGC4579 may be ambiguous because of the edge effect on the image for 100 and 160μm.

We conclude that dust traces both Hα and 1.6 μm in these four galaxies, except a better correlation with Hα in NGC4254. There is no clear evidence for a dust component which is heated only by the evolved stars. Comparing my results to a similar study in M81, M83 and NGC2403 by Bendo et al. (2012a), we find little evidence for colder dust tracing evolved stars in NGC4254, NGC4303, NGC4321 and NGC4579. From the colour temperature maps, I find dust temperatures in the range of 12-30 K assuming that $\beta = 2$. There is no evidence for dust at lower temperature than 12 K.

All the four galaxies show a higher temperature of dust at longer wavelengths which is unexpected. We have tried to change the value of β to $\beta = 2.2$ to fix the problem. Further study is needed to determine if β is indeed higher than 2 in these and possibly other galaxies.

Appendix A

IDL Programmes

A.1 change_Ha_unit.pro

The program in IDL to convert the unit of H_alpha images.

```
;Read in the data.
img=readfits(fileprefix+'.fits',head)


;get the value for zero point
zp=double(sxpar(head,'P_ZEROPO'))
;zp4254=-14.36
;zp4303=-15.11
;zp4321=-14.35
;zp4579=-14.75


;get the value for log(counts/image)
;Not using this one because image have minus values make log a nan.
;logCnts=alog10(img)


;get the value for exposure time
Texp=sxpar(head,'TM-EXPOS')
```

```
  if Texp eq 0 then Texp=sxpar(head,'EXP-TIME')


;texp4254=1800.1

;texp4303=600

;texp4321=1800.03

;texp4579=600


;Calculate the flux. the equation is from the header, unit is

;erg.cm^-2.s^-1. Not using this one because logCnts became nan

;when img is a minus value.

;logFlux=zp+logCnts-alog10(Texp)

;flux=10^(logFlux)

flux=10.^zp*img/Texp


;calculte the size of pixel in arcsec^2

getrot,head,rot,scale

x=abs(scale[0])

y=abs(scale[1])

arcsec_sq=3600.*3600.*x*y


;change the unit of the flux from erg.cm^-2.s^-1 to Jy.arcsec^-2

flux=flux*10^23/arcsec_sq


;write the result into fits image

writefits,fileprefix+'_unit.fits',flux,head


end
```

A.2 `readimg.pro`

The program in IDL to prepare data for data analysis. The attached is for NGC4254, but all the other galaxies use the same program except the galaxy names are different.

```
;read in convoled images of NGC4254
;no good 70 image avaliable
imgha=readfits('ngc4254_ha_preped_convplw.fits',headerha)
img16=readfits('ngc4254_1.6_starfilt_convplw.fits',header16)
img100=readfits('ngc4254_100_convplw.fits',header100)
img160=readfits('ngc4254_160_convplw.fits', header160)
img250=readfits('ngc4254_250_convplw.fits',header250)
img350=readfits('ngc4254_350_convplw.fits',header350)
img500=readfits('ngc4254_500.fits',header500,exten=1)



;Convert Ha and 1.6 micron data to Jy/arcsec^2
; Ha units changed by program 'change_Ha_unit.pro' under folder
;'Ha_images'.
; 1.6 image is 1Jy/arcsec^2



;Convert 100-160 micron data to Jy/arcsec^2 from their header information
img100=img100/10.24
img160=img160/40.96
;(convert data from Jy/pixel to Jy/arcsec^2)



;Convert 250-500 micron data to Jy/arcsec^2.
;Multiply SPIRE images by colour corrections and divide by beam areas.
```

```
;Numbers got from http://herschel.esac.esa.int/Docs

;/SPIRE/html/spire_om.html#x1-980005.2.7


img250=img250/423*0.98279*0.994

;(divide by 423 arcsec^2/beam to convert the data from

;Jy/beam to Jy/arcsec^2.

; Then multiply the data by 0.98279*0.994(color corrections).)


img350=img350/751*0.98344*0.990

;(Divide the data by 751 arcsec^2/beam to convert the data

;from Jy/beam to Jy/arcsec^2.  The multiply the data by 0.98344*0.990

;(color corrections).)


img500=img500/1587*0.97099*1.003

;(Divide the data by 1587 arcsec^2/beam to convert the data

;from Jy/beam to Jy/arcsec^2.  The multiply the data by 0.97099*1.003

;(color corrections).)




;Identify the background using mask arrays.

regmask, 'ngc4254_ha_back.reg',imgha,maskha, header=headerha

regmask, 'ngc4254_1.6back.reg',img16,mask16, header=header16

regmask, 'ngc4254_160back.reg',img100,mask100, header=header100

regmask, 'ngc4254_160back.reg',img160,mask160, header=header160

regmask, 'ngc4254_spire_back.reg',img250,mask250,header=header250

regmask, 'ngc4254_spire_back.reg',img350,mask350, header=header350

regmask, 'ngc4254_spire_back.reg',img500,mask500, header=header500
```

```
;Subtract the background.

imgha=imgha-median(imgha(where(maskha eq 1)))

img16=img16-median(img16(where(mask16 eq 1)))

img100=img100-median(img100(where(mask100 eq 1)))

img160=img160-median(img160(where(mask160 eq 1)))

img250=img250-median(img250(where(mask250 eq 1)))

img350=img350-median(img350(where(mask350 eq 1)))

img500=img500-median(img500(where(mask500 eq 1)))



;Cut the 250 micron image.  (Don't do this for the other bands.)
hextract,img250,header250,1627,1716,1984,2073



;Match the coordinates of the other images to the 250 micron image.
hastrom,imgha,headerha,header250

hastrom,img16,header16,header250

hastrom,img100,header100,header250

hastrom,img160,header160,header250

hastrom,img350,header350,header250

hastrom,img500,header500,header250



;Rebin the images.
hrebin,imgha,headerha,imghareb,headerhareb,15,15

hrebin,img16,header16,img16reb,header16reb,15,15

hrebin,img100,header100,img100reb,header100reb,15,15

hrebin,img160,header160,img160reb,header160reb,15,15

hrebin,img250,header250,img250reb,header250reb,15,15
```

```
hrebin,img350,header350,img350reb,header350reb,15,15

hrebin,img500,header500,img500reb,header500reb,15,15



;rebinned images

;writefits,'rebha.fits',imghareb,headerhareb

;writefits,'reb16.fits',img16reb,header16reb

;writefits,'reb100.fits',img100reb,header100reb

;writefits,'reb160.fits',img160reb,header160reb

;writefits,'reb250.fits',img250reb,header250reb

;writefits,'reb350.fits',img350reb,header350reb

;writefits,'reb500.fits',img500reb,header500reb



;----------------------------------------



;Measure the background noise.

sdha=stddev([imghareb[0:2,12:14],imghareb[12:14,0:2], $

imghareb[0:2,0:2],imghareb[12:14,12:14]])

sd16=stddev([img16reb[0:2,12:14],img16reb[12:14,0:2], $

img16reb[12:14,12:14]])

;sd70=stddev([img70reb[0:2,0:2],img70reb[12:14,0:2], $

img70reb[12:14,12:14]])

sd100=stddev([img100reb[0:2,12:14],img100reb[12:14,0:2], $

img100reb[0:2,0:2],img100reb[12:14,12:14]])

sd160=stddev([img160reb[0:2,12:14],img160reb[12:14,0:2], $

img160reb[0:2,0:2],img160reb[12:14,12:14]])

sd250=stddev([img250reb[0:2,0:2],img250reb[12:14,0:2],$

img250reb[12:14,12:14]])

sd350=stddev([img350reb[0:2,0:2],img350reb[12:14,0:2],$

img350reb[12:14,12:14]])
```

```
sd500=stddev([img500reb[0:2,0:2],img500reb[12:14,0:2],$

img500reb[12:14,12:14]])


;Remove bad pixels.

;img70reb(3,7)=!values.f_nan

;img70reb(4,5)=!values.f_nan

img500reb(4,6)=!values.f_nan

img500reb(11,7)=!values.f_nan



;Select data that are detected at the 5 sigma level.

w=where(img100reb ge 5*sd100 and img160reb ge 5*sd160 and $

img250reb ge 5*sd250 and img350reb ge 5*sd350,complement=wbad)



save,filename='ngc4254_bindata.dat',img16reb,imghareb,$

img100reb,img160reb,img250reb,img350reb,img500reb,$

sd16,sdha,sd100,sd160,sd250,sd350,sd500,w,wbad


end
```

A.3 plot_T.pro


```
;program to plot planck function with 3 different temperatures.

;In this program , I is Intensity,L is wavelength, T is temperature.



!p.multi=0
```

```
set_plot,'ps'

device,filename='plot_Tlog.ps'

!p.font=0


h=6.626068e-34

c=3e8

k=1.3806503e-23



T=30.

L=findgen(1e6)/1e6

I=(L)^(-5)*1/(exp(h*c/(L*k*T))-1)



plot,L,I,xtitle='Wavelength(meter)',ytitle='Intensity $

(arbitrary)',ystyle=1, /ylog,/xlog , xrange=[1e-6,5e-1], $

YRANGE=[0,1e19]


L=[0.0001, 0.00016, 0.00025, 0.00035, 0.0005]

I=(L)^(-5)*1/(exp(h*c/(L*k*T))-1)

oplot, L,I, psym=6


;xyouts,0.0002,1e18,'T=30K',CHARSIZE = 0.8


T=20

L=findgen(1e6)/1e6

I=L^(-5)*1/(exp(h*c/(L*k*T))-1)

oplot,L,I,linestyle=2


L=[0.0001,0.00016,0.00025, 0.00035, 0.0005]
```

```
I=(L)^(-5)*1/(exp(h*c/(L*k*T))-1)

oplot, L,I, psym=6


;xyouts,0.0002,1e16,'T=20K',CHARSIZE = 0.8


T=10

L=findgen(1e6)/1e6

I=L^(-5)*1/(exp(h*c/(L*k*T))-1)

oplot,L,I,linestyle=1


L=[0.0001,0.00016,0.00025, 0.00035, 0.0005]

I=(L)^(-5)*1/(exp(h*c/(L*k*T))-1)

oplot, L,I, psym=6


;xyouts,0.0002,5e14,'T=10K',CHARSIZE = 0.8


meanings = ['T=30K', 'T=20K', 'T=10K']

lines = [0,2,1]

LEGEND, linestyle=lines, meanings, /right, /top, CHARSIZE = 0.8


!p.font=-1

device,/close

set_plot,'x'




end
```

A.4 `plot_mass.pro`

```
;program to plot planck function with 2 different temperatures

;and one with different mass.

;In this program , F is Intensity,L is wavelength,

;T is temperature, M is mass.



!p.multi=0


set_plot,'ps'

device,filename='plot_mass.ps'

!p.font=0


h=6.626068e-34

c=3e8

k=1.3806503e-23



T=30.

M=1

L=findgen(1e6)/1e6

F=(L)^(-7)*M*1/(exp(h*c/(L*k*T))-1)


plot,L,F,xtitle='log (!9l!N!3)',ytitle='log (I!9!Dl!N!3)',$

ystyle=1, /ylog,/xlog, xrange=[1e-5,1e-2], YRANGE=[1e20,1e27]


;plot,L,F,xtitle='Wavelength(meter)',ytitle='Flux Density $
```

```
(arbitrary)',ystyle=1, /ylog,/xlog , xrange=[1e-5, 1e-2], $
 YRANGE=[1e8,1e11]


L=[0.0001, 0.00016, 0.00025, 0.00035, 0.0005]
F=(L)^(-7)*M*1/(exp(h*c/(L*k*T))-1)
oplot, L,F, psym=6


;xyouts,0.0002,1e18,'T=30K',CHARSIZE = 0.8


T=20
M=1
L=findgen(1e6)/1e6
F=(L)^(-7)*M*1/(exp(h*c/(L*k*T))-1)
oplot,L,F,linestyle=2


L=[0.0001,0.00016,0.00025, 0.00035, 0.0005]
F=(L)^(-7)*M*1/(exp(h*c/(L*k*T))-1)
oplot, L,F, psym=6


;xyouts,0.0002,1e16,'T=20K',CHARSIZE = 0.8


T=20
M=6
L=findgen(1e6)/1e6
F=(L)^(-7)*M*1/(exp(h*c/(L*k*T))-1)
oplot,L,F,linestyle=1


L=[0.0001,0.00016,0.00025, 0.00035, 0.0005]
F=(L)^(-7)*M*1/(exp(h*c/(L*k*T))-1)
oplot, L,F, psym=6
```

```
;xyouts,0.0002,5e14,'T=10K',CHARSIZE = 0.8


meanings = ['T=30K', 'T=20K', 'T=20K (more dust)']

lines = [0,2,1]

LEGEND, linestyle=lines, meanings, /right, /top, CHARSIZE = 0.8


!p.font=-1

device,/close

set_plot,'x'


end
```

A.5 `plot_IRatio30.pro`

```
;program to plot surface brightness(I) ratio(I_1/I_2) $

relation with temperature (T) up to 30 K

;Which is I_1/I_2 against T

;In this program , I_1/I_2 is represented by y; T is t.


!p.multi=0

;!p.multi=[0,2,0]


set_plot,'ps'

device,filename='plot_IRatio30.ps'

!p.font=0
```

```
;w1 is wavelength_1 (lambda1) in mm, w2 is wavelength2_2 (lambda2) in mm


;h=6.626068e-34

;c=3e8

;k=1.3806503e-23

;h*c/k=14.4e-3

;mm=1e-3m

;h*c/k(w1 in 1e-3m)=14.4



t=findgen(31)


w1=0.1

w2=0.16

c=(w2/w1)^7

y=c*(exp(14.4/w2/t)-1)/(exp(14.4/w1/t)-1)

plot,t,y,ystyle=1,xrange=[0,30], yrange=[0,7], $

xtitle='!N!3Temperature (K)',ytitle='!N!3I!9!Dn1!N!3/I!9!Dn2'



w1=0.16

w2=0.25

c=(w2/w1)^7

y=c*(exp(14.4/(w2*t))-1)/(exp(14.4/(w1*t))-1)

oplot,t,y



w1=0.25

w2=0.35

c=(w2/w1)^7
```

```
y=c*(exp(14.4/(w2*t))-1)/(exp(14.4/(w1*t))-1)

oplot,t,y



w1=0.35

w2=0.5

c=(w2/w1)^7

y=c*(exp(14.4/w2/t)-1)/(exp(14.4/w1/t)-1)

oplot,t,y



xyouts,18,1,'!N!3I!D100!9m!3m!N!3/I!D160!9m!3m',CHARSIZE = 0.8

xyouts,15,2.3,'I!D160!9m!3m!N!3/I!D250!9m!3m',CHARSIZE = 0.8

xyouts,13,3.8,'I!D250!9m!3m!N!3/I!D350!9m!3m',CHARSIZE = 0.8

xyouts,11,4.8,'I!D350!9m!3m!N!3/I!D500!9m!3m',CHARSIZE = 0.8



!p.font=-1

device,/close

set_plot,'x'



end
```

A.6   `plot_IRatio300.pro`

```
;program to plot surface brightness(I) ratio(I_1/I_2) $

relation with temperature (T)

;Which is I_1/I_2 against T
```

```
;In this program , I_1/I_2 is represented by y; T is t.


!p.multi=0

;!p.multi=[0,2,0]


set_plot,'ps'

device,filename='plot_IRatio300.ps'

!p.font=0


;w1 is wavelength_1 (lambda1) in mm, w2 is wavelength2_2 $

(lambda2) in mm


w1=0.1

w2=0.16

c=(w2/w1)^7


t=findgen(300)

y=c*(exp(14.4/w2/t)-1)/(exp(14.4/w1/t)-1)

plot,t,y,xtitle='!N!3T (K)',ytitle='!N!3I!9!Dl1!N!3/I!9!Dl2'


w1=0.16

w2=0.25

c=(w2/w1)^7


;t=findgen(30)

y=c*(exp(14.4/w2/t)-1)/(exp(14.4/w1/t)-1)

oplot,t,y


w1=0.25
```

```
w2=0.35
c=(w2/w1)^7


;t=findgen(30)
y=c*(exp(14.4/w2/t)-1)/(exp(14.4/w1/t)-1)
oplot,t,y


w1=0.35
w2=0.5
c=(w2/w1)^7


;t=findgen(30)
y=c*(exp(14.4/w2/t)-1)/(exp(14.4/w1/t)-1)
oplot,t,y



xyouts,210,15.3,'I!D100!9m!3m!N!3/I!D160!9m!3m',CHARSIZE = 0.8
xyouts,170,12.3,'I!D160!9m!3m!N!3/I!D250!9m!3m',CHARSIZE = 0.8
xyouts,130,8.5,'I!D350!9m!3m!N!3/I!D500!9m!3m',CHARSIZE = 0.8
xyouts,100,6.3,'!N!3I!D250!9m!3m!N!3/I!D350!9m!3m',CHARSIZE = 0.8



!p.font=-1
device,/close
set_plot,'x'


end
```

A.7 `plot_kB.pro`

```
;program to plot Intensity I which is planck function with

;absorption opacity Kappa in 3 different temperatures.

;In this program , I is Intensity,L is wavelength, T is temperature.



!p.multi=0


set_plot,'ps'

device,filename='plot_kB.ps'

!p.font=0



h=6.626068e-34

c=3e8

k=1.3806503e-23



T=30.

L=findgen(1e6)/1e6

I=(L)^(-7)*1/(exp(h*c/(L*k*T))-1)


plot,L,I,xtitle='log (!9l!N!3)',ytitle='log (I!9!Dl!N!3)',$

ystyle=1, /ylog,/xlog, xrange=[5e-6,1e-1], YRANGE=[0,1e27]



L=[0.0001, 0.00016, 0.00025, 0.00035, 0.0005]

I=(L)^(-7)*1/(exp(h*c/(L*k*T))-1)
```

```
oplot, L,I, psym=6


;xyouts,0.0002,1e18,'T=30K',CHARSIZE = 0.8


T=20

L=findgen(1e6)/1e6

I=L^(-7)*1/(exp(h*c/(L*k*T))-1)

oplot,L,I,linestyle=2


L=[0.0001,0.00016,0.00025, 0.00035, 0.0005]

I=(L)^(-7)*1/(exp(h*c/(L*k*T))-1)

oplot, L,I, psym=6


;xyouts,0.0002,1e16,'T=20K',CHARSIZE = 0.8


T=10

L=findgen(1e6)/1e6

I=L^(-7)*1/(exp(h*c/(L*k*T))-1)

oplot,L,I,linestyle=1


L=[0.0001,0.00016,0.00025, 0.00035, 0.0005]

I=(L)^(-7)*1/(exp(h*c/(L*k*T))-1)

oplot, L,I, psym=6


;xyouts,0.0002,5e14,'T=10K',CHARSIZE = 0.8


meanings = ['T=30K', 'T=20K', 'T=10K']

lines = [0,2,1]

LEGEND, linestyle=lines, meanings, /right, /top, CHARSIZE = 0.8
```

```
!p.font=-1
device,/close
set_plot,'x'


end
```

A.8 plot_IRatio30nulam.pro

```
;program to plot surface brightness ratio(I_nu (lambda1)/I_nu
; (lambda2) relation with temperature (T) up to 30 K
;Which is I_1/I_2 against T
;In this program , I_1/I_2 is represented by y; T is t.


!p.multi=0
;!p.multi=[0,2,0]


set_plot,'ps'
device,filename='plot_IRatio30nulam.ps'
!p.font=0


;w1 is wavelength_1 (lambda1) in mm,
;w2 is wavelength2_2 (lambda2) in mm


;h=6.626068e-34
;c=3e8
;k=1.3806503e-23
;h*c/k=14.4e-3
```

```
;mm=1e-3m

;h*c/k(w1 in 1e-3m)=14.4



t=findgen(31)


w1=0.1

w2=0.16

c=(w2/w1)^5

y=c*(exp(14.4/w2/t)-1)/(exp(14.4/w1/t)-1)

plot,t,y,ystyle=1,xrange=[0,30], yrange=[0,3.5], $

xtitle='!N!3T (K)',$

ytitle='!N!3I!9!Dn!N!3 (!9l!D1!N!3) / I!9!Dn!N!3 (!9l!D2!N!3)'



w1=0.16

w2=0.25

c=(w2/w1)^5

y=c*(exp(14.4/(w2*t))-1)/(exp(14.4/(w1*t))-1)

oplot,t,y



w1=0.25

w2=0.35

c=(w2/w1)^5

y=c*(exp(14.4/(w2*t))-1)/(exp(14.4/(w1*t))-1)

oplot,t,y



w1=0.35
```

```
w2=0.5

c=(w2/w1)^5

y=c*(exp(14.4/w2/t)-1)/(exp(14.4/w1/t)-1)

oplot,t,y


xyouts,20,0.6,'!N!3I!D100!9m!3m!N!3/I!D160!9m!3m',CHARSIZE = 0.8

xyouts,16,1,'I!D160!9m!3m!N!3/I!D250!9m!3m',CHARSIZE = 0.8

xyouts,13,1.9,'I!D250!9m!3m!N!3/I!D350!9m!3m',CHARSIZE = 0.8

xyouts,12,2.5,'I!D350!9m!3m!N!3/I!D500!9m!3m',CHARSIZE = 0.8



!p.font=-1

device,/close

set_plot,'x'


end
```

A.9 `plot_ha16.pro`

```
;plot of surface brightness ratio against 1.6um and Ha intensity


restore,'ngc4254_bindata.dat'

!p.multi=[0,2,4]

!p.charsize=2

set_plot,'ps'

device,filename='ngc4254_ha16_no500_xy.ps'

device,/encapsul,/cm,xsize=30,ysize=30

!p.font=0
```

```
plot,1e15*imghareb(w),img100reb(w)/img160reb(w), $
  xrange=[0,1.1],yrange=[0.2,1.2], ystyle=1,psym=6,$
   xtitle='I!9!Dn!N!3(H!9a!3)',$
ytitle='I!9!Dn!N!3(100!9m!3m)/I!9!Dn!N!3(160!9m!3m)'
print,'The Ha correlation of 100/160 is:$
',correlate(alog10(imghareb(w)),$
alog10(img100reb(w)/img160reb(w)))


plot,1e4*img16reb(w),img100reb(w)/img160reb(w),$
  xrange=[0,1],yrange=[0.2,1.2], ystyle=1,psym=6,$
 xtitle='I!9!Dn!N!3(1.6!9m!3m)',$
ytitle='I!9!Dn!N!3(100!9m!3m)/I!9!Dn!N!3(160!9m!3m)'
print,'The 1.6 micron correlation of 100/160 is:',$
correlate(img16reb(w),img100reb(w)/img160reb(w))



plot,1e15*imghareb(w),img160reb(w)/img250reb(w),$
   xrange=[0,1.1],yrange=[1.3,2.7], ystyle=1, psym=6,$
  xtitle='I!9!Dn!N!3(H!9a!3)',$
ytitle='I!9!Dn!N!3(160!9m!3m)/I!9!Dn!N!3(250!9m!3m)'
print,'The Ha correlation of 160/250 is:$
', correlate(imghareb(w),img160reb(w)/img250reb(w))


plot,1e4*img16reb(w),img160reb(w)/img250reb(w),$
   xrange=[0,1],yrange=[1.3,2.7], ystyle=1,psym=6,$
  xtitle='I!9!Dn!N!3(1.6!9m!3m)',$
ytitle='I!9!Dn!N!3(160!9m!3m)/!9!Dn!N!3I(250!9m!3m)'
print,'The 1.6 micron correlation of 160/250 is:',$
correlate(img16reb(w),img160reb(w)/img250reb(w))
```

```
;yrange=[2,3],ystyle=1,


plot,1e15*imghareb(w),img250reb(w)/img350reb(w),$
  xrange=[0,1.1],yrange=[2.1,2.8], ystyle=1, psym=6,$
  xtitle='I!9!Dn!N!3(H!9a!3)',$
ytitle='I!9!Dn!N!3(250!9m!3m)/I!9!Dn!N!3(350!9m!3m)'
print,'The Ha correlation of 250/350 is:',$
correlate(imghareb(w),img250reb(w)/img350reb(w))


plot,1e4*img16reb(w),img250reb(w)/img350reb(w),$
  xrange=[0,1],yrange=[2.1,2.8], ystyle=1,psym=6,$
  xtitle='I!9!Dn!N!3(1.6!9m!3m)',$
ytitle='I!9!Dn!N!3(250!9m!3m)/!9!Dn!N!3I(350!9m!3m)'
print,'The 1.6 micron correlation of 250/350 is:',$
correlate(img16reb(w),img250reb(w)/img350reb(w))



plot,1e15*imghareb(w),img350reb(w)/img500reb(w),$
   xrange=[0,1.1],yrange=[2.5,3.2], ystyle=1, psym=6,$
   xtitle='I!9!Dn!N!3(H!9a!3)',$
ytitle='I!9!Dn!N!3(350!9m!3m)/I!9!Dn!N!3(500!9m!3m)'
print,'The Ha correlation of 350/500 is:', $
correlate(imghareb(w),img350reb(w)/img500reb(w))


plot,1e4*img16reb(w),img350reb(w)/img500reb(w),$
 xrange=[0,1],yrange=[2.5,3.2], ystyle=1, psym=6,$
 xtitle='I!9!Dn!N!3(1.6!9m!3m)',$
ytitle='I!9!Dn!N!3(350!9m!3m)/I!9!Dn!N!3(500!9m!3m)'
print,'The 1.6 micron correlation of 350/500 is:',$
```

```
correlate(img16reb(w),img350reb(w)/img500reb(w))
```

```
!p.font=-1
device,/close
set_plot,'x'
!p.charsize=0
```

```
end
```

A.10 3plot_ha16xylog.pro

```
;plot of surface brightness ratio against 1.6um and
;Ha intensity in log
```

```
restore,'ngc4254_bindata.dat'
!p.multi=[0,2,4]
!p.charsize=2
set_plot,'ps'
device,filename='ngc4254_ha16_no500_xylog.ps'
device,/encapsul,/cm,xsize=20,ysize=26
!p.font=0
```

```
plot,alog10(imghareb(w)),alog10(img100reb(w)/img160reb(w)), $
   xrange=[-16.5,-14.5],yrange=[-0.6,0.2],ystyle=1,psym=6,$
   xtitle='I!9!Dn!N!3(H!9a!3)',$
```

```
ytitle='I!9!Dn!N!3(100!9m!3m)/I!9!Dn!N!3(160!9m!3m)
```

```
;xyouts,2e-17,0.2,"A label"
print,'The Ha correlation of 100/160 is:$
',correlate(alog10(imghareb(w)),$
alog10(img100reb(w)/img160reb(w)))
```

```
plot,alog10(img16reb(w)),alog10(img100reb(w)/img160reb(w)),$
  xrange=[-6,-3.5],yrange=[-0.6,0.2], ystyle=1,psym=6,$
 xtitle='I!9!Dn!N!3(1.6!9m!3m)',$
ytitle='I!9!Dn!N!3(100!9m!3m)/I!9!Dn!N!3(160!9m!3m)'
print,'The 1.6 micron correlation of 100/160 is:',$
correlate(alog10(img16reb(w)),alog10(img100reb(w)/img160reb(w)))
```

```
plot,alog10(imghareb(w)),alog10(img160reb(w)/img250reb(w)),$
   xrange=[-16.5,-14.5],yrange=[0.1,0.5], psym=6,$
  xtitle='I!9!Dn!N!3(H!9a!3)',$
ytitle='I!9!Dn!N!3(160!9m!3m)/I!9!Dn!N!3(250!9m!3m)'
print,'The Ha correlation of 160/250 is:', $
correlate(alog10(imghareb(w)),alog10(img160reb(w)/img250reb(w)))
```

```
plot, alog10(img16reb(w)),alog10(img160reb(w)/img250reb(w)),$
   xrange=[-6,-3.5],yrange=[0.1,0.5], ystyle=1,psym=6,$
  xtitle='I!9!Dn!N!3(1.6!9m!3m)',$
ytitle='I!9!Dn!N!3(160!9m!3m)/!9!Dn!N!3I(250!9m!3m)'
print,'The 1.6 micron correlation of 160/250 is:',$
correlate(alog10(img16reb(w)),alog10(img160reb(w)/img250reb(w)))
;yrange=[2,3],ystyle=1,
```

```
plot,alog10(imghareb(w)),alog10(img250reb(w)/img350reb(w)),$
  xrange=[-16.5,-14.5],yrange=[0.3,0.45],psym=6,$
  xtitle='I!9!Dn!N!3(H!9a!3)',$
ytitle='I!9!Dn!N!3(250!9m!3m)/I!9!Dn!N!3(350!9m!3m)'
print,'The Ha correlation of 250/350 is:',$
correlate(alog10(imghareb(w)),alog10(img250reb(w)/img350reb(w)))


plot,alog10(img16reb(w)),alog10(img250reb(w)/img350reb(w)),$
  xrange=[-6,-3.5],yrange=[0.3,0.45],ystyle=1,psym=6,$
  xtitle='I!9!Dn!N!3(1.6!9m!3m)',$
ytitle='I!9!Dn!N!3(250!9m!3m)/!9!Dn!N!3I(350!9m!3m)'
print,'The 1.6 micron correlation of 250/350 is:',$
correlate(alog10(img16reb(w)),alog10(img250reb(w)/img350reb(w)))



plot,alog10(imghareb(w)),alog10(img350reb(w)/img500reb(w)),$
   xrange=[-16.5,-14.5],yrange=[0.4,0.5], psym=6,$
   xtitle='I!9!Dn!N!3(H!9a!3)',$
ytitle='I!9!Dn!N!3(350!9m!3m)/I!9!Dn!N!3(500!9m!3m)'
print,'The Ha correlation of 350/500 is:', $
correlate(alog10(imghareb(w)),alog10(img350reb(w)/img500reb(w)))


plot,alog10(img16reb(w)),alog10(img350reb(w)/img500reb(w)),$
  xrange=[-6,-3.5],yrange=[0.4,0.5],ystyle=1, psym=6,$
 xtitle='I!9!Dn!N!3(1.6!9m!3m)',$
ytitle='I!9!Dn!N!3(350!9m!3m)/I!9!Dn!N!3(500!9m!3m)'
print,'The 1.6 micron correlation of 350/500 is:', $
correlate(alog10(img16reb(w)),alog10(img350reb(w)/img500reb(w)))
```

```
;Result,

;The Ha correlation of 100/160 is:       0.86244606

;The Ha correlation of 160/250 is:       0.89287391

;The Ha correlation of 250/350 is:       0.93679424

;The Ha correlation of 350/500 is:       0.85096116

;The 1.6 micron correlation of 100/160 is:       0.74344143

;The 1.6 micron correlation of 160/250 is:       0.73351112

;The 1.6 micron correlation of 250/350 is:       0.89931698

;The 1.6 micron correlation of 350/500 is:       0.86246018



!p.font=-1
device,/close
set_plot,'x'
!p.charsize=0


end
```

A.11 change_coor.pro

```
;This program correct the corrodinate system of 160 image.
;Because the coordinate system of the 160 and 250 are set differently,
; so it it need to be corrected.
;This program is also used to correct the 100 image of
;the NGC4321 and 100 and 160 of NGC4254.


;restore,'ngc4321_bindata.dat'


;read in convoled images of NGC4321
img160=readfits('ngc4321_160_convplw.fits', header160)
img250=readfits('ngc4321_250_convplw.fits',header250)



;change the 160 y axis coordinate system from '1640.5'
;to match the 250 image,
;the new number for CRPIX2 is found after testing with the ratio plot.
sxaddpar, header160, 'CRPIX2', 1639.9



img160=img160/40.96
img250=img250/423*0.98279*0.994
regmask, 'ngc4321_160back.reg',img160,mask160, header=header160
regmask, 'ngc4321_250back.reg',img250,mask250, header=header250
img160=img160-median(img160(where(mask160 eq 1)))
img250=img250-median(img250(where(mask250 eq 1)))
sdimg160=stddev(img160(where(mask160 eq 1)))
sdimg250=stddev(img250(where(mask250 eq 1)))
```

```
;Cut the 250 micron image in the order of x0,x1,y0,y1 in physicsal unit.
; (Don't do this for the other bands.)
hextract,img250,header250,1038,1127,2820,2933


hastrom,img160,header160,header250



regmask,'ngc4321_opticaldisk.reg',img250,maskdisc,header=header250


rat=img160/img250
rat(where(maskdisc eq 0 or img160 lt 5*sdimg160 or $
 img250 lt 5.*sdimg250))=!values.f_nan
writefits,'ngc4321_rat_160_250_new4.fits',rat,header250



;hrebin,img160,header160,img160reb,header160reb,15,19
;hrebin,img250,header250,img250reb,header250reb,15,19

;print,'The 1.6 micron correlation of 100/160 is:',$
correlate(alog10(img16reb(w)),alog10(img100reb(w)/img160reb(w)))
;print,'The Ha correlation of 160/250 is:', $
 correlate(alog10(imghareb(w)),$
alog10(img160reb(w)/img250reb(w)))



end
```

A.12 `readimg_plot.pro`

```
;read in convoled images of NGC4321


imgha=readfits('ngc4321_ha_preped_convplw.fits',headerha)

img16=readfits('ngc4321_1.6_starfilt_convplw.fits',header16)

img100=readfits('ngc4321_100_convplw.fits',header100)

img160=readfits('ngc4321_160_convplw.fits', header160)

img250=readfits('ngc4321_250_convplw.fits',header250)

img350=readfits('ngc4321_350_convplw.fits',header350)

img500=readfits('ngc4321_500.fits',header500,exten=1)


;sxaddpar, header160, 'CRPIX2', 1639.9


;Convert Ha and 1.6 micron data to Jy/arcsec^2

; Ha units changed by program 'change_Ha_unit.pro' under folder

;'Ha_images'.

; 1.6 image is 1Jy/arcsec^2



;Convert 70-160 micron data to Jy/arcsec^2 from their header

;information

;img70=img70*2.35e-5/0.901

;(In addition to converting the data from MJy/sr to

;Jy/arcsec^2, divide the data by 0.901(colour correction). )

img100=img100/10.24

img160=img160/40.96

;(convert data from Jy/pixel to Jy/arcsec^2)
```

```
;Convert 250-500 micron data to Jy/arcsec^2.Multiply SPIRE images

;by colour corrections and divide by beam areas.

img250=img250/423*0.98279*0.994

;(423beam/arcsec^2 to convert the data from Jy/beam to Jy/arcsec^2.

; The multiply the data by 0.98279*0.994(color corrections).)


img350=img350/751*0.98344*0.990

;(Divide the data by 751 beam/arcsec^2 to convert the data

;from Jy/beam to Jy/arcsec^2.  The multiply the data by 0.98344*0.990

;(color corrections).)


img500=img500/1587*0.97099*1.003

;(Divide the data by 1587 beam/arcsec^2 to convert the data

;from Jy/beam to Jy/arcsec^2.  The multiply the data by 0.97099*1.003

;(color corrections).)



;Identify the background using mask arrays.

regmask, 'ngc4321_ha_back.reg',imgha,maskha, header=headerha

regmask, 'ngc4321_1.6back.reg',img16,mask16, header=header16

regmask, 'ngc4321_100back.reg',img100,mask100, header=header100

regmask, 'ngc4321_160back.reg',img160,mask160, header=header160

regmask, 'ngc4321_250back.reg',img250,mask250, header=header250

regmask, 'ngc4321_350back.reg',img350,mask350, header=header350

regmask, 'ngc4321_500back.reg',img500,mask500, header=header500
```

```
;Subtract the background.

imgha=imgha-median(imgha(where(maskha eq 1)))

img16=img16-median(img16(where(mask16 eq 1)))

img100=img100-median(img100(where(mask100 eq 1)))

img160=img160-median(img160(where(mask160 eq 1)))

img250=img250-median(img250(where(mask250 eq 1)))

img350=img350-median(img350(where(mask350 eq 1)))

img500=img500-median(img500(where(mask500 eq 1)))




;Cut the 250 micron image in the order of x0,x1,y0,y1 in

;physicsal unit.

; (Don't do this for the other bands.)

hextract,img250,header250,1038,1127,2820,2933




;Match the coordinates of the other images to the 250 micron image.

hastrom,imgha,headerha,header250

hastrom,img16,header16,header250

hastrom,img100,header100,header250

hastrom,img160,header160,header250

hastrom,img350,header350,header250

hastrom,img500,header500,header250




;Rebin the images.

hrebin,imgha,headerha,imghareb,headerhareb,15,19
```

```
hrebin,img16,header16,img16reb,header16reb,15,19

;hrebin,img70,header70,img70reb,header70reb,15,19

hrebin,img100,header100,img100reb,header100reb,15,19

hrebin,img160,header160,img160reb,header160reb,15,19

hrebin,img250,header250,img250reb,header250reb,15,19

hrebin,img350,header350,img350reb,header350reb,15,19

hrebin,img500,header500,img500reb,header500reb,15,19




;rebinned images

;writefits,'rebha.fits',imghareb,headerhareb

;writefits,'reb70.fits',img70reb,header70reb

;writefits,'reb100.fits',img100reb,header100reb

;writefits,'reb160.fits',img160reb,header160reb

;writefits,'reb250.fits',img250reb,header250reb

;writefits,'reb350.fits',img350reb,header350reb

;writefits,'reb500.fits',img500reb,header500reb




;-----------------------------------------------------------

;Measure the background noise.

sdha=stddev([imghareb[0:2,16:18],imghareb[12:14,0:2], $

imghareb[0:2,0:2],imghareb[12:14,16:18]])

sd16=stddev([img16reb[0:2,16:18],img16reb[0:2,0:2], $

img16reb[12:14,0:2]])

;sd70=stddev([img70reb[0:2,0:2],img70reb[12:14,0:2], $

img70reb[12:14,16:18]])

sd100=stddev([img100reb[0:2,16:18],img100reb[12:14,0:2], $

img100reb[0:2,0:2],img100reb[12:14,16:18]])

sd160=stddev([img160reb[0:2,16:18],img160reb[0:2,0:2], $

img160reb[12:14,16:18]])
```

```
sd250=stddev([img250reb[0:2,0:2],img250reb[12:14,0:2], $
img250reb[12:14,16:18]])
sd350=stddev([img350reb[0:2,0:2],img350reb[12:14,0:2], $
img350reb[12:14,16:18]])
sd500=stddev([img500reb[0:2,0:2],img500reb[12:14,0:2], $
img500reb[12:14,16:18]])


;Remove bad pixels.
;for example:img70reb(3,7)=!values.f_nan
img160reb(6,10)=!values.f_nan
img160reb(7,10)=!values.f_nan


;Select data that are detected at the 5 sigma level.
w=where(img100reb ge 5*sd100 and img160reb ge 5*sd160 and $
img250reb ge 5*sd250 and img350reb ge 5*sd350,complement=wbad)




save,filename='ngc4321_bindata.dat',w,img16reb,imghareb,$
img100reb,img160reb,img250reb,img350reb,img500reb,$
sd16,sdha,sd100,sd160,sd250,sd350,sd500


;restore,'ngc4321_bindata.dat'


!p.multi=[0,2,4]
!p.charsize=2
set_plot,'ps'
device,filename='ngc4321_ha16_no500_xylog_old.ps'
device,/encapsul,/cm,xsize=30,ysize=26
!p.font=0
```

```
plot,alog10(imghareb(w)),alog10(img100reb(w)/img160reb(w)), $
   xrange=[-16.5,-14.5],yrange=[-0.7,0.2],ystyle=1,psym=6,$
   xtitle='I!9!Dn!N!3(H!9a!3)', $
ytitle='I!9!Dn!N!3(100!9m!3m)/I!9!Dn!N!3(160!9m!3m)
print,'The Ha correlation of 100/160 is:',$
correlate(alog10(imghareb(w)),alog10(img100reb(w)/img160reb(w)))


plot,alog10(img16reb(w)),alog10(img100reb(w)/img160reb(w)),$
  xrange=[-5.5,-3.5],yrange=[-0.7,0.2], ystyle=1,psym=6,$
 xtitle='I!9!Dn!N!3(1.6!9m!3m)', $
ytitle='I!9!Dn!N!3(100!9m!3m)/I!9!Dn!N!3(160!9m!3m)'
print,'The 1.6 micron correlation of 100/160 is:',$
correlate(alog10(img16reb(w)),alog10(img100reb(w)/img160reb(w)))



plot,alog10(imghareb(w)),alog10(img160reb(w)/img250reb(w)),$
   xrange=[-16.5,-14.5],yrange=[-0.1,0.4], psym=6,$
  xtitle='I!9!Dn!N!3(H!9a!3)', $
ytitle='I!9!Dn!N!3(160!9m!3m)/I!9!Dn!N!3(250!9m!3m)'
print,'The Ha correlation of 160/250 is:', $
correlate(alog10(imghareb(w)),alog10(img160reb(w)/img250reb(w)))


plot, alog10(img16reb(w)),alog10(img160reb(w)/img250reb(w)),$
   xrange=[-5.5,-3.5],yrange=[-0.1,0.4], ystyle=1,psym=6,$
  xtitle='I!9!Dn!N!3(1.6!9m!3m)', $
ytitle='I!9!Dn!N!3(160!9m!3m)/!9!Dn!N!3I(250!9m!3m)'
print,'The 1.6 micron correlation of 160/250 is:',$
correlate(alog10(img16reb(w)),alog10(img160reb(w)/img250reb(w)))
```

```
;yrange=[2,3],ystyle=1,


plot,alog10(imghareb(w)),alog10(img250reb(w)/img350reb(w)),$
   xrange=[-16.5,-14.5],yrange=[0.34,0.42],psym=6,$
   xtitle='I!9!Dn!N!3(H!9a!3)', $
ytitle='I!9!Dn!N!3(250!9m!3m)/I!9!Dn!N!3(350!9m!3m)'
print,'The Ha correlation of 250/350 is:',$
correlate(alog10(imghareb(w)),alog10(img250reb(w)/img350reb(w)))


plot,alog10(img16reb(w)),alog10(img250reb(w)/img350reb(w)),$
   xrange=[-5.5,-3.5],yrange=[0.34,0.42],ystyle=1,psym=6,$
   xtitle='I!9!Dn!N!3(1.6!9m!3m)', $
ytitle='I!9!Dn!N!3(250!9m!3m)/!9!Dn!N!3I(350!9m!3m)'
print,'The 1.6 micron correlation of 250/350 is:',$
correlate(alog10(img16reb(w)),alog10(img250reb(w)/img350reb(w)))



plot,alog10(imghareb(w)),alog10(img350reb(w)/img500reb(w)),$
    xrange=[-16.5,-14.5],yrange=[0.4,0.5], psym=6,$
    xtitle='I!9!Dn!N!3(H!9a!3)', $
ytitle='I!9!Dn!N!3(350!9m!3m)/I!9!Dn!N!3(500!9m!3m)'
print,'The Ha correlation of 350/500 is:', $
correlate(alog10(imghareb(w)),alog10(img350reb(w)/img500reb(w)))


plot,alog10(img16reb(w)),alog10(img350reb(w)/img500reb(w)),$
   xrange=[-5.5,-3.5],yrange=[0.4,0.5],ystyle=1, psym=6,$
 xtitle='I!9!Dn!N!3(1.6!9m!3m)', $
ytitle='I!9!Dn!N!3(350!9m!3m)/I!9!Dn!N!3(500!9m!3m)'
print,'The 1.6 micron correlation of 350/500 is:', $
```

```
correlate(alog10(img16reb(w)),alog10(img350reb(w)/img500reb(w)))



;Result,

;The Ha correlation of 100/160 is:      0.87522825

;The 1.6 micron correlation of 100/160 is:      0.87133497

;The Ha correlation of 160/250 is:      0.39124683

;The 1.6 micron correlation of 160/250 is:      0.18767608

;The Ha correlation of 250/350 is:      0.91004942

;The 1.6 micron correlation of 250/350 is:      0.89392249

;The Ha correlation of 350/500 is:      0.71539734

;The 1.6 micron correlation of 350/500 is:      0.76301710



; with 160 2 pixels taken out

;The Ha correlation of 100/160 is:      0.89576209

;The 1.6 micron correlation of 100/160 is:      0.86959832

;The Ha correlation of 160/250 is:      0.60992531

;The 1.6 micron correlation of 160/250 is:      0.44771146

;The Ha correlation of 250/350 is:      0.91844338

;The 1.6 micron correlation of 250/350 is:      0.89075586

;The Ha correlation of 350/500 is:      0.71412248

;The 1.6 micron correlation of 350/500 is:      0.75795026


;With 160 coordinate modified and with 160 2 pixels taken out

;The Ha correlation of 100/160 is:      0.88805578

;The 1.6 micron correlation of 100/160 is:      0.84372171

;The Ha correlation of 160/250 is:      0.57940014

;The 1.6 micron correlation of 160/250 is:      0.47565488

;The Ha correlation of 250/350 is:      0.91844338
```

```
;The 1.6 micron correlation of 250/350 is:      0.89075586

;The Ha correlation of 350/500 is:      0.71412248

;The 1.6 micron correlation of 350/500 is:      0.75795026




!p.font=-1

device,/close

set_plot,'x'

!p.charsize=0




end
```

A.13   why_log.pro

```
;program to plot log of temperature with log of surface

;brightness ratio(I_1/I_2) from 10k to 40 K

;Which is log(T) against log(I_1/I_2)

;In this program , log(I_1/I_2) is represented by y; log(T) is t.


!p.multi=0

;!p.multi=[0,2,0]


set_plot,'ps'

device,filename='why_log.ps'

!p.font=0
```

```
;w1 is wavelength_1 (lambda1) in mm, w2 is wavelength2_2

;(lambda2) in mm


;h=6.626068e-34

;c=3e8

;k=1.3806503e-23

;h*c/k=14.4e-3

;mm=1e-3m

;h*c/k(w1 in 1e-3m)=14.4



t=findgen(31)+10


w1=0.1

w2=0.16

c=(w2/w1)^5

y=alog10(c*(exp(14.4/w2/t)-1)/(exp(14.4/w1/t)-1))

plot,y,alog10(t),ystyle=1, ytitle='!N!3log(T)',$

xtitle='!N!3log(I!9!Dn!N!3 (!9l!D1!N!3) / I!9!Dn!N!3 (!9l!D2!N!3))'


;xrange=[0,33], yrange=[-1.5,1.5],


w1=0.16

w2=0.25

c=(w2/w1)^5

y=alog10(c*(exp(14.4/(w2*t))-1)/(exp(14.4/(w1*t))-1))

oplot,y,alog10(t)



w1=0.25
```

```
w2=0.35

c=(w2/w1)^5

y=alog10(c*(exp(14.4/(w2*t))-1)/(exp(14.4/(w1*t))-1))

oplot,y,alog10(t)




w1=0.35

w2=0.5

c=(w2/w1)^5

y=alog10(c*(exp(14.4/w2/t)-1)/(exp(14.4/w1/t)-1))

oplot,y,alog10(t)


xyouts,-0.8,1.2,'!N!3I!D100!9m!3m!N!3/I!D160!9m!3m',CHARSIZE = 0.8

xyouts,-0.4,1.1,'I!D160!9m!3m!N!3/I!D250!9m!3m',CHARSIZE = 0.8

xyouts,-0.15,1.05,'I!D250!9m!3m!N!3/I!D350!9m!3m',CHARSIZE = 0.8

xyouts,0.26,1.02,'I!D350!9m!3m!N!3/I!D500!9m!3m',CHARSIZE = 0.8



!p.font=-1

device,/close

set_plot,'x'


end
```

A.14 readimg_RatioImg.pro

```
;read in convoled images of NGC4254

;no good 70 image avaliable

imgha=readfits('ngc4254_ha_preped_convplw.fits',headerha)
```

```
img16=readfits('ngc4254_1.6_starfilt_convplw.fits',header16)

img100=readfits('ngc4254_100_convplw.fits',header100)

img160=readfits('ngc4254_160_convplw.fits', header160)

img250=readfits('ngc4254_250_convplw.fits',header250)

img350=readfits('ngc4254_350_convplw.fits',header350)

img500=readfits('ngc4254_500.fits',header500,exten=1)



;Convert Ha and 1.6 micron data to Jy/arcsec^2

; Waiting for Ha image units

; 1.6 image is 1Jy/arcsec^2



;Convert 100-160 micron data to Jy/arcsec^2 from their

;header information

img100=img100/10.24

img160=img160/40.96

;(convert data from Jy/pixel to Jy/arcsec^2)



;Convert 250-500 micron data to Jy/arcsec^2.Multiply SPIRE images

;by colour corrections and divide by beam areas.

img250=img250/423*0.98279*0.994

;(423beam/arcsec^2 to convert the data from Jy/beam to Jy/arcsec^2.

; The multiply the data by 0.98279*0.994(color corrections).)



img350=img350/751*0.98344*0.990

;(Divide the data by 751 beam/arcsec^2 to convert the data

;from Jy/beam to Jy/arcsec^2.

;The multiply the data by 0.98344*0.990
```

```
;(color corrections).)


img500=img500/1587*0.97099*1.003

;(Divide the data by 1587 beam/arcsec^2 to convert the data

;from Jy/beam to Jy/arcsec^2.

;The multiply the data by 0.97099*1.003

;(color corrections).)




;Identify the background using mask arrays.

regmask, 'ngc4254_ha_back.reg',imgha,maskha, header=headerha

regmask, 'ngc4254_1.6back.reg',img16,mask16, header=header16

regmask, 'ngc4254_160back.reg',img100,mask100, header=header100

regmask, 'ngc4254_160back.reg',img160,mask160, header=header160

regmask, 'ngc4254_spire_back.reg',img250,mask250,header=header250

regmask, 'ngc4254_spire_back.reg',img350,mask350, header=header350

regmask, 'ngc4254_spire_back.reg',img500,mask500, header=header500




;Subtract the background.

imgha=imgha-median(imgha(where(maskha eq 1)))

img16=img16-median(img16(where(mask16 eq 1)))

img100=img100-median(img100(where(mask100 eq 1)))

img160=img160-median(img160(where(mask160 eq 1)))

img250=img250-median(img250(where(mask250 eq 1)))

img350=img350-median(img350(where(mask350 eq 1)))

img500=img500-median(img500(where(mask500 eq 1)))
```

```
;Measure the noise in background regions for creating images.

sdimgha=stddev(imgha(where(maskha eq 1)))

sdimg16=stddev(img16(where(mask16 eq 1)))

sdimg100=stddev(img100(where(mask100 eq 1)))

sdimg160=stddev(img160(where(mask160 eq 1)))

sdimg250=stddev(img250(where(mask250 eq 1)))

sdimg350=stddev(img350(where(mask350 eq 1)))

sdimg500=stddev(img500(where(mask500 eq 1)))



;Cut the 250 micron image.  (Don't do this for the other bands.)

hextract,img250,header250,1627,1716,1984,2073



;Match the coordinates of the other images to the 250

;micron image.

hastrom,imgha,headerha,header250

hastrom,img16,header16,header250

hastrom,img100,header100,header250

hastrom,img160,header160,header250

hastrom,img350,header350,header250

hastrom,img500,header500,header250



;Make net Ha and 1.6 image and ratio images within the

;optical disk and the background also set to zero.


regmask,'ngc4254_opticaldisk.reg',img250,maskdisc,header=header250


imgha(where(maskdisc eq 0 or imgha lt 5*sdimgha))=!values.f_nan
```

```
writefits,'ngc4254_net_ha.fits',imgha, header250


img16(where(maskdisc eq 0 or img16 lt 5*sdimg16))=!values.f_nan
writefits,'ngc4254_net_16.fits',img16, header250


rat=img100/img160
rat(where(maskdisc eq 0 or img100 lt 5*sdimg100 or $
img160 lt 5.*sdimg160))=!values.f_nan
writefits,'ngc4254_rat_100_160.fits',rat,header250


rat=img160/img250
rat(where(maskdisc eq 0 or img160 lt 5*sdimg160 or $
img250 lt 5.*sdimg250))=!values.f_nan
writefits,'ngc4254_rat_160_250.fits',rat,header250


rat=img250/img350
rat(where(maskdisc eq 0 or img250 lt 5*sdimg250 or $
img350 lt 5.*sdimg350))=!values.f_nan
writefits,'ngc4254_rat_250_350.fits',rat,header250


rat=img350/img500
rat(where(maskdisc eq 0 or img350 lt 5*sdimg350 or $
img500 lt 5.*sdimg500))=!values.f_nan
writefits,'ngc4254_rat_350_500.fits',rat,header250


end
```

A.15 `plot_kernel.pro`

```
;plot 6 kernels for HA, 1.6, 100,160, 250 and 350.



set_plot,'ps'

device,filename='kernel_plots.ps',/color

!p.font=0


;Read in the data.

imgorig=readfits('ngc4254_ha_preped.fits',header250)



;convolution kernel for HA to PLW.

getrot,header250,rot,scale

scale=abs(scale(0))*3600.

kernel=fltarr(301,301)

xymatrix,kernel,ix,iy

r=((ix-150)^2+(iy-150)^2)^0.5*scale

kernel=exp(-r^2/2./((calcspirefwhm('PLW',scale)/2.35)^2- $

(2.4/2.35)^2))

kernel/=total(kernel)

plot, findgen(151)*scale,kernel(150, 150:300)/kernel(150,150),$

xrange=[0,60], ytitle='Normalised Kernel Function',$

        xtitle='Radius (arcsec)'



;convolution kernel 1.6 to PLW.
```

```
scale=1

r=((ix-150)^2+(iy-150)^2)^0.5*scale

kernel=exp(-r^2/2./((calcspirefwhm('PLW',scale)/2.35)^2- $

(2.5/2.35)^2))

kernel/=total(kernel)

tvlct,[[255],[255],[0]],1

;oplot,indgen(151)*scale,kernel(150, 150:300)/kernel(150,150),

;color=1




;convolution kernel for 100 and 160 micron image.

kernel=readfits('kernel_pacs100fast_to_plw_3.2arcsec.fits')

kernel/=total(kernel)

tvlct,[[255],[0],[0]],1

;1=red

oplot, findgen(41)*3.2,kernel(40, 40:80)/kernel(40,40),color=1

kernel=readfits('kernel_pacs160fast_to_plw_6.4arcsec.fits')

kernel/=total(kernel)

tvlct,[[0],[255],[0]],2

;2=green

oplot, findgen(31)*6.4,kernel(30, 30:60)/kernel(30,30),color=2




;convolution kernel for PSW to PLW.

scale=6

r=((ix-150)^2+(iy-150)^2)^0.5*scale

kernel=exp(-r^2/2./((35.5/2.35)^2-(18.2/2.35)^2))

kernel/=total(kernel)

tvlct,[[0],[0],[255]],3

;3=blue
```

```
oplot,indgen(151)*scale,kernel(150, 150:300)/kernel(150,150), $
color=3


;convolution kernel for PMW to PLW.
scale=8
r=((ix-150)^2+(iy-150)^2)^0.5*scale
kernel=exp(-r^2/2./((35.5/2.35)^2-(24.5/2.35)^2))
kernel/=total(kernel)
tvlct,[[0],[255],[255]],4
;4=cyan
oplot,indgen(151)*scale,kernel(150, 150:300)/kernel(150,150), $
color=4


axis,xaxis=0,xrange=[0,60]


!p.font=-1
device,/close
set_plot,'x'


end
```

A.16 bin_rat.pro

```
;read in convoled images of NGC4254
;no good 70 image avaliable


img250=readfits('ngc4254_250_convplw.fits',header250)
img350=readfits('ngc4254_350_convplw.fits',header350)
img500=readfits('ngc4254_500.fits',header500,exten=1)
```

```
;Convert 250-500 micron data to Jy/arcsec^2.Multiply SPIRE images

;by colour corrections and divide by beam areas.

img250=img250/423*0.98279*0.994

;(423beam/arcsec^2 to convert the data from Jy/beam to Jy/arcsec^2.

; The multiply the data by 0.98279*0.994(color corrections).)


img350=img350/751*0.98344*0.990

;(Divide the data by 751 beam/arcsec^2 to convert the data

;from Jy/beam to Jy/arcsec^2.

;The multiply the data by 0.98344*0.990

;(color corrections).)


img500=img500/1587*0.97099*1.003

;(Divide the data by 1587 beam/arcsec^2 to convert the data

;from Jy/beam to Jy/arcsec^2.

;The multiply the data by 0.97099*1.003

;(color corrections).)


;Identify the background using mask arrays.


regmask, 'ngc4254_spire_back.reg',img250,mask250,header=header250

regmask, 'ngc4254_spire_back.reg',img350,mask350, header=header350

regmask, 'ngc4254_spire_back.reg',img500,mask500, header=header500


;Subtract the background.


img250=img250-median(img250(where(mask250 eq 1)))

img350=img350-median(img350(where(mask350 eq 1)))

img500=img500-median(img500(where(mask500 eq 1)))
```

```
;Measure the noise in background regions for creating images.


sdimg250=stddev(img250(where(mask250 eq 1)))

sdimg350=stddev(img350(where(mask350 eq 1)))

sdimg500=stddev(img500(where(mask500 eq 1)))



;Cut the 250 micron image.  (Don't do this for the other bands.)

hextract,img250,header250,1627,1716,1984,2073



;Match the coordinates of the other images to the 250 micron image.


hastrom,img350,header350,header250

hastrom,img500,header500,header250


hrebin,img250,header250,img250reb,header250reb,15,15

hrebin,img350,header350,img350reb,header350reb,15,15

hrebin,img500,header500,img500reb,header500reb,15,15



regmask,'ngc4254_opticaldisk.reg',img350reb,maskdisc, $

header=header350reb


;img250reb=where(maskdisc eq 0)

;img350reb=where(maskdisc eq 0)

;img500reb=where(maskdisc eq 0)


;Make net Ha and 1.6 image and ratio images within the optical disk and
```

```
;the background also set to zero.



rat=img350reb/img500reb

;rat(where(maskdisc eq 0))=!values.f_nan


rat(where(maskdisc eq 0 or img350reb lt 5.*sdimg350 or $

img500reb lt 5.*sdimg500))=!values.f_nan


;maskdisc eq 0 or


writefits,'bin_rat_350_500.fits',alog10(rat),header250reb


end
```

A.17 3plot_350_500.pro

```
;plot of 350/500 ratio against 1.6um in log before and after

;the bad data got removed


!p.multi=0

!p.charsize=2

set_plot,'ps'

device,filename='ngc4254_350500_xylog1.ps'

device,/encapsul,/cm,xsize=30,ysize=26

!p.font=0
```

```
;restore,'ngc4254_bindata.dat'

;(the data group after bad data being removed)

;plot,alog10(img16reb(w)),alog10(img350reb(w)/img500reb(w)),$

;  xrange=[-6,-3.5],yrange=[0.4,0.5],ystyle=1, psym=6,$

; xtitle='log[I!9!Dn!N!3(1.6!9m!3m)]',$

ytitle='log[I!9!Dn!N!3(350!9m!3m)/I!9!Dn!N!3(500!9m!3m)]'



restore,'ngc4254_bindata2.dat' $

(the data group before bad data being removed)

plot,alog10(img16reb(w2)),alog10(img350reb(w2)/img500reb(w2)),$

  xrange=[-6,-3.5],yrange=[0.4,0.5],ystyle=1, psym=6,$

   xtitle='log[I!9!Dn!N!3(1.6!9m!3m)]',$

ytitle='log[I!9!Dn!N!3(350!9m!3m)/I!9!Dn!N!3(500!9m!3m)]'


!p.font=-1
device,/close
set_plot,'x'
!p.charsize=0


end
```

A.18   3plot_ratHa16.pro

```
;Plot of H_alpha against 1.6 micron data for 4 galaxies.


!p.multi=0
```

```
;!p.multi=[0,2,2]
set_plot,'ps'
device,filename='3plot_ratha16.ps'
!p.font=0



restore,'ngc4254_bindata.dat'
plot, alog10(img16reb(w)),alog10(imghareb(w)), $
yrange=[-16.5,-14.5],xrange=[-6.0,-3.0], $
ystyle=1, psym=6, $
ytitle='log[I!9!Dn!N!3(1.6!9m!3m)]', $
xtitle='log[I!9!Dn!N!3(H!9a!3)]'
xyouts,-5.8,-14.8,'NGC4254',CHARSIZE = 0.8
r=linfit(alog10(img16reb(w)),alog10(imghareb(w)), yfit=yfit)
oplot,alog10(img16reb(w)),yfit



;restore,'ngc4303_bindata.dat'
;plot, alog10(img16reb(w)),alog10(imghareb(w)), $
;yrange=[-17,-14.5],xrange=[-6.0,-3.0], $
;ystyle=1, psym=6, $
;ytitle='log[I!9!Dn!N!3(1.6!9m!3m)]', $
xtitle='log[I!9!Dn!N!3(H!9a!3)]'
;xyouts,-5.8,-14.8,'NGC4303',CHARSIZE = 0.8
;r=linfit(alog10(img16reb(w)),alog10(imghareb(w)), yfit=yfit)
;oplot,alog10(img16reb(w)),yfit


;restore,'ngc4321_bindata.dat'
;plot, alog10(img16reb(w)),alog10(imghareb(w)), $
;yrange=[-16.5,-14.5],xrange=[-6.0,-3.0], $
```

```
;ystyle=1, psym=6, $

;ytitle='log[I!9!Dn!N!3(1.6!9m!3m)]', $

xtitle='log[I!9!Dn!N!3(H!9a!3)]'

;xyouts,-5.8,-14.8,'NGC4321',CHARSIZE = 0.8

;r=linfit(alog10(img16reb(w)),alog10(imghareb(w)), yfit=yfit)

;oplot,alog10(img16reb(w)),yfit




;restore,'ngc4579_bindata.dat'

;plot, alog10(img16reb(w)),alog10(imghareb(w)), $

;yrange=[-16.5,-14.5],xrange=[-5.5,-3.0], $

;ystyle=1, psym=6, $

;ytitle='log[I!9!Dn!N!3(1.6!9m!3m)]', $

xtitle='log[I!9!Dn!N!3(H!9a!3)]'

;xyouts,-5.3,-14.8,'NGC4579',CHARSIZE = 0.8

;r=linfit(alog10(img16reb(w)),alog10(imghareb(w)), yfit=yfit)

;oplot,alog10(img16reb(w)),yfit




!p.font=-1
device,/close
set_plot,'x'


end
```

A.19   readimg_Timg.pro


```
;Colour temperature map for NGC4254
```

```
;read in convoled images of NGC4254

;no good 70 image avaliable

imgha=readfits('ngc4254_ha_preped_convplw.fits',headerha)

img16=readfits('ngc4254_1.6_starfilt_convplw.fits',header16)

img100=readfits('ngc4254_100_convplw.fits',header100)

img160=readfits('ngc4254_160_convplw.fits', header160)

img250=readfits('ngc4254_250_convplw.fits',header250)

img350=readfits('ngc4254_350_convplw.fits',header350)

img500=readfits('ngc4254_500.fits',header500,exten=1)



;Convert Ha and 1.6 micron data to Jy/arcsec^2

; Waiting for Ha image units

; 1.6 image is 1Jy/arcsec^2



;Convert 100-160 micron data to Jy/arcsec^2 from

;their header information

img100=img100/10.24

img160=img160/40.96

;(convert data from Jy/pixel to Jy/arcsec^2)



;Convert 250-500 micron data to Jy/arcsec^2.Multiply SPIRE

;images by colour corrections and divide by beam areas.

img250=img250/423*0.98279*0.994

;(423beam/arcsec^2 to convert the data from Jy/beam to Jy/arcsec^2.

; The multiply lthe data by 0.98279*0.994(color corrections).)



img350=img350/751*0.98344*0.990
```

```
;(Divide the data by 751 beam/arcsec^2 to convert the data

;from Jy/beam to Jy/arcsec^2.

;The multiply the data by 0.98344*0.990

;(color corrections).)


img500=img500/1587*0.97099*1.003

;(Divide the data by 1587 beam/arcsec^2 to convert the data

;from Jy/beam to Jy/arcsec^2.

;The multiply the data by 0.97099*1.003

;(color corrections).)




;Identify the background using mask arrays.

regmask, 'ngc4254_ha_back.reg',imgha,maskha, header=headerha

regmask, 'ngc4254_1.6back.reg',img16,mask16, header=header16

regmask, 'ngc4254_160back.reg',img100,mask100, header=header100

regmask, 'ngc4254_160back.reg',img160,mask160, header=header160

regmask, 'ngc4254_spire_back.reg',img250,mask250,header=header250

regmask, 'ngc4254_spire_back.reg',img350,mask350, header=header350

regmask, 'ngc4254_spire_back.reg',img500,mask500, header=header500




;Subtract the background.

imgha=imgha-median(imgha(where(maskha eq 1)))

img16=img16-median(img16(where(mask16 eq 1)))

img100=img100-median(img100(where(mask100 eq 1)))

img160=img160-median(img160(where(mask160 eq 1)))

img250=img250-median(img250(where(mask250 eq 1)))
```

```
img350=img350-median(img350(where(mask350 eq 1)))

img500=img500-median(img500(where(mask500 eq 1)))


;Measure the noise in background regions for creating images.

sdimgha=stddev(imgha(where(maskha eq 1)))

sdimg16=stddev(img16(where(mask16 eq 1)))

sdimg100=stddev(img100(where(mask100 eq 1)))

sdimg160=stddev(img160(where(mask160 eq 1)))

sdimg250=stddev(img250(where(mask250 eq 1)))

sdimg350=stddev(img350(where(mask350 eq 1)))

sdimg500=stddev(img500(where(mask500 eq 1)))



;Cut the 250 micron image.  (Don't do this for the other bands.)

hextract,img250,header250,1627,1716,1984,2073



;Match the coordinates of the other images to the 250 micron image.

hastrom,imgha,headerha,header250

hastrom,img16,header16,header250

hastrom,img100,header100,header250

hastrom,img160,header160,header250

hastrom,img350,header350,header250

hastrom,img500,header500,header250



tc100160=colortemp(100e-6,160e-6,img100,img160,sdimg100,sdimg160)

tc160250=colortemp(160e-6,250e-6,img160,img250,sdimg160,sdimg250)

tc250350=colortemp(250e-6,350e-6,img250,img350,sdimg250,sdimg350)

tc350500=colortemp(350e-6,500e-6,img350,img500,sdimg350,sdimg500)
```

```
writefits,'ngc4254temp_100_160.fits', tc100160, header250

writefits,'ngc4254temp_160_250.fits', tc160250, header250

writefits,'ngc4254temp_250_350.fits', tc250350, header250

writefits,'ngc4254temp_350_500.fits', tc350500, header250


end
```

Bibliography

Andrews J. E., Clayton G. C., Wesson R., et al., 2011, AJ, 142, 45

Barlow M. J., Krause O., Swinyard B. M., et al., 2010, A&A, 518, L138

Bendo G. J., Boselli A., Dariush A., et al., 2012a, MNRAS, 419, 1833

Bendo G. J., Galliano F., Madden S. C., 2012b, MNRAS, 423, 197

Bendo G. J., Joseph R. D., Wells M., et al., 2002, AJ, 123, 3067

Bendo G. J., Wilson C. D., Pohlen M., et al., 2010a, A&A, 518, L65

Bendo G. J., Wilson C. D., Warren B. E., et al., 2010b, MNRAS, 402, 1409

Boquien M., Calzetti D., Combes F., et al., 2011, AJ, 142, 111

Boquien M., Calzetti D., Kramer C., et al., 2010, A&A, 518, L70

Boselli A., Eales S., Cortese L., et al., 2010, PASP, 122, 261

Boselli A., Gavazzi G., 2002, A&A, 386, 124

Buat V., Xu C., 1996, A&A, 306, 61

Calzetti D., Kennicutt R. C., Engelbracht C. W., et al., 2007, ApJ, 666, 870

Calzetti D., Kennicutt Jr. R. C., Bianchi L., et al., 2005, ApJ, 633, 871

Calzetti D., Wu S.-Y., Hong S., et al., 2010, ApJ, 714, 1256

Chester T., 1986, in Light on Dark Matter, edited by F. P. Israel, vol. 124 of
    Astrophysics and Space Science Library, 3–22

Cox A. N., 2000, Allen's astrophysical quantities, Springer Verlag New York

Davies J. I., Bianchi S., Cortese L., et al., 2012, MNRAS, 419, 3505

de Vaucouleurs G., de Vaucouleurs A., Corwin Jr. H. G., Buta R. J., Paturel G., Fouque P., 1991, Third Reference Catalogue of Bright Galaxies, Springer-Verlag Berlin Heidelberg New York

Desert F.-X., Boulanger F., Puget J. L., 1990, A&A, 237, 215

Devereux N. A., Jacoby G., Ciardullo R., 1995, AJ, 110, 1115

Devereux N. A., Young J. S., 1990a, in The Interstellar Medium in External Galaxies, edited by D. J. Hollenbach & H. A. Thronson Jr., vol. 3084 of NASA Conference Publication, 92

Devereux N. A., Young J. S., 1990b, ApJ, 359, 42

Devereux N. A., Young J. S., 1990c, ApJ, 350, L25

Devereux N. A., Young J. S., 1992, AJ, 103, 1536

Devereux N. A., Young J. S., 1993, AJ, 106, 948

Draine B. T., 2003, ARA&A, 41, 241

Draine B. T., 2011, Physics of the Interstellar and Intergalactic Medium, Princeton University Press

Draine B. T., Dale D. A., Bendo G., et al., 2007, ApJ, 663, 866

Draine B. T., Li A., 2007, ApJ, 657, 810

Duley W. W., Williams D. A., 1986, MNRAS, 223, 177

Dunne L., Eales S., Ivison R., Morgan H., Edmunds M., 2003, Nature, 424, 285

Dwek E., 1998, ApJ, 501, 643

Engelbracht C. W., Gordon K. D., Rieke G. H., Werner M. W., Dale D. A., Latter W. B., 2005, ApJ, 628, L29

ESA, 2009, `http://herschel.esac.esa.int/`

ESA, 2011, `http://herschel.esac.esa.int/Docs/SPIRE/html/spire_om.html`

Freedman W. L., Madore B. F., Gibson B. K., et al., 2001, ApJ, 553, 47

Galametz M., Madden S. C., Galliano F., et al., 2010, A&A, 518, L55

Gordon K. D., Rieke G. H., Engelbracht C. W., et al., 2005, PASP, 117, 503

Haas M., 2000, in Proceedings 232. WE-Heraeus Seminar, edited by E. M. Berkhuijsen, R. Beck, & R. A. M. Walterbos, 69–72

Habing H. J., 1996, aapr, 7, 97

Hildebrand R. H., 1983, QJRAS, 24, 267

Hinz J. L., Rieke G. H., Gordon K. D., et al., 2004, ApJS, 154, 259

Hirashita H., Buat V., Inoue A. K., 2003, A&A, 410, 83

Hollenbach D., Salpeter E. E., 1971, ApJ, 163, 155

Hollenbach D. J., Tielens A. G. G. M., 1997, ARA&A, 35, 179

Impey C. D., Neugebauer G., 1988, AJ, 95, 307

Jarrett T. H., Chester T., Cutri R., Schneider S. E., Huchra J. P., 2003, AJ, 125, 525

Kennicutt R., 1998a, in Starbursts: Triggers, Nature, and Evolution, Les Houches School, edited by B. Guiderdoni & A. Kembhavi, 1, ESP Sciences

Kennicutt Jr. R. C., 1983, ApJ, 272, 54

Kennicutt Jr. R. C., 1992, ApJ, 388, 310

Kennicutt Jr. R. C., 1998b, ARA&A, 36, 189

Kennicutt Jr. R. C., 1998c, ApJ, 498, 541

Kennicutt Jr. R. C., Armus L., Bendo G., et al., 2003, PASP, 115, 928

Kennicutt Jr. R. C., Calzetti D., Walter F., et al., 2007, ApJ, 671, 333

Kennicutt Jr. R. C., Hao C.-N., Calzetti D., et al., 2009, ApJ, 703, 1672

Kessler M. F., 1995, Space Sci.Rev., 74, 57

Knapen J. H., Stedman S., Bramich D. M., Folkes S. L., Bradley T. R., 2004, A&A, 426, 1135

Kong X., Charlot S., Brinchmann J., Fall S. M., 2004, MNRAS, 349, 769

Krause O., Birkmann S. M., Rieke G. H., et al., 2004, Nature, 432, 596

Latter W. B., 2006, http://ssc.spitzer.caltech.edu/mips/, 1

Laureijs R. J., Klaas U., Richards P. J., Schulz B., Abraham P., 2003, The ISO Handbook, Volume IV - PHT - The Imaging Photo-Polarimeter, European Space Agency

LeBertre, 2004, `http://aramis.obspm.fr/~lebertre/LNP/agb_lnp.gif`

Li A., Draine B. T., 2001, ApJ, 554, 778

Lonsdale Persson C. J., Helou G., 1987, ApJ, 314, 513

Maraston C., 2011, in Why Galaxies Care about AGB Stars II: Shining Examples and Common Inhabitants, edited by F. Kerschbaum, T. Lebzelter, R. F. Wing, vol. 445 of Astronomical Society of the Pacific Conference Series, 391

Mentuch E., Abraham R. G., Glazebrook K., et al., 2009, ApJ, 706, 1020

Mentuch E., Abraham R. G., Zibetti S., 2010, ApJ, 725, 1971

Poelarends A. J. T., Herwig F., Langer N., Heger A., 2008, ApJ, 675, 614

Poglitsch A., Waelkens C., Geis N., et al., 2010, A&A, 518, L2

Popescu C. C., Tuffs R. J., Dopita M. A., Fischera J., Kylafis N. D., Madore B. F., 2011, A&A, 527, A109

Poznanski D., Butler N., Filippenko A. V., et al., 2009, ApJ, 694, 1067

Prescott M. K. M., Kennicutt Jr. R. C., Bendo G. J., et al., 2007, ApJ, 668, 182

Press W. H., Flannery B. P., Teukolsky S. A., 1986, Numerical recipes. The art of scientific computing, Cambridge: University Press, 1986

Romanishin W., 1990, AJ, 100, 373

Salpeter E. E., 1955, ApJ, 121, 161

Sanders D. B., Mirabel I. F., 1996, ARA&A, 34, 749

Sanders D. B., Phinney E. S., Neugebauer G., Soifer B. T., Matthews K., 1989, ApJ, 347, 29

Sauvage M., Thuan T. X., 1992, ApJ, 396, L69

Schmidt M., 1959, ApJ, 129, 243

Schoeniger F., Sofue Y., 1997, A&A, 323, 14

Sibthorpe B., Ferlet M., Bendo G., Papageorgiou A., the SPIRE ICCC., 2011, `ftp://ftp.sciops.esa.int/pub/hsc-calibration/SPIRE/PHOT/Beams/beam_release_note_v1-1.pdf`

Skrutskie M. F., Cutri R. M., Stiening R., et al., 2006, AJ, 131, 1163

Smith M. W. L., Vlahakis C., Baes M., et al., 2010, A&A, 518, L51

Soifer B. T., Neugebauer G., Houck J. R., 1987, ARA&A, 25, 187

Spitzer L., 1978, Physical processes in the interstellar medium, New York Wiley-Interscience, 1978. 333 p.

Springob C. M., Masters K. L., Haynes M. P., Giovanelli R., Marinoni C., 2009, ApJS, 182, 474

Tielens A. G. G. M., 2005, The Physics and Chemistry of the Interstellar Medium, Cambridge University Press

Tuffs R. J., Popescu C. C., Pierini D., et al., 2002, ApJS, 139, 37

Verley S., Relaño M., Kramer C., et al., 2010, A&A, 518, L68

Walterbos R. A. M., Greenawalt B., 1996, ApJ, 460, 696

Walterbos R. A. M., Schwering P. B. W., 1987, A&A, 180, 27

Werner M. W., Roellig T. L., Low F. J., et al., 2004, ApJS, 154, 1

Wilson C. D., Scoville N., Rice W., 1991, AJ, 101, 1293

Zhu Y.-N., Wu H., Cao C., Li H.-N., 2008, ApJ, 686, 155

Zinner E. K., 2003, Treatise on Geochemistry, 1, 17